Universität Hamburg

DER FORSCHUNG | DER LEHRE | DER BILDUNG

Maxwell-TDDFT Nanoplasmonics and Structured Light Shaping

Dissertation zur Erlangung des Doktorgrades an der Fakultät für Mathematik, Informatik und Naturwissenschaften Fachbereich Physik der Universität Hamburg

vorgelegt von

Esra Ilke Albar

HAMBURG

2025

Gutachter/innen der Dissertation:	Prof. Dr. Angel Rubio Dr. Heiko Appel
Zusammensetzung der Prüfungskommission:	Prof. Dr. Angel Rubio Dr. Heiko Appel Prof. Dr. Franz Xaver Kärtner Prof. Dr. Daniela Pfannkuche Prof. Dr. Michael Potthoff
Vorsitzende/r der Prüfungskommission:	Prof. Dr. Michael Potthoff
Datum der Disputation:	02.02.2026
Vorsitzender Fach-Promotionsausschusses Physik:	Prof. Johannes Haller
Leiter des Fachbereichs Physik:	Prof. Dr. Markus Drescher
Dekan der Fakultät MIN:	Prof. Dr.-Ing. Norbert Ritter

Eidesstattliche Erklärung / Declaration on oath

I hereby affirm that this dissertation is my own work. I have used no aids or sources other than those credited. All passages taken verbatim or in substance from publications are clearly identified as such.

If resources based on generative artificial intelligence (gAI) were used, I affirm that the central contribution and substance of this work is my own independent effort. The complete documentation of all resources used is available in accordance with good scientific practice. I assume full responsibility for any errors or breaches of data protection that may have been generated by gAI.

Esra Ilke Albar

15.12.2025
Date

Signature

Contents

List of Figures

List of Tables

Acronyms

AETRS approximate enforced time-reversal symmetry. 21

BLYP Becke–Lee–Yang–Parr. 18

CFL Courant-Friedrichs–Lewy. 96

DFT density functional theory. 11, 15, 16, 19, 24

EDA electric dipole approximation. 10–16, 29–32, 41, 42, 44, 65, 67, 68, 70, 75, 78–83, 88–91, 94, 96–98, 100, 102, 103, I, IX, X, XII

FMC full minimal coupling. 11, 13, 31–33, 67, 68, 70, 74–76, 78–83, 88, 90–92, 94, 96–98, 100, 103, II, VIII–X, XII

GGA generalized gradient approximation. 18

HHG high harmonic generation. 12, 13, 67–69, 73, 74, 76, 81, 82, 84, 85, 88–90, 103–105, VIII

LDA local density approximation. 18

NAO numeric atomic orbitals. 20, 21

OAM orbital angular momentum. 9, 10, 12–14, 35, 39, 46–49, 51–55, 57, 59–69, 72–76, 79–85, 88–90, 102–105, II, V–IX, XI, XII

PBE Perdew–Burke–Ernzerhof. 18

PML Perfectly matched layer. 96

PWB plane-wave basis. 20

QED quantum electrodynamics. 10, 29

QEDFT quantum-electrodynamical density-functional theory. 10

RWA rotating wave approximation. 28

SE Schrödinger equation. 16

SPP surface plasmon polariton. 12

STOV spatiotemporal optical vortices. 102, 104

TDCDFT time dependent current density functional theory. 18, 19, 22

TDDFT time-dependent density functional theory. 9–11, 14–16, 19–22, 24, 29, 33, 34, 41, 89, IV

TDKS time-dependent Kohn Sham equations. 9, 33

TDSE time-dependent Schrödinger equation. 9, 13, 14, 19, 29, 34, IV

TERS tip-enhanced Raman Spectroscopy. 104

List of Symbols

$\vec{A}_{xc}$ exchange vector potential. 18, 33

$\vec{A}(\vec{r},t)$ vector potential. 30

$\vec{B}(\vec{r},t)$ magnetic field. 23, 30

$\mathcal{E}_H$ Hartree energy. 17

$\mathcal{E}_{xc}$ exchange correlation energy. 17, 18

$\mathcal{E}$ energy. 17

$\vec{E}(\vec{r},t)$ electric field. 23, 28, 30

$\vec{M}(\vec{r})$ magnetization density. 30

$\vec{P}(\vec{r})$ polarization density. 30

T kinetic energy of non-interacting electrons. 17

$\hat{a}^\dagger$ photon creation operator. 28

$\hat{a}$ photon annihilation operator. 28

$\chi_\mu(\vec{r},\vec{r'};\omega)$ microscopic susceptibility within linear response TDDFT. 24

ϵ_0 vacuum permittivity. 22

e electron charge. 32

$\vec{j}(\vec{r},t)$ probability current density. 24, 33

$\vec{J}(\vec{r},t)$ total electric current density. 32, 33

λ wavelength. 29

μ_0 vacuum permeability. 23

$n_0(\vec{r})$ space dependent electronic density. 16, 17

$n(\vec{r},t)$ space and time dependent electronic density. 18–20, 22, 24

ω frequency. 29

ϕ Kohn-Sham states. 20

ψ many body wave function. 16

$\rho(\vec{r},t)$ electronic density. 22

$\vec{r}$ position. 35

$\hat{\sigma}_{\pm}$ raising and lowering operators. 28

v_{eff} effective potential. 16

Babama

To my father

Acknowledgments

I would like to express my gratitude to my supervisor, Prof. Angel Rubio, for his guidance and support. I am equally thankful to Dr. Heiko Appel, who has taught me physics with patience and kindness and shaped my scientific thinking. I would like to thank my supervisor, Dr. Franco Bonafé, wholeheartedly; his insights and his persistence inspired me over these years. I hope to grow into the kind of scientist he exemplifies. I am grateful to Dr. Valeriia Kosheleva; her rigor and knowledge, as well as her friendship, are irreplaceable. I would also like to express my gratitude to Dr. Michael Ruggenthaler for stimulating discussions.

I am very grateful to Lena, Shahram, Charly, Blu, Mona, Kevin, Alba, Sebas, Benoit, Chris, Jacob, Jonas, Lukas Konecny, Simon, Wenwen, George, Elia, Paolo, and Francesco for their camaraderie that made MPSD feel like home.

I am grateful to Duru, Erman, Irmak, Yagmur, Talitha, Burcu, Seref, and Esin for their friendship and unwavering support.

I would like to thank Dr. Fabio Pablo Miguel Mendez-Cordoba for his contagious passion for physics and his contribution of joy.

I am grateful to my aunt Pervin Altuner for her immense support.

Most of all, I would like to thank my sister Serra Ozge Albar. She is the greatest gift I have ever received.

List of Publications

The following publications are part of this thesis:

1. **Esra Ilke Albar**, Valeriia P. Kosheleva, Heiko Appel, Angel Rubio, and Franco P. Bonafé
   "High-order harmonic generation with orbital angular momentum beams: Beyond-dipole corrections"
   Phys. Rev. A 112, 063109 – Published 10 December 2025.
   arXiv:2503.14982

2. Franco P. Bonafé, **Esra Ilke Albar**, Sebastian T. Ohlmann, Valeriia P. Kosheleva, Carlos M. Bustamante, Francesco Troisi, Angel Rubio, and Heiko Appel.
   "Full minimal coupling Maxwell-TDDFT: An ab initio framework for light-matter interaction beyond the dipole approximation"
   Phys. Rev. B 111, 085114 – Published 5 February 2025.
   arXiv:2409.08959

3. **Esra Ilke Albar**, Franco P. Bonafé, Valeriia P. Kosheleva, Sebastian T. Ohlmann, Heiko Appel, and Angel Rubio.
   "Time-resolved plasmon-assisted generation of optical-vortex pulses"
   Scientific Reports volume 13, 14748 – Published 07 September 2023.

1 Zusammenfassung

Moderne Pump-Probe-Spektroskopie nutzt zunehmend elektromagnetische Felder mit maßgeschneiderter räumlicher und zeitlicher Struktur. Attosekunden-Methoden senken die Pulsdauer in den Sub-Femtosekundenbereich und ermöglichen so die Echtzeitverfolgung elektronischer Bewegungen, während Röntgenspektroskopie Materie im Angström-Wellenlängenbereich untersucht und mit atomarer räumlicher Auflösung die Dynamik auf Kernniveau zugänglich macht. Gleichzeitig entwickelt sich räumlich strukturiertes Licht, wie verdrehte Strahlen mit Orbitaldrehimpuls (OAM), Vektorstrahlen und andere künstlich erzeugte Wellenfronten, zu einem leistungsstarken Werkzeug zur Steuerung und Untersuchung von Materie, mit Anwendungen, die von ultraschneller Bildgebung über chirale Diskriminierung bis hin zur Quanteninformationsverarbeitung reichen. Diese Fortschritte zeigen die Grenzen gängiger theoretischer Näherungen auf, insbesondere der elektrischen Dipolnäherung, die Feldgradienten, räumliche Texturen oder den intrinsischen Drehimpuls von strukturiertem Licht nicht erfassen kann. In dieser Arbeit gehen wir über die Dipolnäherung hinaus und verwenden einen vollständigen Minimal-Kopplungs-Rahmen , der die gesamte räumliche Struktur, die Gradienten und den OAM-Gehalt des elektromagnetischen Feldes beibehält. Dieser Ansatz ermöglicht es uns, die multiskalige Wechselwirkung von strukturiertem Licht mit Materie durch eine Kombination aus klassischer Elektrodynamik und quantenmechanischen Simulationen zu untersuchen und legt dabei Bereiche der Kontrolle und der Spektroskopie, die mit herkömmlichen Methoden nicht zugänglich sind.

Zunächst demonstrieren wir die Erzeugung optischer Wirbel aus nanoplasmonischen archimedischen Spiralen mithilfe von Echtzeit-Elektrodynamiksimulationen im Realraum, bei denen wir die Entstehung und zeitliche Entwicklung der lokalen Bahndrehimpulsdichte auflösen. Die resultierenden Wirbel weisen aufgrund der Drehimpulsübertragung eine ausgeprägte räumliche Struktur auf. Wir validieren

die Phasenstrukturierung des Strahls, indem wir klassisch beschriebene Punktladungen als Sonden verwenden. Die Positionsabhängigkeit der Testladungsbahnen über den Strahl hinweg unterstreicht die Notwendigkeit, die räumliche Abhängigkeit von OAM- Strahlen zu berücksichtigen.

Wir untersuchen die Erzeugung hoher Harmonischer in atomarem Wasserstoff jenseits der Dipolnäherung und verwenden dabei den Hamiltonian-Operator für vollständige minimale Kopplung, um magnetische, quadrupolare und räumliche Gradienteneffekte ohne Trunkierung einzubeziehen. Wir bestätigen die Existenz solcher Effekte mit Lasern mit ebenen Wellen. Darüber hinaus beobachten wir, dass strukturierte Felder wie Besselstrahlen charakteristische Formen nichtlinearer Dipolbewegungen und Symmetriebrüche induzieren, die besonders bei geraden Harmonischen sichtbar sind. Wir scannen die einfallende OAM-Zahl, um zu zeigen, dass Korrekturen jenseits der Dipolnäherung in der Elektronenbahn für diesen Parameter empfindlich sind. Wir erweitern diese Analyse auf den molekularen Fall. Wir untersuchen ein Benzolmolekül, das einem zirkular polarisierten Strahl aus ebenen Wellen ausgesetzt ist, und identifizieren die modifizierten Auswahlregeln jenseits des Dipols im harmonischen Spektrum.

Wir richten unseren Fokus auf die Vorwärts-Rückwärts-Kopplung von Licht und Materie. Wir verwenden in unserem numerischen Aufbau ein Cherenkov-Wellenpaket, das sich schneller als die Phasengeschwindigkeit des Lichts bewegt, um zu zeigen, dass nicht nur der Grad der Kopplung, sondern auch die Berücksichtigung der Rückwirkung der Materie auf das elektromagnetische Feld erhebliche Auswirkungen haben kann: Wir identifizieren eine Symmetriebrechung im elektronischen Wellenpaket, die nur sichtbar wird, wenn über den Dipol hinausgehende Ansätze mit der Vorwärts- Rückwärts-Kopplung kombiniert werden.

Zusammenfassend zeigen die Ergebnisse dieser Arbeit, dass die räumliche Struktur des Lichts, sein Drehimpuls und die daraus resultierende Symmetriebrechung nicht erfasst werden, wenn nur die zeitlichen Eigenschaften des elektromagnetischen Feldes berücksichtigt werden. Durch die Kombination klassischer und quantenmechanischer Beschreibungen und durch die vollständige Beschreibung des elektromagnetischen Feldes, die über die elektrische Dipolnäherung hinausgeht, untersuchen wir strukturierte elektromagnetische Felder, beginnend mit der Erzeugung plasmonischer Wirbel, bis hin zur Emission hoher Harmonischer und Cherenkov-Strahlung. Wir liefern eine Reihe von vorhersagekräftigen Simulationen, in denen die Wechselwirkung von Licht und Materie empfindlich auf räumliche Struktur und Symmetrie reagiert. Unsere Ergebnisse bieten eine Grundlage für zukünftige Studien zu strukturierten elektromagnetischen Feldern und deren Auswirkungen auf Quantensysteme.

2 Abstract

Modern pump–probe spectroscopies increasingly exploit electromagnetic fields with tailored spatial and temporal structure. Attosecond techniques push pulse durations to the sub-femtosecond regime, enabling real-time tracking of electronic motion, while X-ray spectroscopies probe matter at angstrom-scale wavelengths, accessing core-level dynamics with atomic spatial resolution. At the same time, spatially structured light, such as twisted beams carrying orbital angular momentum (OAM), vector beams, and other engineered wavefronts, is emerging as a powerful tool for controlling and interrogating matter, with applications ranging from ultrafast imaging to chiral discrimination and quantum information processing. These advances expose the limitations of common theoretical approximations, particularly the electric-dipole approximation, which cannot capture field gradients, spatial textures, or the intrinsic angular momentum of structured light. In this thesis, we go beyond the dipole approximation and employ a full minimal-coupling framework that retains the complete spatial structure, gradients, and OAM content of the electromagnetic field. This approach allows us to explore the multiscale interaction of structured light with matter through a combination of classical electrodynamics and quantum-mechanical simulations, revealing regimes of control and spectroscopy that are inaccessible to conventional treatments.

First, we demonstrate the generation of optical vortices from nanoplasmonic Archimedean spirals using real-time real-space electrodynamics simulations, where we resolve the emergence and temporal evolution of the local orbital angular momentum density. The resulting vortices manifest pronounced spatial structure owing to the angular momentum transfer. We validate the phase structuring of the beam by using classically described point charges as probes. The position dependence of the test charge trajectories across the beam highlights the necessity of accounting for the spatial dependence of OAM beams.

We proceed to investigate high-harmonic generation in atomic hydrogen beyond the dipole approximation, employing the full minimal-coupling Hamiltonian to include magnetic, quadrupolar, and spatial-gradient effects without truncation. We confirm the existence of such effects with plane-wave lasers. Moreover, we observe that structured fields such as Bessel beams induce characteristic forms of nonlinear dipole motion and symmetry breaking, which are particularly visible in even harmonics. We tune the incident OAM number to show that beyond-dipole corrections in the electron trajectory are susceptible to this parameter. We expand this analysis to the molecular case. We investigate a benzene molecule subjected to a circularly polarized plane wave beam, and identify the modified, beyond dipole selection rules in the harmonic spectrum.

We turn our focus to the forward-backward coupling of light-matter. We employ a Cherenkov wave packet traveling faster than the phase velocity of light in our numerical setup to demonstrate that not only the level of coupling, but also accounting for the back reaction of the matter to the electromagnetic field can have significant implications: We identify symmetry breaking in the electronic wave packet that is only visible when beyond dipole approaches are combined with the forward-backward coupling.

To summarize, the results of this thesis highlight that the spatial structure of light, its angular momentum, and resulting symmetry breaking are not captured when accounting only for the temporal properties of the electromagnetic field. By combining classical and quantum descriptions, and by embracing the full description of the electromagnetic field by going beyond the electric dipole approximation, we study structured electromagnetic fields starting from plasmonic vortex generation, then move to high-harmonic emission and Cherenkov radiation. We provide a set of predictive simulations where the interaction of light and matter is sensitive to spatial structure and symmetry. Our results offer a basis for future studies involving structured electromagnetic fields and their effects on quantum systems.

“ Into the space ship, Granny."
-Ursula K. Leguin, The Space Crone (1976)

3 Introduction

The interaction between light and matter is one of our main sources of information about the world. Whether through our eyes or through spectroscopy, we living beings constantly extract knowledge from this interplay: A bird knows where to perch because she sees the tree as light fires the optical nerve, and we know where a bone is broken as we map the X-ray radiation passing through the matter: our body. Hence, it is not surprising that yet another thesis focuses on light–matter interaction, describing both sides at different scales and theoretical levels. This particular thesis presents our successful efforts to couple time-dependent density functional theory (TDDFT) with Maxwell's equations, highlighting why an effort to go beyond the known approximations is necessary.

On the matter side, we work in a variety of scales: we start from the classical Drude description of the nanoplasmonic medium, where we model the medium with its pole frequency and the Drude relaxation parameters. We then expand our findings to ab initio calculations. When tackling ab initio descriptions, we operate with the time-dependent Schrödinger equation (TDSE), and then time-dependent Kohn Sham equations (TDKS) within the TDDFT formalism. TDDFT remains one of the most versatile and widely used methods for studying ultrafast and light-driven phenomena in atoms, molecules, and solids [1].

On the electromagnetic field side, structured light will have a special emphasis throughout the thesis. A particular focus is on the twisted light, also referred to as the optical vortex, namely the electromagnetic field with orbital angular momentum (OAM) along its direction of propagation. Since its first theoretical prediction by Ref. [2], and following experimental confirmation by Ref. [3], the twist of light has represented a new degree of freedom that enables new knobs to tune the light–matter interaction and devise new optical spectroscopic tools to study matter. As the name 'twisted light' implies, the wavefront twists around the propagation direction, resembling a corkscrew. Unlike the plane waves, whose

phase fronts are generally flat, twisted light has a phase dependence of the form $e^{im\phi}$. The variable m is named the topological charge, or the OAM number, since it dictates the content of OAM of the field. The twist around the beam axis superposes the field components in the middle, leading to their cancellation. This creates a dark spot at the center of OAM beams, which is also referred to as the singularity.

The applications of the OAM of light have been numerous: The helical swirl of the beam can trap small objects and optically manipulate them [4, 5]. The swirl also creates intensity rings around the propagation axis, which creates a nonhomogeneous transversal plane. The asymmetric intensity distribution of the superposed OAM beams can be used to overcome the Rayleigh limit for imaging [6], and the rich phase structuring finds application in microscopy [7]. The ground-state depletion can be modified with twisted light to sense even the wave packet of a single trapped ion [8]. The high-dimensional OAM states can be employed in quantum information protocols [9, 10]. The wide-ranging potential applications go hand in hand with an abundance of theoretical and experimental studies. Researchers have so far investigated the excitation with OAM beams [11–20] as well as scattering processes [21–24] and finally, ionization [25–32].

When it comes to the coupling, even though the extensive quantum electrodynamics (QED) formalism successfully treats both the charged particles and photons, and explains fundamental phenomena [33], its application is computationally costly and therefore limited to small systems [34–37]. The development of alternative ab initio approaches capable of treating electronic structure and light–matter coupling in more complex settings flourished as a response to those limitations of QED. Particularly, TDDFT has emerged as a powerful and computationally feasible tool for modeling electronic dynamics driven by external electromagnetic fields. Several semiclassical strategies have been proposed to account for coupling to the radiation including the Maxwell–Ehrenfest dynamics [38], multi-trajectory Ehrenfest schemes [39, 40], coherent electron–field dynamics [41], models combining Maxwell's equations with Schrödinger's [42], and finally the combination of Maxwell–TDDFT[43, 44]. However, in most applications, the light field is introduced semiclassically as a practical step towards the full quantum-electrodynamical density-functional theory (QEDFT) first-principles framework. It is typically treated within the electric dipole approximation (EDA), so that only the temporal dependence of the electromagnetic field couples to the electrons.

Yet with the growing sophistication of modern pump-probe spectroscopies, the shortcomings of the EDA are becoming more apparent. When the wavelength is comparable to the system size, or when the field exhibits spatial inhomogeneity or magnetic effects, the EDA picture breaks down. This leads to new physical effects,

modified selection rules, and novel opportunities for controlling matter with light and improving the performance of optical spectroscopies[12, 45]. Beyond-dipole behavior has been observed in X-ray and XUV spectroscopy [46–51], strong-field and attosecond physics [52–59], magneto-optical processes [48, 60], chiral cavity QED [61–63], nanoplasmonic spectroscopy [64–66], and interactions with structured light among many other studies [16, 25, 26, 61, 67]. Most existing treatments of such beyond dipole fingerprints rely on perturbative approaches or multipolar expansions. However, such truncated expansions are origin-dependent [47] and costly [45]. Although computationally feasible non-dipole strong-field Hamiltonians [57] have provided valuable insights for specific applications, a unified framework that treats arbitrary spatial field distributions and their associated radiation reaction in real time is yet to be achieved.

In this work, we employ the exact full minimal coupling (FMC) methodology as a remedy to these limitations. By retaining the complete spatial form of the electromagnetic vector potential, the FMC approach avoids the multipole truncation and naturally incorporates magnetic-field effects, field gradients, and non-dipole interactions. Within this formalism, we employ a parallel, open-source Maxwell–TDDFT scheme computed in real space and real time. This combined framework treats electrons and electromagnetic fields on equal footing, and enables an ab initio exploration of light–matter interaction, which captures the beyond-dipole phenomena and radiation back reaction.

The thesis is organized as follows: The initial section 4 comprises the theoretical methodology of the thesis. We detail the formulations we employ as well as numerical implementations. we start with providing an overview of density functional theory (DFT) and TDDFT. An explanation of EDA and our beyond dipole approach FMC details follow. We introduce our beyond dipole FMC methodology. Then, we detail the forward-backward coupling, which enables us to discern not only the effect of light on the matter, but the complete cross-talk of light and matter. Maxwell's equations, as well as the Riemann-Silberstein formalism, are found next. Linear, non-magnetic medium, as the Drude model of the nanoplasmonic medium, is also explained in this section. Then we move on to elaborate on the electromagnetic field we employ: we expand on our formalism of twisted light in the form of Bessel beams. In the final subsections, an account of the code infrastructure is found. We explain the multisystem framework and the spatial laser implementation of the Octopus-code, which is the code base where most of the calculations of this work are performed.

Twisted-light beams are routinely produced using spiral phase plates [68], forked holograms [69], q-plates [70], metallic nanostructures [71–75]). To develop compact and reliable techniques to generate twisted beams that can fulfill the

requirements of the emerging photonic technologies is crucial. Therefore, the interplay of the nanolasmonics and the twisted light is worthy of attention. In the following chapter 5, we investigate the generation and transfer of orbital angular momentum (OAM) via nanoplasmonic spiral vortex generators. We describe a golden Archimedean spiral to investigate time-resolved twisted light generation from a circularly polarized plane wave pulse. We probe the passage of the incident pulse through the Archimedean spiral and resolve the generated OAM in space and time.

In the generation of OAM with the nanoplasmonic structures, surface plasmon polariton (SPP)s play a crucial role. Previous studies have addressed the emergence of these hybrid light matter surface states employing plasmonic Archimedean spirals [76]. There have been numerical studies studying the mechanism for such polaritonic modes with OAM content [77–79]. We build on this understanding by examining the scattered radiation from the spiral and evaluating its OAM evolution in time. Since we use an incident ultrashort pulse, we are also able to comment on the spatiotemporal shaping of the resulting twisted beam.

We do not confine ourselves to examining the vacuum component of the scattered pulse: we model a diatomic target molecule that consists of classically described point-like particles and subject it to the radiation generated by the plasmonic spiral. We capture the complete process from the very emergence of the twisted beam up until the angular momentum transfer to the target particles. By displacing the target system across the cross section of the generated radiation, we confirm the spatial structuring of the OAM beam, which verifies the need for beyond dipole approaches.

In the following chapter 6, we adopt a more accurate, ab initio description of the matter. We investigate high harmonic generation (HHG), a widely used non-linear mechanism for generating ultrashort, high-frequency pulses. In this process, an intense laser interacts with the target system and induces emission at integer multiples of its driving frequency [80]. HHG has transformed time-resolved spectroscopy by enabling the observation of ultrafast electron dynamics, and has been applied extensively to both gaseous and solid-state targets [81, 82]. Here, we focus on HHG from atomic hydrogen driven by beams carrying orbital angular momentum (OAM).

The inherent spatial variance of said beams is incompatible with the EDA, where electromagnetic fields are solely represented with their time dependence. Hence, the HHG with OAM beams case resides outside of the boundaries of the ‘Dipole Oasis’, which mainly is investigated in terms of intensity and wavelength limits [83]. Up until now, HHG with OAM beams has been studied in the light of the local dipole approximation [84–88], which merely accounts for the local

amplitude of the field. However, we report that this approach has its shortcomings as it overlooks the effects caused by the magnetic field or electric quadrupoles stemming from the gradients of the field.

HHG beyond the EDA has been addressed by numerous works, be it relativistic [89, 90] or non-relativistic and rather wavelength and intensity related [83]. These works have identified magnetic field caused deviations in the electron trajectory referred to as figure-of-eight motion [55, 91–96]. Their findings showed that when the spatial distribution of the vector potential is retained, one can calculate the resulting magnetic field; therefore, radiation pressure effects and breaking of forward-backward symmetry along the laser propagation axis can be addressed. The effect of this symmetry breaking on the resulting momentum distribution of electrons has been confirmed by experiments [97].

However, while succeeding at identifying the magnetic field effects, the previous non-dipole approaches have employed either the strong field approximation (SFA) [98] or the multipolar expansion[92], which necessarily involve spatial truncations or approximations. This motivates the need for a fully spatially resolved treatment of the light field, especially in the case of structured beams. In this work, we explore the intrinsic properties of OAM beams, which include the spatial gradients as well as magnetic field effects. We work with FMC in the non-relativistic regime, which accounts for the full spatial characteristics of the beam without resorting to truncations.

To investigate the beyond dipole effects in HHG, we solve the TDSE for the electron of a hydrogen atom in real space and real time. We compute the HHG spectrum from positions at different transverse locations relative to the beam axis. Our results reveal symmetry breaking owing to the magnetic and gradient-induced forces that manifest in the appearance of even harmonics. Resolving the electron trajectories allows us to identify clear fingerprints of the OAM: The OAM driven electron has trajectory components besides the polarization or propagation axes. The angular dependence of emitted harmonics in the transversal plane reveals that the off-axis (polarization-orthogonal) component shows substantial non-dipole corrections. Learning from this, we compute the off-axis harmonics response as a function of the OAM number of the incident beam. We observe that particularly even harmonics respond well to OAM adjustment. The final subsection of this chapter includes the HHG calculations of the benzene molecule, where we employ a circularly polarized pulse and unravel beyond-dipole effects of symmetry in spectra.

The following chapter is reserved for the Cherenkov emission from an electronic wavepacket with the FMC tool. The wavepacket is a fitting playground to demonstrate the effect of both spatial dependence and backward reaction. We

first detail the efforts to optimize the numerical parameters to overcome the challenges imposed by the uncertainty principle. With the optimized simulations, we can test the effects of two parameters: The level of coupling and the effect of back reaction of the emission. We provide the corresponding results with an emphasis on the forward-backward coupling scheme, which enables us to couple its emitted radiation back into the quantum dynamics of the wavepacket.

This thesis aims to demonstrate the beyond-dipole phenomena that emerge from the interaction of matter with the spatial structuring of light. We combine solutions of Maxwell's equations with nanoplasmonics, TDSE and TDDFT calculations on the matter side. We explore how spatial gradients and magnetic components of spatiotemporally structured beams show beyond dipole fingerprints. We start from the generation of OAM beams, and expand the understanding of OAM transfer across multiple regimes. We cover short OAM pulses generated from a plane-wave through spiral-shaped structures, as well as analytically derived exact twisted modes of Maxwell's solutions. The target systems span from classically described particles to fully ab initio descriptions of electronic matter.

Through this multiscale and multiphysics framework, we capture accurately the relevant symmetry-breaking mechanisms enabled by spatial gradients, magnetic field effects, and the bidirectional nature of forward-backward coupling of light and matter. We emphasize that these mechanisms are invisible within the EDA.

4 Theory & Implementation

The investigation of light–matter interactions under structured electromagnetic fields requires the development of both analytical and numerical frameworks. In this chapter, we present the theoretical constructs and numerical implementations employed throughout the thesis. These efforts paved the way for simulations spanning multiple scales of time and space that also go beyond conventional approximations, such as the EDA.

We begin by outlining the core theoretical formalism of DFT and TDDFT, which forms the quantum mechanical background for describing the electronic dynamics of matter. To account for the electromagnetic field dynamics and its coupling with matter, we introduce Maxwell's equations in the Riemann–Silberstein formalism. We also tackle the generation of orbital angular momentum with nanoplasmonic structures: For the modeling of this process, we choose a linear, non-magnetic medium captured via the Drude model, the theory of which we provide in this section.

We continue with a primer about light matter interaction. We present the novel full minimal coupling implementation [99], which allows a complete coupling between the electromagnetic field and the electronic system, capturing both spatial and temporal characteristics of the field and the corresponding response of the material. Our novel approach enables a new class of simulations that reach beyond the traditional electric dipole approximation, offering insights into the symmetry breaking in Cherenkov radiation, orbital angular momentum transfer, and structured field-driven nonlinearities. We continue with the introduction of a full ab initio *forward-backward coupling* scheme, which allows not only to treat the action of the electromagnetic field on the matter system, but also includes the back reaction from the matter in the form of radiation.

We then elaborate on the details of the structured light sources used in this work. Bessel beams, which carry orbital angular momentum, are introduced as

a class of twisted light. We provide a vector potential formulation that retains full spatial dependence and allows for flexible construction in Cartesian coordinates, which is crucial for our implementation in the Octopus code [99, 100]. These beams serve as probes to investigate light–matter coupling effects that are inaccessible when using plane-waves or under the EDA.

We introduce the *Multisystem* framework of the Octopus code, which enabled us to perform calculations across a vast variety of systems and scales. To simulate such spatially structured laser fields within our TDDFT framework, we also detail the implementation of position-dependent laser sources ('External Source') in the Octopus code. This includes a computationally efficient approach that avoids a full propagation of Maxwell's equations while retaining spatial dependence, which is crucial for beyond-dipole studies.

4.1 Density Functional Theory

The way to describe the electronic structure of the matter system is through the solution of the many-body Schrödinger equation

$$\hat{H}\psi_j(r_1, ..., r_N) = \mathcal{E}_n\psi(_1, ..., r_N), \tag{1}$$

where the Hamiltonian for Schrödinger equation (SE) reads:

$$\hat{H} = -\sum_{i=1}^{N} \frac{\hbar^2}{2m_e}\nabla_i^2 - \sum_{i=1}^{N}\sum_{a} \frac{Z_a e^2}{|\vec{r_i} - \vec{R_a}|} + \sum_{i\neq j} \frac{e^2}{|\vec{r_i} - \vec{r_j}|} \tag{2}$$

Here, the first term describes the kinetic energy of electrons, while the second term represents Coulomb interactions of electrons with nuclei with charge Z_a, and the last term denotes the electron-electron repulsion. Tackling this problem implies solving for a system that requires dependence on $3N$ spatial coordinates.

The many-body wavefunction ψ depends on the behavior of N particles. However, such a solution beyond a small number of interacting particles is rather costly, if feasible. In this sense, DFT provides a remedy to the computational cost as it allows the many-body problem to be expressed solely as a function of 3 spatial coordinates. This ground-breaking idea was founded on two foundational theorems proposed by Hohenberg and Kohn in 1964 [101].

Their first theorem provides a bijection between the external potential and the density of the system. This is deduced from the connection that the external potential $v_{eff}(\vec{r})$, as well as the ground state wave function, are unique functionals of the ground state electronic density $n_0(\vec{r})$. This implies that all properties of the system, such as the ground-state energy and excitation energies, are also

determined by $n_0(\vec{r})$.

The second theorem proposed in the same paper demonstrates that the exact ground state density $n_0(\vec{r})$ should minimize the total energy functional $\mathcal{E}[n_0]$. This reduces the many-body problem to a minimization problem over densities.

However, an exact functional $F[n_0]$ that will connect the energy $\mathcal{E}[n_0]$

$$\mathcal{E}[n_0] = F[n_0] + \int v_{eff}(\vec{r}) n_0(\vec{r}) d^3r \tag{3}$$

and the external potential as in Eq. (3) is not known.

In 1965, Kohn and Sham tackled this unknown functional, [102], and expressed it in parts as

$$F[n_0] = T[n_0] + \mathcal{E}_H[n_0] + \mathcal{E}_{xc}[n_0]. \tag{4}$$

Here, the term $T[n_0]$ denotes the kinetic energy of non-interacting electrons, while $\mathcal{E}_H[n_0]$ is the Hartree energy and $\mathcal{E}_{xc}[n_0]$ is the exchange-correlation functional, which stores all of the many-body effects extending beyond Hartree.

The effective potential acting on the system can be expressed as

$$v_{eff}(\vec{r}) = v_{ext}(\vec{r}) + \int \frac{n_0(\vec{r'})}{|\vec{r} - \vec{r'}|} d^3r' + v_{xc}(\vec{r}). \tag{5}$$

The exchange-correlation potential is related to the exchange correlation energy as $v_{xc}(\vec{r}) = \frac{\delta \mathcal{E}_{xc}}{\delta n_0(\vec{r})}$.

These steps of the Kohn-Sham construction allow us to solve the problem through a fictitious non-interacting electronic system with auxiliary orbitals. These orbitals are obtained from

$$\left[-\frac{\hbar^2 \nabla^2}{2m_e} + v_{eff}[n_0](\vec{r}) \right] \phi_j(\vec{r}) = \epsilon_j \phi_j(\vec{r}), \tag{6}$$

where the Kohn-Sham states $\phi_j(\vec{r})$ are functionals of the space-dependent electron density $n_0(\vec{r})$. This formalism is built upon the unique mapping of the external potential v_{eff}; consequently, all observables are functionals of the ground-state density $n_0(r)$ as explained above, and the exact ground-state density is the solution that minimizes the total-energy functional as a function of electronic density, [101, 102]. The density is reached by summing over occupied orbitals

$$\sum_{j=1}^{N_{\text{occ}}} |\phi_j(\vec{r})|^2 = n_0(\vec{r}). \tag{7}$$

Static DFT relies on the solution of the self-consistent eigenvalue problem in

(6). Here, an initial guess for the ground state electron density n_0 is produced, a corresponding Kohn-Sham potential is built, which in turn yields via Eq. (6) new orbitals $\phi_j(\vec{r})$ and density n_0. Iteration is continued until a certain threshold for the difference of density or energy is reached. However, this does not conclude the story: The exact form of the exchange-correlation potential is not known, which is approached by different levels of approximations.

The very first approach to approximate $\mathcal{E}_{xc}$ was introduced already by Kohn and Sham and is called local density approximation (LDA). This approximation assumes that $\mathcal{E}_{xc}$ depends only on the local value of the density at a given point and relates the exchange correlation energy to the corresponding energy of a homogeneous electron gas with this value of the density

$$\mathcal{E}_{xc}^{\mathrm{LDA}}[n_0] = \int n_0(\vec{r})\, \varepsilon_{xc}^{\mathrm{unif}}(n_0(\vec{r}))\; d^3r. \tag{8}$$

Another approach is to consider the gradients of the density to increase accuracy. The generalized gradient approximation (GGA) follows this formalism:

$$\mathcal{E}_{xc}^{\mathrm{GGA}}[n_0] = \int f(n_0(\vec{r}), \nabla n_0(\vec{r}))\; d^3r. \tag{9}$$

Popular versions of this approach include the Perdew–Burke–Ernzerhof (PBE) and Becke–Lee–Yang–Parr (BLYP) functionals, [103–105]. While the search for a more accurate description of the exchange-correlation functional is ongoing, and there are additional options, such as borrowing the exact Hartree-Fock exchange for correction (as in the case of hybrid functionals), the process has been linked to 'Jacob's Ladder' [106]. The LDA and GGA approaches prove useful for our study, since they provide a good balance between accuracy and computational cost. Hence, we choose our final steps early in the ladder and restrict ourselves to these two approximations of functionals.

So far, we have emphasized the one-to-one correspondence between the electron density $n(\vec{r}, t)$ and the external potential $v_{eff}(\vec{r}, t)$, which is the concept of $v-$*representability*. When the external perturbation cannot be described solely by a scalar potential, namely, a vector potential is present and magnetic effects become relevant, the electron density alone is no longer sufficient. In fact, time-dependent currents are, in general, not v-representable, as distinct vector potentials can give rise to the same density while inducing different current distributions [107]. Then the current density must be introduced as an additional basic variable[1]. time dependent current density functional theory (TDCDFT) provides such a generalization by extending density functional theory to include the paramagnetic current, thereby introducing an exchange–correlation vector potential $\vec{A}_{xc}$ that ensures gauge invariance and enables a consistent description

of magnetic and non-dipole effects.

In practice, however, the limited availability and maturity of current dependent exchange–correlation functionals restrict the widespread use of TDCDFT. For this reason, and because many time-dependent observables of interest are primarily density-driven, we employ TDDFT with full minimal coupling to vector potential to describe dynamical phenomena in this work. TDDFT extends ground-state DFT to the time domain and provides access to excited-state properties, non-equilibrium dynamics, and ultrafast responses, while remaining computationally feasible for realistic systems. In the following subsection, we introduce the TDDFT formalism and outline the specific numerical implementations and approximations adopted in this work. The SI system of units is used in the paper unless specified otherwise.

4.2 Time-Dependent Density Functional Theory

For time-dependent phenomena, the TDSE

$$\hat{H}\psi_j(r_1, ..., r_N) = i\hbar\frac{\partial}{\partial t}(\psi(r_1, ..., r_N)) \tag{10}$$

has to be solved.

Within the same spirit of DFT, TDDFT scales the problem down, using the one-to-one correspondence of the time-dependent external potential and the time-dependent electronic density $n(\vec{r}, t)$. This correspondence was proven in the Runge-Gross theorem [108], which is analogous to the Hohenberg–Kohn theorem in ground-state DFT. It states that, for a fixed initial many-body wavefunction, there exists such a correspondence between time-dependent external potentials and time-dependent densities up to an additive function of time. The implication of this is that all observables of a time-dependent interacting system can be written as unique functionals of the density. The proof assumes that the external potential is Taylor-expandable around the initial time and that the initial state is sufficiently well behaved.

As mentioned in the previous section, this concept is called the $v-representability$, which entails the requirement that a given density $n(\vec{r}, t)$ can be generated by at least one external potential $v_{eff}(\vec{r}, t)$. In their work, Runge and Gross postulated non-interacting v-representability, which states that for any interacting density, there exists a Kohn–Sham potential that reproduces it in a non-interacting system. This postulate was later proven by Van Leeuwen, who showed that under mild conditions imposed on the initial state and boundary conditions, such a potential always exists [109]. This proof legitimized the application of TDDFT.

The time-dependent Kohn-Sham equations take the form [110].

$$\left[-\frac{\nabla^2}{2} + v_{eff}[n](\vec{r},t)\right]\phi_j(\vec{r},t) = i\frac{\partial}{\partial t}\epsilon_j\phi_j(\vec{r},t). \tag{11}$$

Here, the time-dependent Kohn-Sham states ϕ, as well as $n(\vec{r},t)$, do not only depend on space, but also evolve in time. Consequently, solving the scheme presented in Eq. (11) computationally allows for the description of time-dependent phenomena [111].

The corresponding sum over occupied states for a given time t in TDDFT is used to reach the correct form of density as a function of time

$$\sum_j |\phi_j(\vec{r},t)|^2 = n(\vec{r},t). \tag{12}$$

The initial condition is set by the ground state density and orbitals provided by static DFT in this work, which is a common procedure for TDDFT. On the other hand, there have been works showing that the exact exchange–correlation potential depends on the history of the density and the initial state, a feature known as memory dependence [112]. However, while neglecting memory in adiabatic approximations leads to failures in describing charge-transfer dynamics, double excitations, and strongly correlated systems [113], this study dwells outside of these phenomena.

To tackle the problem numerically, a choice of basis or representation for the Kohn-Sham states is required. The accuracy and the efficiency of a calculation are strongly determined by this choice. Some common basis representations are the plane-wave basis (PWB), numeric atomic orbitals (NAO), and the real space grid. The first approach expands the orbitals as a Fourier series using reciprocal lattice vectors, and it is well-suited for the periodic description of solids. On the other hand, NAO expresses the orbitals as solutions of the radial Schrödinger equation centered around the atoms, which corresponds to tabulated radial functions multiplied by spherical harmonics, which represents a good candidate for all-electron calculations [114]. However, these basis sets represent challenges when describing continuum and ionization. In this work, we employ the real-space representation, which corresponds to orbitals discretized directly on a spatial grid, implemented in the Octopus code [115–117]. This representation grants the flexibility in modeling since no bias from the basis set is introduced. Moreover, real-space description is naturally fitting to real-time propagation since with this scheme, derivatives and potentials are represented as finite-difference stencils. Then an update in time to these quantities involves only neighboring grid points, which

reduces computational overhead by avoiding, for instance, dense matrix vector multiplications encountered in NAO. A final advantage of a real-space representation is the treatment of the continuum. This is of importance in the present case, since we would like to study high harmonic generation phenomena. While continuum and ionization problems can be treated via absorbing boundaries around a real space simulation box [118], the localized nature of other basis sets might represent a challenge.

Another key aspect to consider when modeling matter with the TDDFT formalism is the core electrons: Core states are inert, and they usually do not contribute much to bonding or dynamics. Nonetheless, one can choose to represent core electrons explicitly in time-dependent Kohn-Sham equations, keeping their Coulomb interaction with nuclei and their effect on valence electrons. This is referred to as *all-electron calculation*. However, this entails a computational cost: Since these states oscillate rapidly, the discretization in space has to be fine to cover their behavior. A workaround is to employ pseudopotentials, which are effective potentials that replace explicit treatment of core-level electrons with an assigned effective potential. This potential should reproduce the interaction between the core electrons and the atomic nucleus with the valence electrons.

Nonetheless, when considering electromagnetic coupling, the computational efficiency of pseudopotentials comes with a cost: The calculations with pseudopotentials suffer from a path ambiguity due to the nonlocal part [99, 119, 120]. Unlike all-electron calculations, where the potential is local and couples directly to an electromagnetic field, the nonlocal part of the pseudopotential depends on two spatial points. Since different paths connecting these points can lead to different results, there is no unique, gauge-invariant prescription. Therefore, in this work, we benchmark our TDDFT calculations with all-electron counterparts when it is feasible.

Once the basis representation and the addressing of core-level electrons are decided, the next step is to propagate the calculation in time

$$U(t, t_0) = \mathcal{T} \exp\left[-\frac{i}{\hbar}\int_{t_0}^{t} H(t')dt'\right], \tag{13}$$

where $\mathcal{T}$ is the time-ordering operator. Throughout this work, two approaches to time propagation are used: approximate enforced time-reversal symmetry (AETRS) and exponential midpoint. The first approach relies on the extrapolated Hamiltonian $\tilde{H}(t+\Delta t) \approx H(t) + \Delta t \dot{H}(t) + \frac{\Delta t^2}{2}\ddot{H}(t)$ and uses the following

propagation scheme

$$U_{AETRS}(\Delta t) = \exp\left[-\frac{i\Delta t}{2\hbar}(\tilde{H}(t+\Delta t) + H(t))\right]. \tag{14}$$

The exponential midpoint scheme predicts the state ϕ at the midpoint and estimates the Hamiltonian from the predicted density, then applies the propagator

$$U_{EM}(\Delta t) = \exp\left[-\frac{i\Delta t}{\hbar}H(t+\Delta t/2)\right]. \tag{15}$$

to arrive at the state in the following timestep.

In this subsection, we introduced our main tool for modeling matter within the formalism of TDDFT, while elaborating on the numerical aspects such as basis representation and time-propagation schemes. We note that extensions to TDDFT such as TDCDFT, which explicitly incorporate vector potentials and currents, could provide a more general framework for treating the response to magnetic or spatially structured electromagnetic fields in the future; however, the present work is confined to the standard TDDFT formalism.

Having established these foundations, the following sections will first dwell on Maxwell's equations, then turn to the description of light–matter coupling, where we outline the different levels of theory and the approaches used to incorporate the electromagnetic field.

4.3 Classical Maxwell's Equations and the Riemann-Silberstein Formalism

Maxwell's equations govern the behavior of the electromagnetic field. In this thesis, we focus on their time-dependent microscopic expressions:

$$\vec{\nabla} \cdot \vec{E}(\vec{r}, t) = \frac{1}{\epsilon_0}\rho(\vec{r}, t), \tag{16}$$

$$\vec{\nabla} \cdot \vec{B}(\vec{r}, t) = 0 \tag{17}$$

$$-\partial_t \vec{B}(\vec{r}, t) = \vec{\nabla} \times \vec{E}(\vec{r}, t), \tag{18}$$

$$\mu_0\epsilon_0\partial_t \vec{E}(\vec{r}, t) = \vec{\nabla} \times \vec{B}(\vec{r}, t) - \mu_0\vec{j}(\vec{r}, t). \tag{19}$$

They consist of Gauß's laws Eqs. (16) and (17), Faraday's law in Eq. (18), and Ampère's law Eq. (19). Gauß's law in Eq. (16) connects the electric field $\vec{E}(\vec{r}, t)$ with the electronic density $\rho(\vec{r}, t)$ (connected to electronic probability density $n(\vec{r}, t)$ with relation $\rho(\vec{r}, t) = -|e|n(\vec{r}, t)$) and states that the charges result in an electric field. Here, ϵ_0 denotes the vacuum permittivity. Gauß's law of magnetism, seen in Eq. (17), on the other hand, states that for magnetic field $\vec{B}(\vec{r}, t)$, there

are no monopoles.

These two equations are time-dependent. Faraday's law expresses that the temporal change in the magnetic field gives rise to an electric field. Symmetrically, Ampère's law states that the time-dependent changes in the electric field, along with the displacement current $\vec{j}(\vec{r},t)$, induce a magnetic field. Here, μ_0 denotes the vacuum permeability.

It is worth noting that the charge density described in Eq. (16) and the current contribution $\vec{j}(\vec{r},t)$ seen in Eq. (19) are the contributions of matter to Maxwell's equations. The key to coupling light with matter resides within these terms.

In classical electrodynamics, the electromagnetic field energy is a function of the physical, gauge-invariant electric field $\vec{E}$ and magnetic field $\vec{B}$. The corresponding electromagnetic energy density is given by

$$\vec{u}(\vec{r},t) = \frac{1}{2}\left(\epsilon_0 \vec{E}^2(\vec{r},t) + \frac{1}{\mu_0}\vec{B}^2(\vec{r},t)\right), \tag{20}$$

whose spatial integral yields the total energy of the electromagnetic field. Motivated by this physical interpretation that $\vec{E}(\vec{r},t)$ and $\vec{B}(\vec{r},t)$ are fundamental observables, the Riemann–Silberstein formalism offers the opportunity of combining electromagnetic fields into one complex vector, also referred to as the Riemann-Silberstein vector [121–123]. This vector has the electric field incorporated into its real part, while the magnetic field constitutes its imaginary part

$$\vec{F}^{\pm}(\vec{r},t) = \sqrt{\frac{\epsilon_0}{2}}\vec{E}(\vec{r},t) \pm i\sqrt{\frac{1}{2\mu_0}}\vec{B}(\vec{r},t). \tag{21}$$

In this complex electromagnetic vector, electric and magnetic fields are scaled by the prefactors $\sqrt{\epsilon_0/2}$ and $\sqrt{1/2\mu_0}$. This establishes the connection to the electromagnetic energy density

$$\vec{u}(\vec{r},t) = \vec{F}^{-}(\vec{r},t)\cdot\vec{F}^{*}(\vec{r},t) = \vec{F}^{-}(\vec{r},t)\cdot\vec{F}^{+}(\vec{r},t) = \vec{F}^{+}(\vec{r},t)\cdot(\vec{F}^{+})^{*}(\vec{r},t), \tag{22}$$

where the Riemann-Silberstein vectors of different handedness are $\vec{F}^{+}(\vec{r},t)$ and $\vec{F}^{-}(\vec{r},t)$, which are also complex conjugates[124].

The Riemann-Silberstein formalism allows one to re-express Maxwell equations in numerically convenient forms [73, 125]. Two Gauß's laws can be combined to yield the modified Gauß's law

$$\boldsymbol{\nabla}\cdot\vec{F}(\vec{r},t) = \frac{1}{\sqrt{2\epsilon_0}}\rho(\vec{r},t). \tag{23}$$

Similarly, Faraday's and Ampère's laws are combined in the Riemann-Silberstein formalism to yield a unified equation of motion for the electromagnetic field

$$i\partial_t \vec{F}(\vec{r},t) = c\boldsymbol{\nabla}\times\vec{F}(\vec{r},t) - \frac{i}{\sqrt{2\epsilon_0}}\vec{J}(\vec{r},t). \tag{24}$$

Here, c is the speed of light in vacuum with the relation $c = 1/\sqrt{\epsilon_0\mu_0}$. This form has the advantage of evaluating the electric and magnetic fields on the same grid simultaneously, instead of the evaluation of the electric and magnetic fields on separate grids located midway between the pair of other components, as is common for finite-difference time-domain (FDTD) methods in computational electromagnetism [126]. Another advantage is the description of enveloped short pulses: While one could also evaluate the fields via the Helmholtz equation, the explicit, approximation-free time evaluation of the fields in Eq. (24) provides an excellent description of the electromagnetic field even in a broad frequency range.

4.4 Linear, Non-Magnetic Medium as Drude Model

While DFT describes the electronic response at the microscopic level, classical electrodynamics often treats materials through an effective dielectric function. The Drude model is a simple and commonly used form of this response, which connects the quantum description and classical nanoplasmonic models. Although the ultimate goal is to couple microscopic Maxwell equations with the TDDFT formalism using the time-dependent electronic density $n(\vec{r},t)$ and current density $\vec{j}(\vec{r},t)$, effective medium approaches remain useful for describing the electromagnetic response at larger length scales.

The linear response of materials as given by the TDDFT formalism yields the susceptibility $\chi_\mu(\vec{r},\vec{r'};\omega)$, which is connected to the expansion of the density around the equilibrium

$$\delta n(\vec{r},\omega) = \int d^3r' \chi_{mic}(\vec{r},\vec{r'};\omega)\delta v_{ext}(\vec{r'},\omega). \tag{25}$$

For a simple metal where only the free electron response survives, this microscopic TDDFT response reproduces the Drude response. Spatial averaging of this quantity paves the way to the Drude susceptibility, which will be detailed in this chapter. Since this is valid in the linear regime, we employ a linear medium description to study macroscopic scales.

A linear medium is defined by the linear relationship the displacement vector $\vec{\mathbf{D}}(\vec{r},\omega)$ has with the exciting electric field $\vec{\mathbf{E}}(\vec{r},\omega)$; henceforth, the constitutive relation for $\vec{D}$ takes the form

$$\vec{\mathbf{D}}(\vec{r},\omega) = \epsilon(\vec{r},\omega)\vec{\mathbf{E}}(\vec{r},\omega). \tag{26}$$

Going into the time domain, Eq. (26) corresponds to a convolution of the first-order response function $\chi(\vec{r}, t-\tau)$ and time-dependent electric field $\vec{E}(\vec{r},t)$. This allows us to separate the treatment of the electric field-dependent part of the response $\epsilon_0\vec{E}(\vec{r},t)$ and the polarization vector $\vec{P}(\vec{r},t)$. Here, $\epsilon(\vec{r},\omega)$ represents the frequency-dependent permittivity of the material while ϵ_0 is the vacuum permittivity. Then the displacement vector has the form

$$\vec{D}(\vec{r},t) = \chi(\vec{r},t) * \vec{E}(\vec{r},t) = \int_0^\infty \chi(\vec{r},t-\tau)\vec{E}(\vec{r},\tau)d\tau = \epsilon_0\vec{E}(\vec{r},t) + \vec{P}(\vec{r},t). \tag{27}$$

Ampère's law connects the applied magnetic field $\vec{H}(\vec{r},t)$ with the displacement vector

$$\begin{aligned} \vec{\nabla} \times \vec{H}(\vec{r},t) &= \partial_t\vec{D}(\vec{r},t) + \vec{J}_{free}(\vec{r},t) \qquad (28)\\ &= \epsilon_0\partial_t\vec{E}(\vec{r},t) + \vec{J}_p(\vec{r},t) + \vec{J}_{free}(\vec{r},t). \end{aligned}$$

The final form of Eq. (28) is reached by using the definition of the displacement vector in Eq. (27) and the definition of polarization current $\vec{J_P}$

$$\vec{J_P} = \partial_t\vec{P}(\vec{r},t) = \epsilon_0\partial_t\int_0^t \chi_e(\vec{r},\tau)\vec{E}(t-\tau)d\tau. \tag{29}$$

On the other hand, the total magnetic field in a medium can be expressed via the combination of the applied external magnetic field $\vec{H}(\vec{r},t)$ and magnetization $\vec{M}(\vec{r},t)$ of the medium given by

$$\vec{B}(\vec{r},t) = \mu_0(\vec{H}(\vec{r},t) + \vec{M}(\vec{r},t)). \tag{30}$$

With this definition in mind, one can see that, symmetrically to Ampère's law, the electric field is now connected by Faraday's law to the magnetization.

$$\begin{aligned} \vec{\nabla} \times \vec{E}(\vec{r},t) &= -\partial_t\vec{B}(\vec{r},t) \qquad (31)\\ &= -\mu_0\partial_t\vec{H}(\vec{r},t) - \mu_0\partial_t\vec{M}(\vec{r},t)). \qquad (32) \end{aligned}$$

Keeping in mind the form of the complex bilinear vector shown in Eq. (21), one can express the time derivatives of electric and magnetic fields in terms of such a representation.

$$i\partial_t \vec{F}^{\pm} = i\left(\sqrt{\frac{\epsilon_0}{2}}\partial_t \vec{E} \pm i\sqrt{\frac{1}{2\mu_0}}\partial_t \vec{B}\right) \tag{33}$$

Using the connection given by Ampère's law in Eq. (28) and Faraday's law in Eq. (32) in Riemann-Silberstein formalism:

$$i\partial_t \vec{F}^{\pm} = i\left(\sqrt{\frac{\epsilon_0}{2}}(\frac{1}{\epsilon_0}(\vec{\nabla}\times\vec{H}(\vec{r},t) - \vec{J}_P(\vec{r},t) - \vec{J}_{free}(\vec{r},t))) \mp i\sqrt{\frac{1}{2\mu_0}}\vec{\nabla}\times\vec{E}(\vec{r},t)\right) \tag{34}$$

Once again, using the definitions of total magnetic field provided by Eq. (30), one arrives at

$$\vec{\nabla}\times\vec{H}(\vec{r},t) = = \sqrt{\frac{2}{\mu_0}}(\vec{\nabla}\times\sqrt{\frac{1}{2\mu_0}}\vec{B}(\vec{r},t) - \vec{\nabla}\times\vec{M}(\vec{r},t)). \tag{35}$$

One can also conveniently express the electric field as in

$$\vec{\nabla}\times\vec{E}(\vec{r},t) = \sqrt{\frac{2}{\epsilon_0}}\vec{\nabla}\times\sqrt{\frac{\epsilon_0}{2}}\vec{E}(\vec{r},t). \tag{36}$$

Expressions of Eqs. (30) and (35) can be plugged in Eq. (34) to obtain the equation of motion for complex bilinear vector $\vec{F^{\pm}}$.

$$\begin{aligned} i\partial_t \vec{F}^{\pm} &= c_0\vec{\nabla}\times(\pm\vec{F}^{\pm}) - i\sqrt{\frac{1}{2\epsilon_0}}(\vec{\nabla}\times\vec{M}(\vec{r},t) + \vec{J}_P(\vec{r},t) + \vec{J}_{free}(\vec{r},t)), \\ i\partial_t \vec{F}^{\pm} &= c_0\vec{\nabla}\times(\pm\vec{F}^{\pm}) - i\sqrt{\frac{1}{2\epsilon_0}}\vec{J}_{total}. \end{aligned} \tag{37}$$

Here, $\vec{J}_{total}$ is a combination of magnetization, polarization current, and free current as in

$$\vec{J}_{total} = \vec{\nabla}\times\vec{M}(\vec{r},t) + \vec{J}_P(\vec{r},t) + \vec{J}_{free}(\vec{r},t). \tag{38}$$

Once the equation of motion in Eq. (37) is established, it becomes clear that the current contribution from the matter side can be fed back to the time propagation of Maxwell's equations. Such a current contribution can come from any level of description of matter. In the particular case of the Drude medium,

the matter system is described by the scalar (isotropic) electric susceptibility, i.e., Drude susceptibility (for one pole), given by

$$\chi(\omega) = -\frac{\omega_p^2}{\omega^2 - i\omega\gamma_p}, \tag{39}$$

where ω_p is the frequency of the pth pole and γ_p is the corresponding relaxation time. We know the form of polarization in the frequency domain $\tilde{\mathbf{P}}(\omega)$

$$\tilde{\mathbf{P}}(\omega) = \epsilon_0\chi(\omega)\tilde{\mathbf{E}}(\omega). \tag{40}$$

and as in Fourier domain $f'(t) = i\omega\tilde{f}(\omega)$, then from the definition of $\vec{J_P}(t)$,

$$\tilde{\mathbf{J}}_P(\omega) = i\omega\vec{P}(\omega) = i\omega\epsilon_0\boldsymbol{\chi}(\omega)\vec{E}(\omega). \tag{41}$$

Now the definition of the polarization current permits the plugging in of the definition of the susceptibility seen in (39), when rearranged, results in

$$\begin{aligned} \tilde{\mathbf{J}}_P(\omega) &= -\epsilon_0\frac{\omega_p^2}{-i\omega - \gamma_p}\tilde{\mathbf{E}}(\omega), \\ (i\omega + \gamma_p)\tilde{\mathbf{J}}_P(\omega) &= \epsilon_0\omega_p^2\tilde{\mathbf{E}}(\omega). \end{aligned} \tag{42}$$

The advantage of Eq. (42) is that its inverse Fourier transform back into the time domain yields the auxiliary equation of motion

$$\partial_t\vec{J}_D(\vec{r},t) + \gamma_p\vec{J}_D(\vec{r},t) = \epsilon_0\omega_p^2\vec{E}(\vec{r},t). \tag{43}$$

for the current contribution from the medium. This procedure can also be applied to other susceptibility models [127]. The auxiliary equation for $\vec{J_P}$ can be tackled simultaneously with the Maxwell time-propagation, which was given in Eq. (24).

Keeping in mind that we focus on non-magnetic materials in the linear regime, one can consider the current contribution from polarization $\vec{J}_P(\vec{r},t)$ and neglect the magnetization and free charge contribution described in Eq. (38). Henceforth, the current supplied by the Drude medium is the total contribution, and one can state $\vec{J}_P(\vec{r},t) = \vec{J}_D(\vec{r},t)$ where $\vec{J}_D(\vec{r},t)$ denotes the current contribution from Drude medium.

4.5 Light-Matter Coupling

The coupling of light with matter can be described at different levels of theory. The most simplistic approach is to treat light as a classical electromagnetic wave and matter as classical charges. Then an electron bound to a nucleus is modeled as a damped harmonic oscillator driven by the electric field. The corresponding equation of motion in one direction then reads

$$m_e\ddot{x} + m_e\gamma\dot{x} + m_e\omega_0^2 x = -eE(t), \tag{44}$$

where m_e is the electron mass, ω_0 the natural frequency, *gamma* the damping constant, and $\vec{E}(\vec{r},t)(t)$ the electric field. The induced polarization can be understood as $P(t) = Nex(t)$, with N oscillators. This model explains linear optical response, but cannot capture discrete quantum levels or spontaneous emission, since it lacks a quantum description.

One moves to the semi-classical Rabi model to account for quantum features of matter while still treating light classically [128]. Here, the atom is described as a two-level quantum system coupled to a classical oscillating field, with the Hamiltonian

$$H = \frac{\hbar\omega_0}{2}\sigma_z - \vec{d}\cdot\vec{E}(t), \tag{45}$$

where ω_0 is the transition frequency, σ_z the Pauli matrix, and $\vec{d}$ the dipole operator with $\vec{d} = -e.\vec{r}$. While this model explains Rabi oscillations between ground and excited states, it lacks the spontaneous emission and photon statistics. The first fully quantum description of light–matter coupling, where both the atom and a single mode of the electromagnetic field are quantized, is the Jaynes–Cummings model [129] with

$$H = \hbar\omega_c\hat{a}^\dagger\hat{a} + \frac{\hbar\omega_0}{2}\sigma_z + \hbar g\left(\hat{a}^\dagger\hat{\sigma}_- + \hat{a}\hat{\sigma}_+\right), \tag{46}$$

where $\hat{a}$, $\hat{a}^\dagger$ are photon creation and annihilation operators, $\hat{\sigma}_\pm$ the raising and lowering operators of the two-level atom, and g the coupling constant. Eq. (46) is formulated under the rotating wave approximation (RWA), which captures vacuum Rabi splitting, spontaneous emission, and atom-photon entanglement. However, this approximation discards rapidly oscillating counter-rotating terms, which is justified when the light–matter coupling is weak, and the neglected terms average out over an optical cycle. The discarded terms describe virtual processes that do not obey energy conservation and become relevant in the ultrastrong coupling regime or for few-cycle and broadband fields.

When the RWA is lifted, one obtains the Rabi model, which retains both

energy-conserving and counter-rotating terms. This model becomes relevant when the light–matter interaction strength is significant.

For multiple atoms interacting with a common field mode, the Jaynes–Cummings framework generalizes to the Tavis–Cummings model [130], or the Dicke model [131], which explains collective quantum optical effects such as superradiance.

To expand beyond single atoms and a few level modes, one must turn to the full machinery of QED. The QED Hamiltonian quantizes both matter and the electromagnetic field across all modes. QED explains phenomena such as the Lamb shift. However, it is far too complex to apply directly to realistic many-electron systems such as molecules or solids.

For such systems, many-body approaches are employed. As it was detailed in previous chapters, the full TDSE equation can treat electrons interacting with strong laser pulses, but scales exponentially with system size. TDDFT provides a feasible route by reformulating the problem in terms of the electron density, leading to the time-dependent Kohn–Sham equations. This allows simulation of optical excitations, nonlinear responses, and high-harmonic generation in complex systems. In this work, we adopt the TDDFT formalism, where the matter is treated quantum mechanically while the electromagnetic field is described classically. The following subsections will elaborate on the different levels of theory we adopted concerning light-matter coupling.

4.5.1 Electric Dipole Approximation EDA

The spatial part of the electric field $\vec{E}(\vec{r},t)$ can be expressed as

$$\exp\left(-i\vec{k}\cdot\vec{r}\right) = 1 + i\vec{k}\cdot\vec{r} + \frac{(i\vec{k}\cdot\vec{r})^2}{2!} + ... \tag{47}$$

which corresponds to the Taylor expansion of the exponential $\vec{k}\cdot\vec{r}$ term around $\vec{r}=\vec{0}$. Here, keeping in mind that the wave vector $\vec{k}$,

$$|\vec{k}| = \frac{\omega}{c} = \frac{2\pi}{\lambda}, \tag{48}$$

where ω denotes the frequency, scales inversely with the wavelength λ.

When it comes to incorporating electromagnetic fields in the Hamiltonian, the EDA is a common procedure. When the wavelength is much larger than the size of the system, one can argue that for an electromagnetic field of the form $A_0 e^{i\vec{k}\cdot\vec{r}-\omega t}$, the term $\vec{k}\cdot\vec{r}$ is small and its expansion can be truncated at the first

term in Eq. (47), which effectively reduces to

$$\exp\left(-i\vec{k}\cdot\vec{r}\right) = 1 + i\vec{k}\cdot\vec{r} + \frac{(i\vec{k}\cdot\vec{r})^2}{2!} + ... \approx 1. \tag{49}$$

The EDA approximation seen in Eq. (49) results in the omission of the spatial dependence of the electromagnetic field, which is then expressed solely by its temporal dependence $\vec{E}(t)$, or within the velocity gauge $\vec{A}(t)$. When one accounts for the spin dynamics under the effect of the magnetic field $\vec{B}(t)$ via the Zeeman term $\frac{|e|}{m}\vec{B}(t)\cdot\hat{s}$ and effective time dependent potential term $v[n](\vec{r},t)$, one arrives at the Hamiltonian

$$\mathcal{H}^{(\mathrm{DIP})} = \frac{1}{2m}\left(-i\hbar\nabla + \frac{|e|}{c}\vec{A}(t)\right)^2 + \frac{|e|}{m}\vec{B}(t)\cdot\hat{s} + v[n](\vec{r},t). \tag{50}$$

4.5.2 Identifying the Electromagnetic Beyond-Dipole Effects: Multipolar Expansion

The Hamiltonian defined within the full minimal coupling approach preserves the complete spatial dependence, therefore spans over all multipolar orders. Nevertheless, for the analysis we will carry on for the following sections, the need to identify the effects stemming from different orders and types of electromagnetic fields is raised. To do so, one needs to reformulate the Hamiltonian as a function of electric and magnetic fields, which are gauge independent, rather than the gauge-dependent potentials [125]. The Power-Zienau-Woolley (PZW) transformation,

$$\hat{U}_{PZW} = \exp\left[\frac{i}{\hbar}\int \vec{P}(\vec{r})\vec{A}(\vec{r})d^3r\right], \tag{51}$$

allows one to express the Hamiltonian in terms of electric and magnetic fields.

Keeping in mind that the electric field $\vec{E}(\vec{r},t)$ and the magnetic field $\vec{B}(\vec{r},t)$ are connected to the vector potential $\vec{A}(\vec{r},t)$, upon this transformation, one reaches the multipolar interaction Hamiltonian

$$\mathcal{H}^{M}_{int} = -\int \vec{P}(\vec{r})\cdot\vec{E}_{\perp}(\vec{r})d^3r - \int \vec{M}(\vec{r})\cdot\vec{B}(\vec{r})d^3r, \tag{52}$$

which is expressed in terms of electromagnetic fields. Here, $\vec{P}(\vec{r})$ refers to the polarization density while $\vec{M}(\vec{r})$ refers to the magnetization density. We also note that this expansion operates solely with the transversal part of the electric field.

Once the interaction Hamiltonian depends on the spatial form of electric and magnetic fields, the Taylor expansion of the fields around a fixed position $\vec{r_0}$ generates terms of different orders. This expansion is commonly referred to as the multipolar expansion. Then, the expression, which is truncated at the third term for the multipolar Hamiltonian, takes the form

$$\begin{aligned}\mathcal{H}_{total}^{(\mathrm{ME})} = &-\frac{\hbar^2}{2m}\nabla^2 + |e|\vec{r}\cdot\vec{E}_{\perp}\left(\vec{r}_0,t\right) + \frac{1}{2}|e|(\vec{r}\cdot\boldsymbol{\nabla})\vec{r}\cdot\left(\vec{E}_{\perp}(\vec{r},t)\right)\Big|_{\vec{r}=\vec{r}_0} \\ &+ \mathrm{i}\frac{|e|}{2m}\vec{B}\left(\vec{r}_0,t\right)\cdot(\vec{r}\times\boldsymbol{\nabla}) + ... + V_{\mathrm{H}}[n](\vec{r},t) + V_{\mathrm{xc}}[n](\vec{r},t) + V_{\mathrm{nuc}}(\vec{r},t).\end{aligned} \tag{53}$$

One can already recognize that the first term is the electric dipole term $|e|\vec{r}\cdot\vec{E}_{\perp}\left(\vec{r}_0,t\right)$. It depends solely on the amplitude of the applied electric field, which is also the backbone of the EDA seen in Eq. (49). The next term

$$\frac{1}{2}|e|(\vec{r}\cdot\boldsymbol{\nabla})\vec{r}\cdot\left(\vec{E}_{\perp}(\vec{r},t)\right)\Big|_{\vec{r}=\vec{r}_0} = \frac{1}{2}|e|\sum_{ij} r_i\mathbb{Q}_{ij}r_j, \tag{54}$$

is one step further in the expansion of the electric field term $\vec{P}(\vec{r})\cdot\vec{E}_{\perp}(\vec{r})$, which is called the electric quadrupole term. This contribution does not only depend on the amplitude but also on the gradients of the applied field, see the term $\mathbb{Q}_{ij} = \partial_i\vec{E}_{\perp,j}\left(\vec{r},t\right)\Big|_{\vec{r}=\vec{r}_0}$ in Eq. (54), which is the electric field gradient tensor.

The following term is the magnetic dipole contribution

$$\mathrm{i}\frac{|e|}{2m}\vec{B}\left(\vec{r}_0,t\right)\cdot(\vec{r}\times\boldsymbol{\nabla}) = -\frac{|e|}{2m}\vec{B}\left(\vec{r}_0,t\right)\cdot\hat{\vec{L}}. \tag{55}$$

Notice that $\vec{L}$ is the orbital angular momentum operator, which highlights the interplay between the orbital motion of the electron and the magnetic field.

Since structured beams have spatial variations as well as temporal ones, it is common to account for at least up to the electric quadrupole term while analyzing their interaction with matter [132]. While the FMC approach covers the effects stemming from all the expansion terms, studying these three multipolar expansion terms will allow us to identify the source of the effects in the following sections.

4.5.3 Beyond the Electric Dipole Approximation: Full Minimal Coupling Approach

The quantum mechanical interaction of a charged particle with electromagnetic fields is described by

$$\mathcal{H} = \frac{1}{2m}\left(\vec{p} + \frac{|e|}{c}\vec{A}(\vec{r},t)\right)^2 + |e|\phi(\vec{r},t). \tag{56}$$

Here $\vec{p}$, e, and m are the momentum, charge, and mass of the particle, respectively. $\vec{A}(\vec{r},t)$ denotes the vector potential while $\Phi(\vec{r},t)$ corresponds to the scalar potential.

We work with the Coulomb gauge throughout the thesis. Henceforth, the vector potential is transversal, i.e. $\vec{A}(\vec{r},t)$ and scalar potential $\Phi(\vec{r},t)$ are chosen so that $\nabla \cdot \vec{A} = 0$ and $\Phi = 0$. With such constraints, while keeping in mind the definition of the canonical momentum

$$\vec{p} = -i\hbar\nabla, \tag{57}$$

Eq. (56) can be rewritten as

$$\mathcal{H} = \frac{1}{2m}\left(-i\hbar\nabla + \frac{|e|}{c}\vec{A}(\vec{r},t)\right)^2. \tag{58}$$

Here we choose to work with the velocity gauge, hence the Hamiltonian operates with vector potential via the term $\vec{p} - |e|\vec{A}(\vec{r},t)$ rather than electric field $|e|\vec{r}\vec{E}(\vec{r},t)$ which would be the case with length gauge. With this choice, electric and magnetic fields are calculated with

$$\vec{E}(\vec{r},t) = -\partial_t \vec{A}(\vec{r},t), \tag{59}$$

$$\vec{B}(\vec{r},t) = \nabla \times \vec{A}(\vec{r},t). \tag{60}$$

When one does not resort to EDA, this Hamiltonian keeps the spatial dependence as seen in the FMC case

$$\mathcal{H}^{(\mathrm{FMC})} = \frac{1}{2m}\left(-i\hbar\nabla + \frac{|e|}{c}\vec{A}(\vec{r},t)\right)^2 + \frac{|e|}{m}\vec{B}(\vec{r},t)\cdot\hat{\vec{s}} + v[n](\vec{r},t). \tag{61}$$

Here, the latter term $v[n](\vec{r},t)$ is the potential term expressed as a function of density $n(\vec{r},t)$ and also depends on the current $\vec{J}(\vec{r},t)$. This term encapsulates the potential terms according to the level of theory one aims to cover. This term can span over the Hartree potential $V_{\mathrm{H}}[n](\vec{r},t)$ which describes the effect of charge

density produced by other electrons on the electron, the exhange-correlation potential $V_{\mathrm{xc}}[n](\vec{r},t)$ which encapsulates many-body effects such as exchange interactions (effects caused by antisymmetry of fermionic wavefunction) and correlation effects (describing dynamic interactions between electrons where mean-field Hartree potential falls short), and $V_{\mathrm{nuc}}(\vec{r},t)$ which denotes the Coulomb potential of the nuclei. Then, the FMC Hamiltonian $\mathcal{H}^{(\mathrm{FMC})}$ [99], takes the form

$$\mathcal{H}^{(\mathrm{FMC})} = \frac{1}{2m}\left(-i\hbar\nabla + \frac{|e|}{c}\vec{A}(\vec{r},t)\right)^2 + \frac{|e|}{m}\vec{B}(\vec{r},t)\cdot\hat{\vec{s}} + V_{\mathrm{H}}[n](\vec{r},t) + V_{\mathrm{xc}}[n](\vec{r},t) + V_{\mathrm{nuc}}(\vec{r},t). \tag{62}$$

These Hamiltonians described here can then be plugged into the TDDFT framework described in Sec. 4.2 in order to tackle TDKS equations

$$-\mathrm{i}\frac{\partial}{\partial t}\varphi_i(\vec{r},t) = \mathcal{H}\varphi_i(\vec{r},t). \tag{63}$$

Then the corresponding current contribution from the matter side can be calculated from the Kohn-Sham states $\varphi_i(\vec{r},t)$. Here, the states ϕ_i are indexed over i, representing the occupied orbitals. As seen in Eq. (12) in previous sections, once summed up over states, one reaches the electronic probability density. For each state $\varphi_i(\vec{r},t)$, the current contribution is computed via

$$\vec{j}(\vec{r},t) = \frac{\hbar}{m}\,\mathrm{Im}\left(\varphi^*\nabla\varphi\right) + \frac{|e|}{mc}\vec{A}\varphi^*\varphi + \frac{\hbar}{2m}\vec{\nabla}\times\left(\varphi^*\hat{s}\varphi\right). \tag{64}$$

The term $\vec{j}(\vec{r},t)$ in Eq. (64) is the probability current density. Here, the first, second, and third terms represent the paramagnetic, diamagnetic, and magnetization current densities, respectively. We would also like to note that in the second term, the contribution of exchange–correlation vector potential $\vec{A}_{xc}$ to vector potential $\vec{A} = \vec{A}_{ext} + \vec{A}_{xc}$ is discarded, since we remain within TDDFT framework. Probability current density $\vec{j}(\vec{r},t)$ is connected to the total electric current density $\vec{J}(\vec{r},t)$ [43, 133] with

$$\vec{J}(\vec{r},t) = -|e|\vec{j}(\vec{r},t). \tag{65}$$

4.5.4 Forward-Backward Coupling

Computing the total electric current density from the matter side is crucial because it enables its application in Maxwell's equations. The total current contribution is the tool to connect the matter system to the electromagnetic field. The current computed in Eq. (64) is then converted into total electric current den-

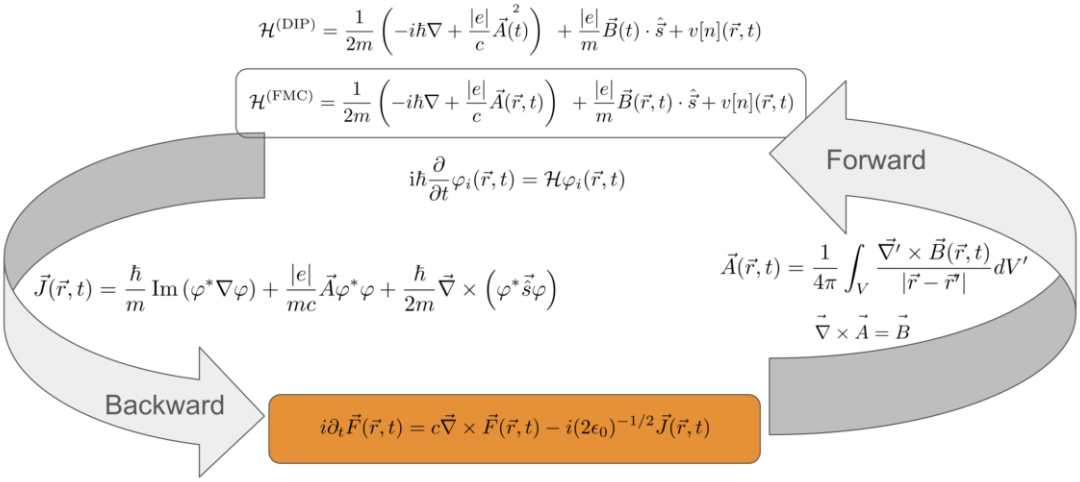

Figure 1: A schematic summarizing the forward-backward coupling approach followed while modeling light-matter interaction. We note that this scheme is valid for both TDSE and TDDFT frameworks.

sity and shipped to the equation of motion for Maxwell's equations in Riemann-Silberstein formalism described in Eq. (24). Here, the side condition of modified Gauß's law is applied as seen in Eq. (23). The vector potential is computed from the instantaneous magnetic field through the solution of Poisson's equation [134]

$$\vec{A}\left(\vec{r},t\right) = \nabla \times \int \frac{\vec{B}\left(\vec{r}',t\right)}{4\pi|\vec{r}-\vec{r}'|}\,\mathrm{d}^3r'. \tag{66}$$

This provides the chance of coupling the electromagnetic field back to the matter side: With the newly obtained electric and magnetic fields, one can compute the vector potential $\vec{A}(\vec{r},t)$ and feed it back to the Hamiltonians of Eqs. (50) and (61) alongside the computed magnetic field $\vec{B}(\vec{r},t)$.

At this point, the gauge choice should be highlighted: Throughout this thesis, we operate within the Coulomb(radiation) gauge. As mentioned in Sec. 4.5.3, this choice imposes that the vector potential $\vec{A}$ is kept divergence-free. This choice enables the extraction of the vector potential from the instantaneous magnetic field shown in Eq. (66).

With the recipe described above, one has the option to couple matter systems with electromagnetic fields in a forward-backward loop. While calculating the electromagnetic field and introducing them to the matter side is *'forward coupling'*, shipping the current contribution from the matter side to the electromagnetic simulation and dynamically updating the fields is called *'backward coupling'* throughout this work. When the electromagnetic response is coupled

back to the matter system, we call this bidirectional scheme *'forward-backward coupling'*. This provides a self-consistent framework that allows one to investigate different contributions. Added on top of the option of employing both dipole and beyond-dipole approaches, this scheme becomes a powerful tool to discover and identify new phenomena in light-matter interactions. In the following sections, we will apply this tool to a variety of examples spanning from Cherenkov radiation to high harmonic generation.

4.6 Twisted Light in the form of Bessel Beams

Light beams carrying orbital angular momentum, also referred to as twisted light, possess the unique characteristic of carrying a nonzero projection of the orbital angular momentum (OAM) onto the propagation direction. This special feature has paved the way to gain a deeper understanding of the role played by OAM in light-matter interactions. The possible applications of vortex-light beams are numerous, spanning from optical manipulation [4, 5], quantum information [9, 10] to imaging and sensing applications [6–8]. These beams can enable OAM based pump–probe techniques which have the potential to detect chiral or topological responses that ordinary plane waves cannot detect. A deeper understanding of twisted light interacting with quantum descriptions of matter is mandatory, and its inherent spatial dependence makes the twisted light an excellent candidate for beyond-dipole investigations.

Twisted light has phase structuring effects which cause spatial inhomogeneity in the transversal plane as depicted in panel b of Fig. 2. This phase structuring can be seen in

$$\vec{A}(\vec{r},t) \propto \exp\Big(-i\omega t + i\vec{k}\cdot\vec{r}\Big)\exp(im\phi)J_m(k_\perp r), \tag{67}$$

where a general form for twisted light is provided: the vector potential $\vec{A}(\vec{r},t)$ has the usual plane wave ansatz $\exp\Big(-i\omega t + i\vec{k}\cdot\vec{r}\Big)$ which propagates through time and space as a function of frequency ω, time t, wave vector $\vec{k}$ and position $\vec{r}$. Here, the term $\exp(im\phi)$ implies a phase structuring in the field on the order of m since $\phi = atan(\frac{y}{x})$ is the azimuthal angle, while the Bessel function $J_m(k_\perp r)$ causes the variation of the field along the transversal distance from the beam axis.

In this chapter, we provide the exact Bessel beam formulation we have implemented and employed for our calculations. The formulation described here is also implemented in the Octopus code, offering the first integrated software platform for combining exotic beam profiles with TDDFT simulations.

If a monochromatic field is assumed, the vector potential can be decomposed

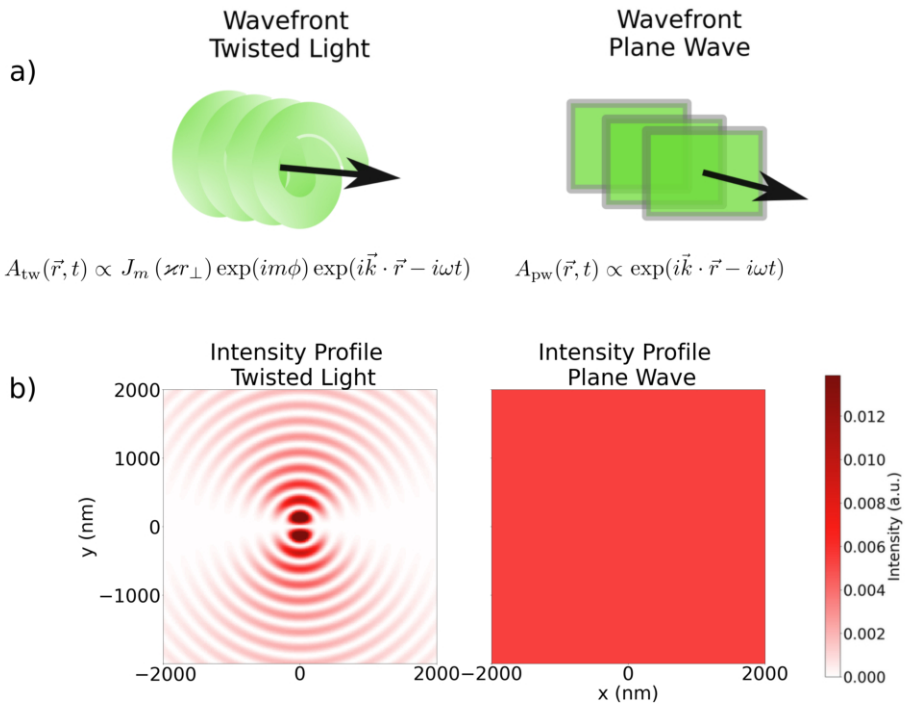

Figure 2: a) The comparison of the wave fronts of twisted light (light with orbital angular momentum) and a plane wave. As the wavefront of a plane wave would indeed be planar, the rotation around the propagation axis causes the wavefront of the twisted light to assume a screw-like shape. b) The qualitative comparison of transversal intensity profiles as time snapshots. While the transversal plane of a plane wave is uniform in intensity, the Bessel function governing over radial direction (in xy plane) paves the way to structured intensity for a twisted beam.

in its spatial and temporally dependent parts. This separation will also be useful to go beyond monochromatic waves and apply the envelopes to the pulses: We will employ spatially dependent envelope expressions provided in Sec. 4.8 to turn continuous Bessel waves into pulses in the following sections. Here in this chapter, we will deal with the spatially structured part first, and we will assume propagation as a function of time per the temporal exponential.

4.6.1 Bessel Beams: Spatially Dependent Vector Potential Formulation

In the present work, we restrict ourselves to the case of Bessel beams when it comes to electromagnetic fields with orbital angular momentum content. These beams possess the frequency ω, helicity λ, as well as projections of the linear wave vector k_z and total angular m momenta onto the propagation direction. The z axis is fixed as the propagation direction in our formulation. The Bessel-wave twisted field is described by the vector potential separated in temporal and

spatial parts as $\vec{A}^{(\mathrm{tw})}_{\varkappa m k_z \lambda}(\vec{r},t) = \vec{A}^{(\mathrm{tw})}_{\varkappa m k_z \lambda}(\vec{r}) e^{-i\omega t}$. The spatially dependent part is

$$\vec{A}^{(\mathrm{tw})}_{\varkappa m k_z \lambda}(\vec{r}) = i^{\lambda - m} A_0 \int \frac{e^{im\varphi_k}}{2\pi k_\perp} \delta\left(k_\perp - \varkappa\right) \delta\left(k_\parallel - k_z\right) \vec{A}^{(\mathrm{pl})}_{\vec{k}\lambda}(\vec{r}) d^2k \perp dk_\parallel, \tag{68}$$

where $\vec{A}^{(\mathrm{pl})}_{\vec{k}\lambda}(\vec{r}) = \vec{\varepsilon}_{\vec{k}\lambda} e^{i\vec{k}\cdot\vec{r}}$ is the vector potential describing plane wave light without orbital angular momentum content, $\vec{\varepsilon}_{\vec{k}\lambda}$ is the polarization vector, $k_\parallel$ and $k_\perp$ are the longitudinal and transversal components of the momentum $\vec{k}$, respectively, and $\varkappa = \sqrt{\omega^2 - k_z^2 c^2}$ is the well-defined transversal momentum of the Bessel beam, and A_0 is the amplitude of the vector potential. From Eq. (68), it is visible that Bessel states represent a cone comprised of plane waves with the opening angle θ_k

$$\theta_k = \arctan\left(\frac{\varkappa}{k_z c}\right), \tag{69}$$

in momentum space [25]. Once the integral in Eq. (68) is performed, the following expression is reached

$$\vec{A}^{(\mathrm{tw})}_{\varkappa m k_z \lambda}(\vec{r}) = (-\lambda) A_0 e^{ik_z z} \sum_{\mu=0,\pm1} d^1_{\mu\lambda}\left(\theta_k\right) e^{i\varphi_r(m-\mu)} i^{\lambda-\mu} J_{m-\mu}(\varkappa r_\perp) \vec{e}_\mu. \tag{70}$$

Here, J_n represents the Bessel function of the first kind, $\vec{r} = \left(r_\perp, \varphi_r, r_\parallel\right)$ is a postion vector in cylindrical coordinates, $r_\perp$ is the perpendicular component of $\vec{r}$, $d^1_{\mu\lambda}\left(\theta_k\right)$ is a small Wigner matrix described below. The small Wigner matrices depend on both opening angle and helicity of the beam λ as follows

$$d^1_{\mu\lambda}\left(\theta_k\right) = \begin{cases} \frac{\sin\theta_k}{\sqrt{2}}\lambda, & \text{if } \mu = 0 \\ \frac{1+\lambda\cos\theta_k}{2}, & \text{if } \mu = 1 \\ \frac{1-\lambda\cos\theta_k}{2}, & \text{if } \mu = -1 \end{cases}. \tag{71}$$

Here, $\vec{e}_\mu$ are eigenvectors of the spin projection operator $\hat{S}_z$ concerning the z axis, which form the (orthonormal) basis provided as:

$$\hat{S}_z \vec{e}_\mu = \mu \vec{e}_\mu \quad \hat{S}_z = -i \begin{pmatrix} 0 & 1 & 0 \\ -1 & 0 & 0 \\ 0 & 0 & 0 \end{pmatrix}.$$

The eigenvectors in Cartesian coordinates are explicitly:

$$e_0 = \begin{pmatrix} 0 \\ 0 \\ 1 \end{pmatrix}, \quad e_{\pm1} = \frac{\mp 1}{\sqrt{2}} \begin{pmatrix} 1 \\ \pm i \\ 0 \end{pmatrix}.$$

4.6.2 Formulation in Cartesian Coordinates

We implement the formula in the three-dimensional cartesian grid of octopus. The corresponding components of $\vec{A}^{(\mathrm{tw})}_{\varkappa m k_z \lambda}(\vec{r}) = (A_x(\vec{r}), A_y(\vec{r}), A_z(\vec{r}))$ in cartesian coordinates are

$$\begin{aligned}
A_x &= (-\lambda)\frac{1}{\sqrt{2}} A_0 e^{ik_z z} e^{im\varphi_r (e^{i\varphi_r}} d^1_{-1\lambda}(\theta_k)\, J_{m+1}\left(\frac{\varkappa r_\perp}{c}\right) i^{\lambda+1} \\
&\quad - e^{-i\varphi_r} d^1_{1\lambda}(\theta_k)\, J_{m-1}\left(\frac{\varkappa r_\perp}{c}\right) i^{\lambda-1}), \\
A_y &= \left(\frac{\lambda i}{\sqrt{2}}\right) A_0 e^{ik_z z} e^{im\varphi_r} (e^{i\varphi_r} d^1_{-1\lambda}(\theta_k)\, J_{m+1}\left(\frac{\varkappa r_\perp}{c}\right) i^{\lambda+1} \\
&\quad + e^{-i\varphi_r} d^1_{1\lambda}(\theta_k)\, J_{m-1}\left(\frac{\varkappa r_\perp}{c}\right) i^{\lambda-1}), \\
A_z &= (-\lambda) A_0 e^{ik_z z} i^\lambda e^{im\varphi_r} d^1_{0\lambda}(\theta_k)\, J_m\left(\frac{\varkappa r_\perp}{c}\right).
\end{aligned} \tag{72}$$

Here, the Wigner functions d are given by Eq. (71), cylindrical and cartesian components are connected such that $r_\perp = \sqrt{x^2+y^2}$, $\varkappa = \sqrt{\omega^2 - k_z^2 c^2}$, $k_z = \frac{\varkappa}{\tan(\theta_k) c}$, $\tan(\phi_r) = \frac{y}{x}$. A further simplification is possible: λ is the indicator of helicity, and one can restrict the formulation so that either right or left-handedness is chosen, i.e., $\lambda = \pm 1$. Then, the reformulated cartesian components become

$$A_x = \frac{1}{\sqrt{2}} A_0 e^{ik_z z} e^{im\varphi_r} (e^{i\varphi_r} d^1_{-1\lambda}(\theta_k)\, J_{m+1}\left(\frac{\varkappa r_\perp}{c}\right) + e^{-i\varphi_r} d^1_{1\lambda}(\theta_k)\, J_{m-1}\left(\frac{\varkappa r_\perp}{c}\right)), \tag{73}$$

$$A_y = \left(\frac{i}{\sqrt{2}}\right) A_0 e^{ik_z z} e^{im\varphi_r} (-e^{i\varphi_r} d^1_{-1\lambda}(\theta_k)\, J_{m+1}\left(\frac{\varkappa r_\perp}{c}\right) + e^{-i\varphi_r} d^1_{1\lambda}(\theta_k)\, J_{m-1}\left(\frac{\varkappa r_\perp}{c}\right)),$$

$$A_z = -A_0 e^{ik_z z} i e^{im\varphi_r} d^1_{0\lambda}(\theta_k)\, J_m\left(\frac{\varkappa r_\perp}{c}\right).$$

We note that the real parts of the formulation

$$\begin{aligned}
Re(A_x e^{-i\omega t}) &= \frac{A_0}{\sqrt{2}} [\cos(k_z z + \phi_r(m+1) - \omega t) d^1_{-1\lambda}(\theta_k)\, J_{m+1}\left(\frac{\varkappa r_\perp}{c}\right) \\
&\quad + \cos(k_z z + \phi_r(m-1) - \omega t) d^1_{1\lambda}(\theta_k)\, J_{m-1}\left(\frac{\varkappa r_\perp}{c}\right)], \\
Re(A_y e^{-i\omega t}) &= \frac{A_0}{\sqrt{2}} [\sin(k_z z + \phi_r(m+1) - \omega t) d^1_{-1\lambda}(\theta_k)\, J_{m+1}\left(\frac{\varkappa r_\perp}{c}\right) \\
&\quad - \sin(k_z z + \phi_r(m-1) - \omega t) d^1_{1\lambda}(\theta_k)\, J_{m-1}\left(\frac{\varkappa r_\perp}{c}\right)], \\
Re(A_z e^{-i\omega t}) &= A_0 d^1_{0\lambda}(\theta_k)\, J_m\left(\frac{\varkappa r_\perp}{c}\right) \sin(k_z z + m\phi_r - \omega t),
\end{aligned} \tag{74}$$

is used to compute observables such as the electric field and the magnetic field [135].

4.6.3 Applying Paraxial Approximation to Bessel Beams

A frequently used approach employed in twisted electromagnetic fields that propagate predominantly along a single axis is the paraxial approximation. This approximation assumes that transverse variations occur on length scales much larger than the optical wavelength. Under this condition, Maxwell's equations are simplified to the wave equation form that admits well-known solutions such as Gaussian and Laguerre–Gaussian beams.

However, this approximation breaks down in the presence of strong envelopes, strong focusing and when longitudinal fields are relevant. This occurs for tightly focused beams with large aperture, for beams carrying large OAM exhibiting strong transverse gradients, and for ultrashort or broadband pulses where the slowly varying envelope approximation no longer holds. In such nonparaxial regimes, longitudinal field components become significant.

Physically, the beam divergence or opening angle must remain small for paraxial approximation to hold. In this regime, the electromagnetic field is predominantly transverse, longitudinal field components are negligible, and polarization and spatial degrees of freedom remain approximately decoupled. This setup depends on the opening angle θ_k. Since this angle describes the ratio of transversal wave vector components to the one in the propagation axes as seen in Eq. (69), such an approximation implies that the propagation takes place strictly in one direction. Throughout this thesis, we impose the condition $\theta_k \approx 5^\circ$ when residing in the paraxial regime.

Applying the paraxial approximation, i.e. $\sin(\theta_k) \approx \theta_k$ and $\cos(\theta_k) \approx 1$, and reordering terms which depend on the zeroth order of θ_k, we arrive at $A_z \approx 0$.

$$
\begin{aligned}
A_x &\approx \frac{1}{\sqrt{2}} A_0 e^{ik_z z} e^{im\varphi_r} (e^{i\varphi_r} \frac{1-\lambda}{2} J_{m+1}\left(\frac{\varkappa r_\perp}{c}\right) + e^{-i\varphi_r} \frac{1+\lambda}{2} J_{m-1}\left(\frac{\varkappa r_\perp}{c}\right)), \quad (75)\\
A_y &\approx \left(\frac{i}{\sqrt{2}}\right) A_0 e^{ik_z z} e^{im\varphi_r} (-e^{i\varphi_r} \frac{1-\lambda}{2} J_{m+1}\left(\frac{\varkappa r_\perp}{c}\right) + e^{-i\varphi_r} \frac{1+\lambda}{2} J_{m-1}\left(\frac{\varkappa r_\perp}{c}\right)),\\
A_z &\approx 0.
\end{aligned}
$$

The paraxial approximation also implies that $m = m_{oam} + \lambda$, and the angular momentum number m_{oam} and helicity λ are separable. Then the formulation takes the shape below, which constitutes the spatially dependent part of the

general form in Eq. (67).

$$
\begin{aligned}
A_x &\approx \frac{1}{\sqrt{2}} A_0 e^{ik_z z} e^{im_{oam}\varphi_r} J_{m_{oam}}\left(\frac{\varkappa r_\perp}{c}\right), \\
A_y &\approx \left(\frac{i\lambda}{\sqrt{2}}\right) A_0 e^{ik_z z} e^{im_{oam}\varphi_r} J_{m_{oam}}\left(\frac{\varkappa r_\perp}{c}\right), \\
A_z &\approx 0.
\end{aligned} \tag{76}
$$

4.6.4 Construction of a Linearly Polarized Bessel Beam

The formulation we elaborated in the preceding sections covers the exact formulation of Bessel beams, which is accompanied by circular polarization (helicity $\lambda \pm 1$). However, circularly polarized pulses are not a good fit for studying high harmonic generation in spherically symmetrical atomistic systems: Once the electron is driven away from the nucleus, the recombination is subsequently suppressed in the presence of a circularly polarized beam. Therefore, a linearly polarized Bessel beam is required: Following the formulation of [29, 136, 137], we arrive at

$$
\vec{A}^{(\mathrm{tw})}_{lin}(\vec{r},t) = \frac{1}{\sqrt{2}}\left[\vec{A}^{(\mathrm{tw})}_{m_{\gamma_1},\lambda=+1,\theta_k}(\vec{r},t) + \vec{A}^{(\mathrm{tw})}_{m_{\gamma_2},\lambda=-1,\theta_k}(\vec{r},t)\right]. \tag{77}
$$

Here, the recipe is to combine two Bessel beams with opposite helicities. The same opening angle and the same amplitude for two beams with the condition $m_{\gamma_1} - m_{\gamma_2} = 2$ yields a Bessel beam which is linear in one direction and has the OAM number m, which is the average of the superposed beams. Nevertheless, we note that this linearization is not exact: the beam retains a component along the propagation direction with an amplitude on the order of 10^{-3} relative to the main beam amplitude, and a residual amplitude of approximately 10^{-4} in the suppressed transverse direction.

4.7 Multisystem Implementation in the Octopus code

This work spans a broad range of light–matter interaction phenomena starting from the atomic level (e.g., hydrogen atoms and benzene molecules) to microscopic nanoplasmonic structures with sizes on the order of several micrometers. Capturing such multiscale physics within a unified framework requires careful coordination between different physical subsystems, each governed by distinct equations of motion, numerical grids, and time resolutions. In this section, we outline the implementation strategies that enable this multiscale coupling, the *multisystem* framework of the Octopus code.

There are numerous descriptions of light and matter available in the Octopus code. Matter systems can include classically described point charges, wavepackets, periodic solids, finite systems describing atoms or molecules within the TDDFT formalism. Each system is initialized through a central *system factory*, which manages the setup of propagators, grids, and interactions. Systems coexisting in the simulation are called *partner systems*. Once initialized, the systems can communicate via the regridding interface and update their fields and potentials according to the prescribed clocks.

The interaction between systems includes the transfer of quantities such as electromagnetic fields (electric, magnetic fields, or vector potential), Coulomb forces, Lorenz force, potentials such as Lennard-Jones, and currents. Once these interactions are set up via the *interaction factory*, they are handled dynamically during real-time propagation. We note that the direction of the interaction can also be chosen freely, depending on the level of approximation. A system of clocks is used to determine when particular quantities need to be updated or exchanged between components. These clocks allow systems with different timescales to remain synchronized and enable efficient propagation without unnecessary recalculation. For instance, an atomistic system driven by an external field might not need to update its interaction with a current emitter at every timestep, depending on the scale separation.

To facilitate the exchange of information between systems defined on different spatial grids (e.g., transferring the Lorentz force from a Maxwell grid to an electronic system, or applying Coulomb potentials between charge distributions), a regridding mechanism is employed. This mechanism allows quantities to be interpolated across grids with different resolutions or extents. Two interpolation methods are supported: linear interpolation, which smoothly maps quantities between grids, and nearest-neighbor interpolation, which transfers quantities from the closest points. This flexibility supports different levels of approximation depending on the required accuracy and physical context.

Note that the transfer of some quantities may not be as crucial under certain approximations. For instance, under the EDA, the electric field of a laser can be evaluated directly from the electronic subsystem for the complete simulation box, without requiring full electromagnetic field propagation, and thus does not need explicit coupling to the Maxwell solver spatially across the grid. As we will see in the following chapter, we take advantage of such approaches and avoid unnecessary evaluation in the partner system when feasible.

4.8 Implementation of Position-dependent Laser beams in the Octopus code

To enable calculations extending beyond the EDA, a space-dependent electromagnetic source is necessary. This part can be supplied within the Maxwell solver of the Octopus code, or, in the case of other codes, a workflow combining a Maxwell solver code with the ab-initio code can be devised. However, solving Maxwell's equations for each simulation can be computationally demanding, both in terms of memory and time, especially when the laser field needs to be propagated across the entire simulation grid. This section describes the solution developed for this problem.

To ease computational load, a more efficient solution has been developed: a spatially dependent laser source that does not require full propagation. Integrated into the multi-system framework of the Octopus code with the name '*External-Source*', this approach significantly reduces computational overhead by avoiding the need to solve Maxwell's equations during every simulation step. Instead, the laser field is defined directly on the grid of the target system, making it possible to retain spatial dependence without the cost of time-domain propagation. Therefore, such a feature offers a good way to reduce the computation time and consumption of memory resources via the two advantages: Circumventing the usage of partial differential equation solvers, which would tackle Eqs. (23) and (24), and avoiding the unnecessary calculation of the fields in unused parts of the simulation box.

Through this feature, users can now prescribe laser fields that are explicitly dependent on both space and time. This represents a novelty for TDDFT software, where external fields are typically only a function of time, and spatial uniformity was assumed under the dipole approximation.

A great advantage of such a spatially dependent laser is the facilitation of employing complex beams such as Bessel pulses described in Sec. 4.6. The transversal planes describing such Bessel beams of the orders of $m = 1, 2, 3$ respectively can be seen in Fig. 3, panel a. It is visible from Sec. 4.6 that the formulation of Bessel beams is complex and dependent on numerous variables; therefore, the complete computation in a Maxwell solver requires great computational effort. A spatial laser system that calculates the beam properties when necessary helps the user to circumvent such a problem. The opportunity extends for users to make approximations: between the exact solution of Maxwell's equations and the approximated dipolar field, there is a playground. With such a feature, one can explicitly check parameters such as opening angle and rapidly test the importance of approximating certain variables.

Moreover, calculating a beam in a Maxwell solver requires the formulation to be an exact solution of Maxwell's equations. While this is indeed the case for Bessel beams, frequently used Laguerre-Gaussian beams, for instance, are rather solutions to the paraxial Helmholtz equation. Therefore, it is impossible to propagate such beams in a solver, but rather applying them as an external laser is preferable.

To see how space dependence naturally involves time propagation, a very useful example is the envelope imposed on an electromagnetic wave. This transforms the wave into a pulse, meaning that the wave becomes finite in time and space. A finite pulse in simulations, particularly in TDDFT, is essential both physically and numerically. Physically, it mirrors real experimental conditions where fields are time-localized, enabling the study of transient dynamics, as well as broadband excitation through a finite spectral width. Numerically, finite pulses ensure simulations remain stable, since the nonphysical energy accumulation (which would be caused by continuous waves) is avoided. This renders a clean initial state possible: Once the ground state of the matter system is combined with an initially zero electromagnetic field, one can entirely capture the dynamics within the simulation window.

Within the dipole approximation, conventional time-dependent laser schemes describe a temporal envelope

$$A(t) = A_0 \exp\left[i\left(-\omega t + \phi_p\right)\right] \exp\left(-\frac{(t-t_0)^2}{2\tau_0^2}\right). \tag{78}$$

Here, A_0 denotes the amplitude, ϕ_p is the phase of the beam, ω is the central frequency, and t refers to time. t_0 is the point in time where the pulse is initiated, τ_0 is the width in time, i.e., duration of the pulse. On the other hand, the same envelope can be expressed for a space-dependent pulse

$$A(\vec{r},t) = A_0 \exp\left[i\left(\vec{k}\cdot\vec{r} - \omega t + \phi_p\right)\right] \exp\left(-\frac{\left(\vec{k}\cdot(\vec{r}-\vec{r}_0)/|\vec{k}|\right)^2}{2\sigma^2}\right). \tag{79}$$

Here, the dependence of the pulse on the wave vector $|\vec{k}| = \omega/c$ is preserved as well as space dependent terms in the exponential describing a plane wave: $\exp\Big(i(\vec{k}\cdot\vec{r} - \omega t + \phi_p)\Big)$. The exponential describing the envelope is expressed now in space-dependent terms: $\vec{r}_0$ denotes the position where the pulse starts, and instead of the width in time τ_0, now the width in space σ_0 is used. Time propagation in Eq. (79) is implied through the nature of the wave: $|\vec{r}| = r_0 - ct$.

A benchmark that is used for the implementation is as follows: The expressions of the envelope described in Eqs. (78) and (79) should be equivalent in terms

of $A(\vec{r},t)$ for $\vec{r}=0$ or when $\vec{r}$ is the center of charge of the system. Therefore, one can compute the electromagnetic field and compare the two results stemming from the two expressions. Results of such a comparison are given in Fig. 3, panel b), which confirms that for identical parameters, the two implementations yield the same vector potential as a function of time, assuring the space-dependent implementation is working as intended.

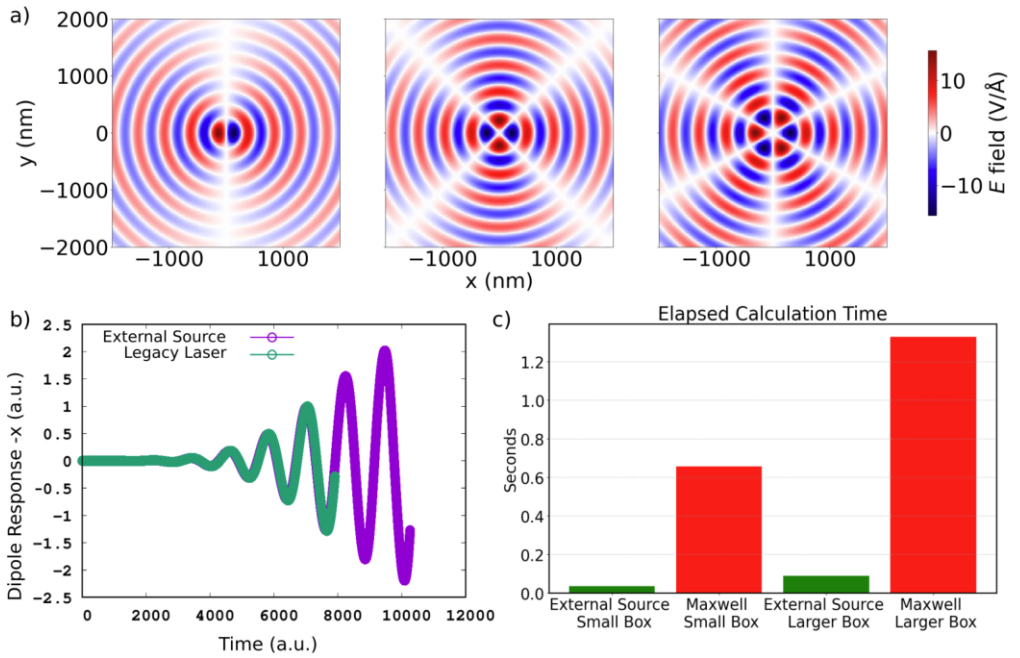

Figure 3: a) Electric fields of Bessel beams with orders $m=1,2,3$ respectively, implemented as spatial laser in the Octopus code. Time snapshots of the transversal xy plane are shown, while z is the direction of propagation. b) Benchmarking of the spatial laser with its solely time-dependent counterpart. Once the position is fixed as the center of charge for the system, both formulations should yield the same electromagnetic field, hence the same dipole excitement. Here, the results are compared as a function of time. c) Comparison of elapsed calculation time for the spatial laser and Maxwell solver. The advantage of the spatial laser grows as the size of the simulation box is increased.

We show the numerical advantage of implementing such a laser in panel c) of Fig. 3. Here, plane wave pulses are propagated first in a cubic simulation box with dimensions $3.0\times3.0\times3.0$ Å, with equal spacing of 0.2 Å. The simulation box contains a carbon atom, which is coupled to the electromagnetic field within the EDA. Two cases were tested: Green bars in Fig. 3 point to the case where the field is supplied with the spatial laser (called External Source in the code), while red bars refer to the case where the Maxwell solver is used for explicit computation of the electromagnetic field. The elapsed time in seconds to complete one timestep

(2.41888×10^{-3} fs) is measured and compared for the box in panel c of Fig. 3. Here, the same quantity is also compared for a larger box of $4.0 \times 4.0 \times 4.0$ Å, with equal spacing of 0.2 Å. Observing that the difference in elapsed calculation time between the External Source and Maxwell Solver tools is increased, it is clear to see that as one moves to larger grids, the advantage of spatial laser is important. All simulations for this demonstration were performed locally on a Debian 12 (Bookworm) machine with an AMD Ryzen 7 PRO 7840U CPU (8 cores, 16 threads), 28 GB RAM. Calculations were launched using Open MPI 4.1.4 with 2 MPI processes.

In summary, the full spatial laser implementation enables a practical and efficient route to explore physics beyond the electric dipole approximation, capturing spatial field variations while maintaining computational tractability.

5 Nanoplasmonics & Generation of Light with Archimedean Spirals*

Nanoplasmonics is the field that resides at the interface of optics and condensed matter science, focusing on the optical phenomena found in metallic systems structured at the nanoscale [138]. Emerged from classical scattering theory, nanoplasmonics gained momentum with the advancement of nanofabrication techniques. Particularly due to surface plasmons, i.e., propagating modes along the surface of a conductor, nanoplasmonics carried the physics to the subwavelength scale: this rendered miniaturized photonic circuits possible, which in turn entailed outstanding progress in sensing, imaging, data storage, and light manipulation [139].

Specifically, light with OAM, also referred to as twisted light or optical vortices, their orbital angular momentum content has significant implications for the study of light-matter interactions. The avenues opened by this new degree of freedom, represented by orbital angular momentum, include optical manipulation of particles [4, 5], as well as novelties in quantum information [9, 10], imaging [6, 7], and detection techniques with superresolution [8]. Naturally, there have been numerous experimental and theoretical studies tackling the interaction of optical vortices with matter spanning from photoionization with such beams [25–29], to the excitation of matter with twisted light in the low intensity regime [12–18, 140].

When combined, nanoplasmonic structuring of twisted electromagnetic fields enables a new knob for the control over light–matter interactions. Considering

*Parts of this chapter, including figures and text excerpts, are adapted from the author's previously published work: Albar, E.I., Bonafé, F.P., Kosheleva, V.P. et al. Time-resolved plasmon-assisted generation of optical-vortex pulses. Sci Rep 13, 14748 (2023), under the Creative Commons Attribution (CC BY 4.0) license.

that the nanoplasmonic systems provide the opportunity to localize, enhance, and spatially structure electromagnetic fields well below the diffraction limit, it is not surprising that they are frequently used for molding light. Customizing field topologies via nanoplasmonics in terms of phase, intensity, and OAM content allow unprecedented access to subwavelength phenomena. Particularly, the ability to imprint and reshape OAM onto incoming non-OAM plane waves through carefully engineered nanostructures has expanded the toolbox for optical control at the nanoscale, offering new handles for steering energy flow, tailoring optical selection rules, and driving novel light-induced dynamics [71, 141]. Henceforth, we focus here on this particular concept of generating OAM from a plane wave pulse.

Understanding the introduction of orbital angular momentum to an unstructured electromagnetic field is crucial for the development of new photonic technologies. The process of twisted light generation can be realized by a variety of structures, such as spiral phase plates [68], forked holograms [69], and q-plates [70]. In this work, we focus on the generation of such fields with gold Archimedean spirals [71], which offers a simple picture of phase structuring of the plane wave beam.

Gorodetski and colleagues experimentally demonstrated the emergence of vortex surface plasmon polaritons (VSPP), i.e., hybrid light-matter states residing at the surface of a conductor [76]. Subsequent studies have reported nanoscale platforms for the synthesis [142], real-time emergence [143], and beaming [144] of twisted light. Such studies were accompanied by finite-difference time-domain (FDTD) simulations that have addressed the mechanisms underlying the generation [77–79]. It has also been shown that vortex characteristics are not confined to the conductor surface, but rather extend to the vacuum [71, 72]. All of these results concerning SPPs motivate our study of the nanoplasmonic Archimedean spiral, which is a suitable candidate to focus on while addressing the SPP-driven mechanisms contributing to twisted light generation.

In this chapter, we present the first complete modeling of the dynamics of a short optical vortex pulse, tracing the process from the very formation of an OAM beam to the imparting of angular momentum onto point-like test charges. The observed susceptibility of the particle trajectories on the initial position across the transversal plane of the beam offers a sensitive diagnostic of the spatially varying orbital angular momentum density.

This chapter is organized as follows: We start with the details of the design process for the structure and its integration into the Maxwell solver part of the Octopus code. Then we move on to describe real-space real-time emergence of orbital angular momentum in the unstructured beam that is shone onto the spiral.

This work is a multiscale study: We employ point charges to test and characterize the produced local orbital angular momentum density. The chapter is concluded with a discussion of findings from the trajectories of test charges.

5.1 Design and Integration of Structures into Maxwell Simulation Box

Spiral phase plates, holograms, and Archimedean spirals imprint OAM onto the incoming beam mainly via their inherent phase structuring. The gaps or indentations in the structure diffract and delay the light, which results in the imprinting of phase structuring onto the incoming light field.

For the case of an Archimedean spiral, phase structuring is bound to the number of branches and the separation between the branches. The general form of the Archimedean spiral is given by

$$r(\varphi) = d_0 + \frac{d \bmod (m\varphi, 2\pi)}{2\pi}. \tag{80}$$

Here, $d_0 = \sqrt{x_0^2 + y_0^2}$ is the starting radius of the segmented Archimedean spiral branches, which then expand from the smallest radius around the center to reach $d_0 + d$. $\varphi = \arctan\left(\frac{y}{x}\right)$ represents the azimuthal angle, and mod is the modulus function giving the remainder of the division of $m\varphi$ by 2π. The number of segments in the spiral is determined by the parameter m, which is shown in panel a of Fig. 4 (for our OAM transfer investigation, we use $m = 4$). This is an analogy to the cross-section of OAM beams, the number of segments enforces the number of phase jumps of the emitted field, which is the fingerprint of the OAM number for electromagnetic fields.

The nanoplasmonic Archimedean spiral is designed first in OpenSCAD [145], a script-based 3D computer-aided modeling software that is used for programmable construction of complex geometries. We match the gap to the wavelength as seen in Fig. 4. We set the radius of the golden spiral to 9 microns, which is feasible for such nanoplasmonic golden structures. The spiral thickness in the propagation direction is 1.6 μm. Resulting geometric files are then transferred to the calculation grid in Octopus and are read in Octopus using the Computational Geometry Algorithms Library (CGAL) [146].

In real-space real-time simulations we perform in Octopus-code [100], we treat the grid points that overlap with the structure as points that emit the current response of the material. This means that the susceptibility is applied only inside the Drude material, while we solve Maxwell's equations in the vacuum for the external points. In this work, the classical Drude susceptibility model for a

linear, non-magnetic medium is used as described in Section 4.4. To describe the matter grid points with this susceptibility model, we employ previously reported parameters [147] for the Drude pole frequency ω_p and inverse relaxation time γ_p for gold, and calculate the susceptibility following Eq. (39).

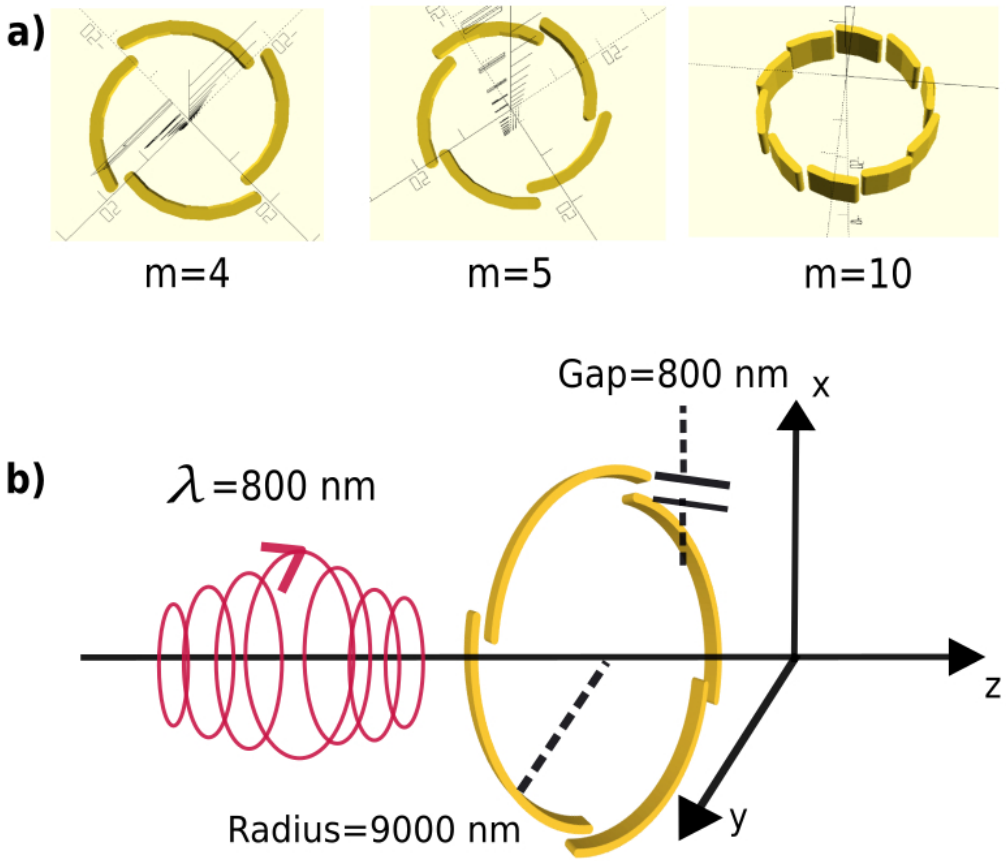

Figure 4: a) Archimedean spiral designs from OpenSCAD. The number of branches determines the number of phase jumps. We employ the Drude pole frequency and inverse relaxation time values for gold to describe a nanoplasmonic Archimedean spiral. b) Setup for the investigation of OAM generation in the spiral. The central wavelength of the incoming 8-cycle, right circularly polarized ultrashort pulse is matched to the separation between the branches. The radius of the spiral is set to 9 μm, while the spiral thickness in the propagation direction is 1.6 μm.

Since the gap between branches is expected to diffract the incoming light and introduce the phase structuring, multiples of the incoming wavelength are beneficial: This facilitates understanding the interference pattern of the produced field occurring in the central vacuum region. In this study, we employ a central wavelength of $\lambda = 800$ nm, which is standard for a Ti:Sapphire laser. An ultrashort pulse of 8 cycles with the said wavelength is then sent onto the nanoplasmonic structure. The pulse has no transversal structuring up until the interaction with the spiral: It has a plane wave form and is right circularly polarized. The electric

field has the form

$$\vec{E}(\vec{r},t) = \mathrm{Re}\{g(\vec{r})e^{i\vec{k}\cdot\vec{r}-\omega t}\vec{\varepsilon}_{\vec{k}\sigma}\}. \tag{81}$$

Here, the polarization vector $\vec{\varepsilon}_{\vec{k}\sigma} = \frac{1}{\sqrt{2}}(1,\, \sigma i,\, 0)^{\mathrm{T}}$ points to circularly polarized light with a helicity $\sigma = 1$, denoting the right-handedness, and $g(\vec{r})$ is the Gaussian envelope function described as

$$g(\vec{r}) = E_0 e^{-\left(\frac{\vec{k}\cdot(\vec{r}-\vec{r_o})}{|\vec{r}|}\right)^2 \frac{1}{2w^2}}. \tag{82}$$

The maximum pulse amplitude E_0 shown in Eq. (82) is 0.02 V/nm; this justifies the restriction of our analysis to the linear regime.

In the envelope that restricts the electromagnetic field in space and time, w is the half pulse width in space, and it corresponds to 4λ in the present study. This renders the used pulse to be ultra-short, while broadening its span over the frequencies surrounding the central frequency of 1.5498 eV. r_o marks the spatial offset from the origin of the pulse to the simulation box, which is arranged with the purpose that at the initial timestep $t = 0$ the pulse starts already inside the simulation box, as depicted in Fig. 6.

The incident pulse and nanoplasmonic golden spiral are combined in a real space simulation box of size of 15.9 × 15.9 × 10.6 μm. The spacing used to discretize the system is 52.9 nm in every direction. We use a time step of 2.65×10^{-3} fs for the time propagation. The total simulation time is 45 fs. The computational method to propagate Maxwell's equations in real time is based on the Riemann-Silberstein (RS) formalism, which is detailed in Section 4.3. The corresponding modified Gauß's Law and equation of motion are seen in Eqs. (23) and (37). For the linear medium, we can express the total current density $\vec{J}_{total}(\vec{r},t)$ as $\vec{J}(\vec{r},t) = \nabla \times \vec{M}(\vec{r},t) - \partial_t \vec{P}(\vec{r},t) - \vec{J}_{free}(\vec{r},t)$. Here, $M(\vec{r},t)$ and $P(\vec{r},t)$ are the magnetization and polarization, respectively. Following the spirit of Section 4.4, we restrict ourselves to the non-magnetic case in the linear regime, hence the currents are solely stemming from polarization $\vec{P}(\vec{r},\omega) = \epsilon_0 \chi(\vec{r},\omega)\vec{E}(\vec{r},\omega)$, where χ is the scalar (isotropic) electric susceptibility shown in Eq. (39).

When propagating the matter side and the electromagnetic side together, one has to solve the auxiliary differential equation involving the induced current density, given in Eq. (43) [127]. We use a Runge-Kutta scheme to tackle this simultaneous propagation in the time domain.

Finally, the simulation box needs absorbing boundaries. In Finite-Difference Time-Domain (FDTD) or Finite Element Methods (FEM) calculations, a finite simulation box implies artificial numerical boundaries imposed on Maxwell's equa-

tions. When reaching the simulation box boundary, the electromagnetic waves can then artificially scatter and reflect, displaying erroneous behavior. To prevent this, Perfectly Matched Layer (PML) boundaries are used: Such a layer acts as an artificial absorber which causes the incident wave at the boundary to be propagated without reflection at the interface [148]. The wave that passes through the boundary to the said artificial layer is attenuated until it is fully absorbed. Then, the outer edge of the simulation box is safe to truncate, since the wave in question is handled. The attenuation follows an artificial conductivity profile σ_i assigned to the PML region

$$\sigma_i(i) = \left(\frac{|i| - b_i}{L_i - b_i}\right)^{q_{PML}} \sigma_{i,max}, \tag{83}$$

where i is the Cartesian direction coordinate $i \in (x, y, z)$ while b_i and L_i are inner simulation box size and total box size including PML layer thickness wrapped around the inner part in that direction[43, 127]. The maximum conductivity $\sigma_{i,max}$ value is determined as

$$\sigma_{i,max} = -\frac{\epsilon_0(q+1)ln(R(0))}{2\mu_0(L_i - b_i)}. \tag{84}$$

The variable q_{PML} here is the PML power coefficient, and it is numerically screened by [125], and fixed at $q_{PML} = 3.5$ in this study. R_0 is the reflection coefficient, i.e., the knob for the tolerated reflection error, and it is set to 1.0×10^{-16} for our work. The simulation box size described above includes a PML region of 0.8 μm in each direction, which corresponds to 15 grid points to absorb the incoming wave safely.

We employ the setup described in this section and propagate an ultrashort pulse in the simulation box, which is incident on a golden nanoplasmonic Archimedean spiral. The following subsection describes the resulting time-resolved OAM behavior emerging in the simulation.

5.2 Probing the Emergence of Orbital Angular Momentum Generation in Time

The classically described, spatially resolved OAM density $\vec{L}(\vec{r}, t)$ is calculated from the electric and magnetic fields $\vec{E}(\vec{r}, t)$ and $\vec{B}(\vec{r}, t)$ [135].

$$\vec{L}(\vec{r}, t) = \frac{1}{c^2\mu_0}\vec{r} \times \left[\vec{E}(\vec{r}, t) \times \vec{B}(\vec{r}, t)\right] = \epsilon_0\vec{r} \times \left[\vec{E}(\vec{r}, t) \times \vec{B}(\vec{r}, t)\right]. \tag{85}$$

Since electromagnetic fields are evaluated instantaneously via the Riemann-Silberstein formalism, the OAM density then becomes a straightforward quantity to report. We implemented this output in theOctopus code and made use of the existing machinery to produce the output efficiently.

We first show the emergence of the OAM density in the electromagnetic field in a scaled-down, proof-of-concept simulation. In Fig. 5.2, a volumetric snapshot of the OAM density is provided where the pulse is halfway through the spiral. It is clearly visible that this quantity is introduced upon passing through the golden nanostructure, since before the spiral, the OAM density is minimal. Here, we report the OAM density in the z direction, which is the propagation direction of the pulse. We also observe that this quantity extends well beyond the span of the spiral, hinting at a consistent production of OAM density.

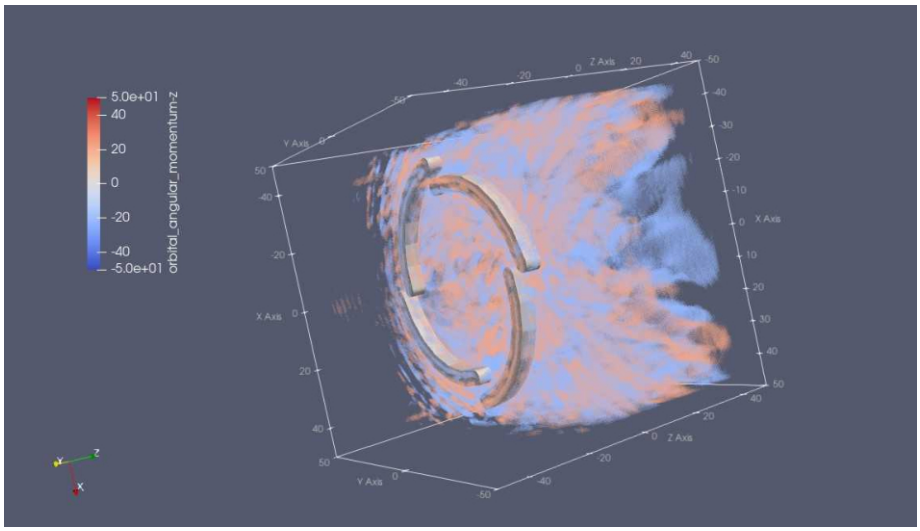

Figure 5: Volumetric Plot for the generation of orbital angular momentum, plotted for a proof-of-concept calculation. A snapshot where the pulse is halfway through the Archimedean spiral is shown.

To move on to a more detailed analysis, we employ the simulation box described in the previous section, and split the electromagnetic field into its external and induced components: $\vec{E}(\vec{r},t) = \vec{E}^{\text{ext}}(\vec{r},t) + \vec{E}^{\text{ind}}(\vec{r},t)$. Here, the external part propagates in the vacuum part of the box and is unaffected by scattering; it only serves to excite the spiral. On the other hand, $\vec{E}^{\text{ind}}(\vec{r},t)$ collects the response from the spiral. We would like to highlight that with this decomposition, $\vec{E}^{\text{ext}}$ corresponds directly to the pulse described in the previous section, which is engineered via the input parameters.

In Fig. 6, we report the results in terms of these components of the total electric field. The side section on the left marks the spiral as the gold area, and the external profile of $E_x^{\text{ext}}(\vec{r},t)$ component through the propagation axis (z) is shown in green, while its induced counterpart $E_x^{\text{ind}}(\vec{r},t)$ along the same

axis is plotted in blue. Here, the rows correspond to different time steps of the simulation: Snapshots from 0.0 fs, 15.9 fs, 21.2 fs, and 29.1 fs are provided.

We are interested in the z component of xy-plane averaged OAM density $L_z(\vec{r},t) \equiv L_z(x,y,z,t)$

$$\bar{L}_z(z,t) = \frac{1}{S_{xy}} \int\int |L_z(x,y,z,t)| dxdy. \tag{86}$$

Here, S_{xy} denotes the cross-sectional area of the simulation box. Then we can express this averaged quantity along the propagation axis as seen in the left side of Fig. 6.

As the induced field in Fig. 6 is shown only along the propagation axis on the left side, the vortex-like time resolved dynamics is better characterized by the averaged OAM density $\bar{L}_z(z,t)$ along the z-axis, which is shown in purple in Figure 6. We compute the OAM density considering the total electric and magnetic fields (external and induced) following the recipe of Eq. (85). We also decompose and plot the OAM density stemming from only the induced fields; it is plotted in red. The amplitude of the OAM density arising from the induced field alone is significantly smaller than that of the total field. Moreover, the induced-only OAM density traces the regions of strongest induced field intensity: it exhibits near-field peaks at the boundaries of the nanostructure and decays (although does not vanish) in amplitude as it propagates away from the spiral. The comparison between these two densities shows that the interference of the incident circularly polarized beam with the induced one plays a significant role in OAM density. On the other hand, the OAM density stemming from the total fields does not experience a significant change in amplitude after the interaction of the external pulse with the nanospiral, since its average profile is mostly dependent on the amplitude of the source pulse. However, it is delayed with respect to the external pulse envelope due to the contribution from emission that travels to free space.

The vertical dashed black lines in the left panels are the transversal cross-section planes plotted in the right panels of Figure 6. These are the middle of the spiral ($z = -2\mu$m) and a further plane ($z = 0$) to characterize the far field. Upon the arrival of the incident pulse to the spiral, the emitted radiation emanates from the branches and travels towards the center of the spiral, interfering with the central axis of the structure. This behavior is clearly visible in the cross-section of the emitted field at time snapshots of 15.9 fs, 21.2 fs, and 29.1 fs. The temporal resolution provided by these snapshots clearly demonstrates the geometric structure that the spiral imprints on the emitted field. In the case of a continuous wave, this interference would result in a clearer pattern. However, the ultrashort incident pulse induces many frequency components that acquire

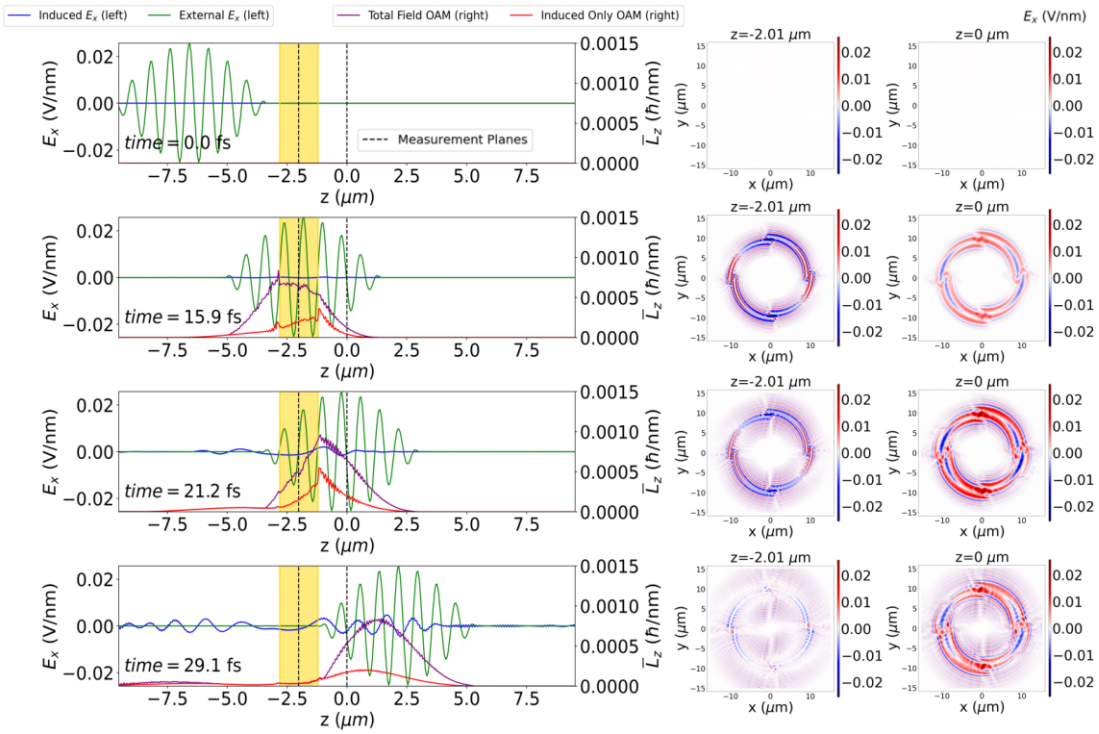

Figure 6: The left panels display the simulation box along the propagation axis, while the corresponding cross-sectional profiles are presented on the right. Each of the rows represents a snapshot in time at 0.0 fs, 15.9 fs, 21.2 fs, and 29.1 fs. The external and induced electric field components E_x, are shown in green and blue, respectively. The xy-integrated OAM density $\bar{L}_z(z,t)$ is given for two cases: The total field (external + induced) is purple, and the induced field is plotted in red. In the side views, vertical dashed black lines indicate the planes for which cross-sectional plots are provided. These two cross sections are located at the midpoint of the spiral ($z = -2\mu$m) and the center of the simulation box $z = 0$. Following the arrival of the external pulse at the spiral, the emitted radiation is seen to propagate towards its center, as shown in the cross-sections at 15.9 fs, 21.2 fs, and 29.1 fs. The behavior of the OAM density in the side view further demonstrates that the vortex-like character of the induced field persists and is not confined to the near field: It survives in the transverse components that radiate into the far field. The figure is reproduced with permission from E. I. Albar et al., *Sci. Rep.* **13**, 14748 (2023), licensed under CC BY 4.0.

different phase components.

In addition to the patterned field at the mid-plane of the spiral, the emission stays significant a few micrometers away. Such an induced field also carries a non-negligible OAM structuring, as seen in the snapshots at 21.2 fs and 29.1 fs, which is also confirmed by the corresponding OAM density in the left panel. This traveling component in the cross-section has a profile that resembles the one at the spiral plane but with a certain delay. Then, one can conclude that the vortex-like nature of the induced radiation survives the interaction: This behavior is not

only present in the near field but also accompanies the transverse component of the electromagnetic field that radiates far from the structure.

Another quantity that demonstrates the contribution of the external fields in the amplitude of the produced OAM density is the averaged energy density along the propagation axis. We calculate the energy density $\vec{W}$

$$\vec{W}(\vec{r},t) = \frac{\epsilon_0}{2}\vec{E}(\vec{r},t)^2 + \frac{2}{\mu_0}\vec{B}(\vec{r},t)^2. \tag{87}$$

We integrate it over the cross section in Eq. (88) with a similar procedure to the OAM and report it in Fig. 7.

$$\bar{W}(z,t) = \frac{1}{S_{xy}}\int\int |W(\vec{r},t)|dxdy. \tag{88}$$

Here, we highlight that the energy density reflects the contribution of the electric and magnetic fields. As seen in Eq. (85), the OAM is proportional to these quantities. In the circularly polarized case where both x and y components are present, the correlation between the magnitude of the energy density and the OAM becomes even more significant.

Once the effect of geometric phase structuring on the ultrashort pulse is confirmed, we simplify our model to dissect the local OAM further. We replace the Maxwell simulation in vacuum with external current sources directly, which mimics the emission from the golden Archimedean spiral. This will help to isolate the induced emission: Current emitters will have the same geometric structuring while being free of external incident pulse and its noise. Since the linear medium requires a fine mesh due to surface boundary conditions, the need to replace it with computationally cheaper current sources arises. The linear medium also suffers from spurious fields at the intricate parts of the design, such as the caps at the ends of branches. This replacement also nullifies such problems.

As a final argument in favor of currents, we investigate the OAM patterning of total and induced fields in Fig. 8. Here, three rows correspond to snapshots from three timesteps in the simulation: 15.9 fs, 42.2 fs, and 45.0 fs. We observe that even though the average OAM density depends on the amplitude of the electromagnetic fields, the patterning due to interference is very similar for both cases. This resemblance is particularly striking after the pulse passes through the spiral. This behavior implies that the overall OAM behavior is governed by the induced field. Henceforth, investigating the current emitters mimicking the induced field should provide reliable insights into the original linear medium setup.

The current density emitters are structured to have the shape of segmented

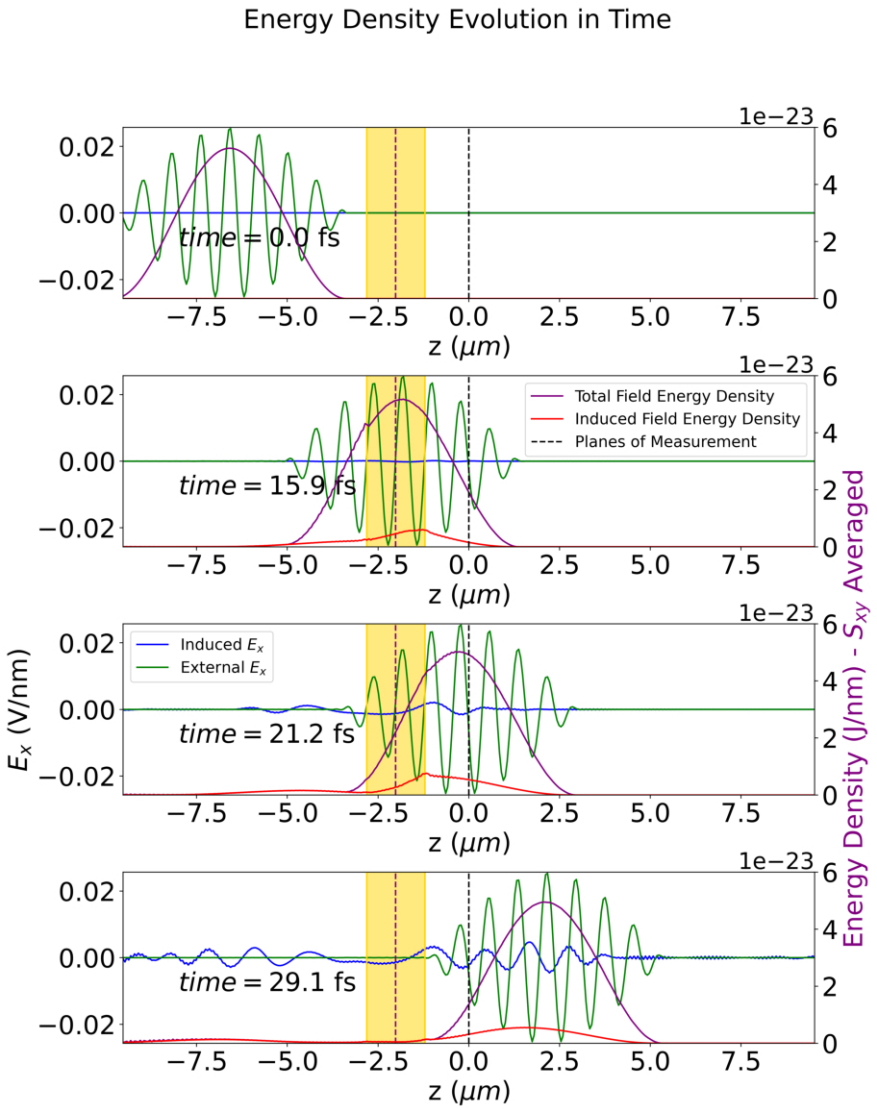

Figure 7: Time-dependent evolution of the energy density reported along propagation axis. Here, the left side indicates the evolution of the x component of the electric field while the right hand side of the graph shows that of the energy density described in Eq. (87). The snapshots correspond to 0.0 fs, 15.9 fs, 21.2 fs, and 29.1 fs. The figure is reproduced with permission form E. I. Albar et al., *Sci. Rep.* **13**, 14748 (2023), licensed under CC BY 4.0.

nanoplasmonic Archimedean spirals. Their space and time dependence are engineered to emulate the emission from the original nanoplasmonic spiral. The x and y components of the emitted current are shown in

$$J_x(x,y,z,t) = j_0 \exp\left(\frac{-\left(\sqrt{x^2+y^2} - r_0 - d\varphi\right)^2}{2\sigma^2}\right) \exp\left(\frac{-(t-t_0)^2}{2\tau^2}\right) \cos(\omega t), \tag{89}$$

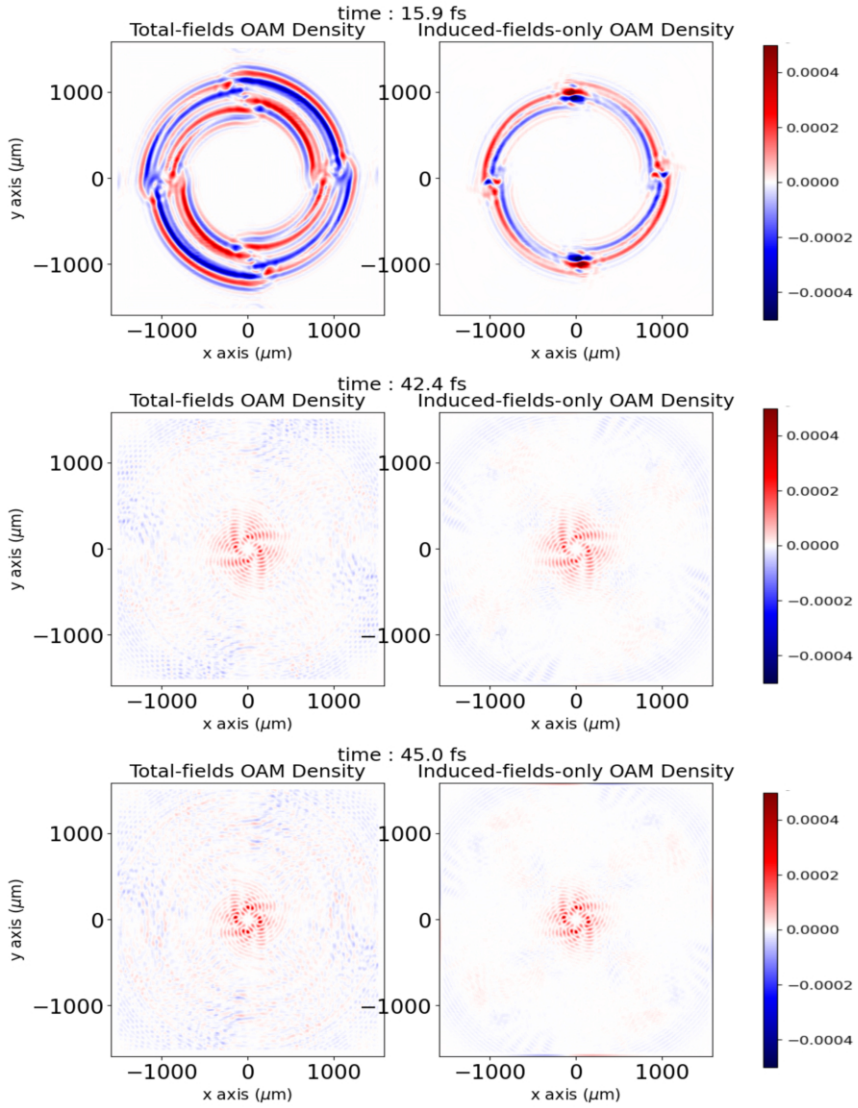

Figure 8: Comparison of cross-sectional OAM densities for total fields and isolated induced field. Since the patterns are quite similar, OAM density generated from current emitters is expected to reproduce the phase structuring from the original medium. Figure is reproduced with permission form E. I. Albar et al., *Sci. Rep.* **13**, 14748 (2023), licensed under CC BY 4.0.

$$J_y(x,y,z,t) = j_0 \exp\left(\frac{-\left(\sqrt{x^2+y^2} - r_0 - d\varphi\right)^2}{2\sigma^2}\right) \exp\left(\frac{-(t-t_0)^2}{2\tau^2}\right) \cos(\omega t + \pi/2), \tag{90}$$

whose shape then mimics the behavior given by Eq. (80). Notice that in the spirit of mimicking the behavior induced by the original circularly polarized pulse, two components have a $\pi/2$ phase shift.

Similar to the definition in Eq. (80), d represents the gap between the branches of the segmented spiral, while j_0 is the current density amplitude and is set to 7.57 $\times 10^{-7}$ A nm^{-2}. Four segments of the spiral are represented in four angular sections: from 0 to $\frac{\pi}{2}$, $\frac{\pi}{2}$ to π, π to $\frac{3}{2}\pi$ and $\frac{3}{2}\pi$ to 2π. Once again, a Gaussian

envelope is introduced in the temporal domain to ensure a short pulse. The width in time corresponds to $\tau = 4$ fs, while the shift in time is $t_0 = 13.3$ fs. In order to have a finite and smooth emission range, the spatial span of the current source is set to σ =0.08 μm.

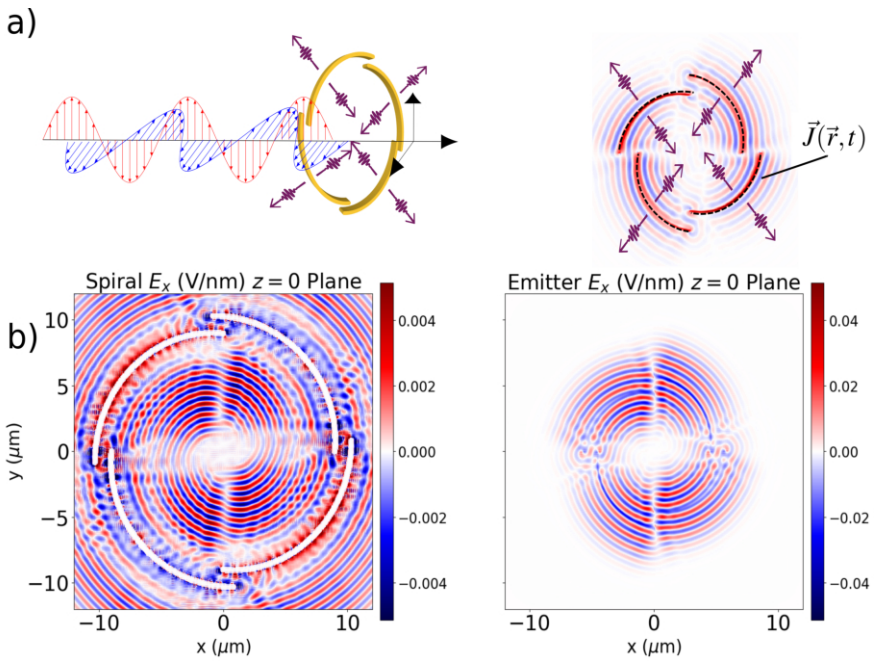

Figure 9: The induced field from the spiral as a Drude medium is found on the left side, while the emission from the current density described in Eq. (89) is situated on the right side. The panel (a) describes the schematics of the comparison: The emission from the gold nanoplasmonic spiral is replaced by the current emitters. Such emitters are prescribed directly in the simulation box and shown in dashed black lines. In panel (b), the emission cross sections are given. The simulation with the current emitter setup permits scaling down the simulation box: We set the radius of the emitter to 4.5 μm. The figure is reproduced with permission from E. I. Albar et al., *Sci. Rep.* **13**, 14748 (2023), licensed under CC BY 4.0.

In Fig. 9, we compare the two mechanisms of vortex generation: the plasmonic spiral and the spiral-shaped current emitters. For the emitter case (right panel), the spiral radius was chosen as $r_0 = 4.5$ μm, i.e., half the radius of the actual plasmonic spiral (left panel), to reduce computational cost. The current emitters are also much thinner, with their extent defined by the parameter σ, in contrast to the 1.6 μm span of the gold segmented spiral. These simplifications allow for a simulation box of $12 \times 12 \times 6$ μm, with a spacing of 80 nm, which accelerates the calculation remarkably. As we will see in the following section, the aim is to add classically described charged particles to the simulation box. In this context, the simplification that is entailed by current emitters provides an outstanding computational advantage. This setup allows the incorporation of other systems in the box while still allowing a reasonable computation time.

Nonetheless, even if sources are positioned differently relative to the origin, the resulting radiation patterns exhibit striking similarities, as seen in the lower panel of Fig. 9 and in Fig. 10. They share the same number of nodal lines, and the two interference profiles are almost identical. The validity of this replacement is confirmed over time, both in terms of the electric field amplitude and the OAM density.

The resemblance in OAM behavior is clearly visible in Fig. 10. Here, both the electric field E_x and OAM density components are sampled with intervals of 2.6 fs. The patterns are compatible in spatial distribution and dynamics. Moreover, the dynamics shown here also unravel the time-resolved emergence of phase structuring that leads to the OAM content in the pulse. In the time-resolved picture, we see that the phase introduced by segmented branches ends up causing the interference petals seen in OAM density dynamics. These patterns evolve in time to form the high-intensity donut rings visible in OAM beams. Another observation is that due to the positioning of branches, emanated fields cancel at the center, leading to an empty area in the center, which is the fingerprint of OAM beams.

However, a direct quantitative comparison of two emissions is not feasible. This is due to immense structural differences: While the plasmonic spiral has a finite and considerable thickness corresponding to two wavelengths of the incident beam, the current emitters are much thinner in the propagation direction, as explained above. Therefore, the amount of emission amplitude over time changes substantially. However, the phase structuring behavior is similar, as evidenced by the time-resolved pattern observed in OAM density given in Fig. 10. Therefore, to probe the local OAM density, adopting the current emitters is useful and accurate.

We note that even in the case of the idealized spiral-shaped emitters, which are free from the numerical artifacts associated with radiation at metal surfaces, the cross-sectional profiles do not immediately reproduce a structure that is identical to a pure Bessel beam, as previously reported in the frequency domain [72]. The root of this discrepancy is the broad frequency content of the ultrashort driving pulse, which introduces various spectral components. The components that are not tuned to the central frequency of the incident beam do not experience the same phase structuring via spiral branches, since they are mismatched to the gap between the spiral branches. This then forbids the formation of a clean nodal structure with the expected number of phase discontinuities. One can resort to a systematic study with progressively longer pulses until the continuous wave regime is covered. However, this is a computationally heavy study and beyond the scope of this work.

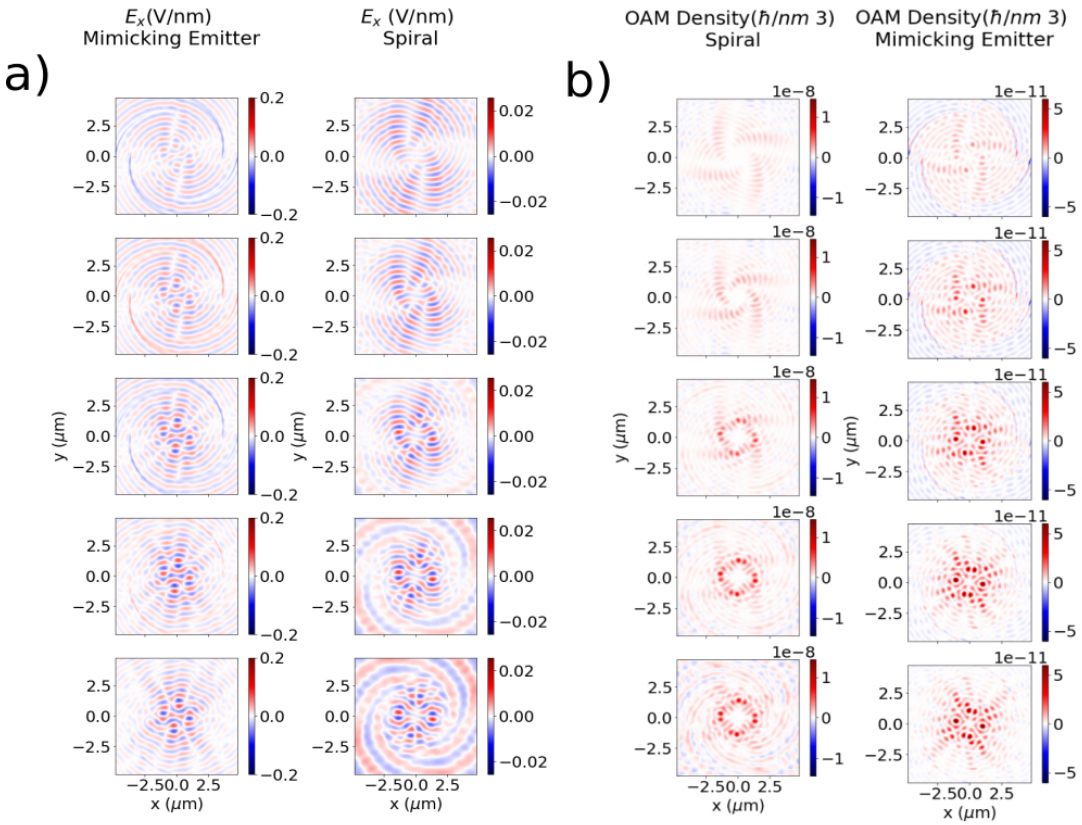

Figure 10: a)The induced electric field from the spiral as a Drude medium is on the left side, while the emission from the current density described in Eq. (89) is on the right. While the area close to boundaries displays different characteristics, the phase structuring is similar at the center, where emitted fields from the segments interfere. b) Same comparison for the OAM density. The left side is the Drude medium, while the right side shows the current emitter OAM density. Once again, particularly at the center where the structuring takes place, the interference patterns similar to petals are striking. The figures here are reproduced with permission from the supporting information of E. I. Albar et al., *Sci. Rep.* **13**, 14748 (2023), licensed under CC BY 4.0.

The motivation for devising the current emitters is to make simulations feasible in the presence of other systems. To probe the local OAM density, we introduce a point charged particle system in the following section. This will enable us to characterize the beam further and to develop a microscopic understanding of OAM transfer between light and matter.

5.3 Investigation of Local Orbital Angular Momentum Density using Point Charges

The dynamics of two point-like charged particles serve to probe the transfer of OAM with full space and time resolution. We employ the current emitter system described in the previous section and place a point-like particle system as the target of the OAM light pulse in the simulation box. The position of the point-like system is changed across the transversal plane of the emitter, and the resulting angular momentum change and trajectories are computed. The dependence of the angular momentum and trajectory of the cross-sectional location of the particle system provides insight into OAM transfer that takes place upon the interaction of the emitted electromagnetic field with matter.

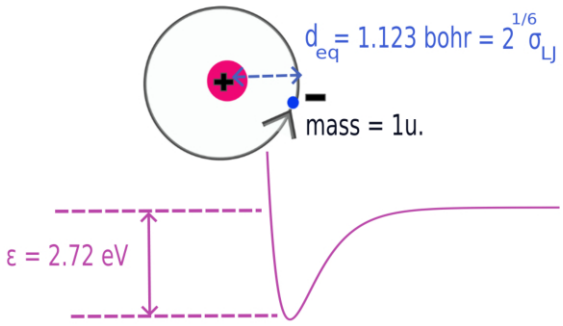

Figure 11: A Lennard-Jones potential is binding the two classically described charged particles. While the anchor particle is heavy and unaffected by the radiation, the orbiting charged particle is lighter and its trajectory is susceptible to incoming OAM content.

For the two particles, we choose to have opposite charges of ± 1 atomic units ($\pm 1.602 \times 10^{-19}$ C) so that overall charge neutrality is ensured. The two charged point-like particles are devised so that only one of them is affected by the emission. One of them is much lighter with a mass of 1 u ($1.67 \times 10^{-24} g$, 1836 m_e, 1 atomic mass unit). The other particle, named *'anchor particle'*, has a much heavier mass of ($9.1 \times 10^{-21} g$, 10^7 m_e). The asymmetry between the masses of the particles ensures that the system is not swept away by the radiation. Then the lighter mass, which orbits the heavy particle, responds to the field, and its angular momentum and trajectory become a direct indicator of OAM content in the radiation.

The two particles are bound with a Lennard-Jones potential, which favors a specific distance between them. The employed Lennard-Jones potential takes the

form

$$V_{\mathrm{LJ}} = 4\epsilon_{\mathrm{LJ}} \left[\left(\frac{\sigma_{\mathrm{LJ}}}{r} \right)^{12} - \left(\frac{\sigma_{\mathrm{LJ}}}{r} \right)^{6} \right]. \tag{91}$$

Here, σ_{LJ} parameter governs the distance that minimizes the potential, so that $r_{min} = 2^{1/6}\sigma_{\mathrm{LJ}}$. On the other hand, ϵ_{LJ} denotes the depth of the potential well experienced by the light particle. In our simulations, the potential depth is set to $\epsilon_{\mathrm{LJ}} = 2.72$ eV, while $\sigma_{\mathrm{LJ}} = 0.053$ nm, which results in an equilibrium distance of $d_{eq} = 1.123$ Bohr ($\approx$0.065 nm), which is close to the interatomic distance in an H_2 molecule.

In the following two cases are studied: a plane wave pulse and the OAM pulse from a current emitter. In the first case, a plane wave radiation is used. The second one, concerning the spiral emitter, probes the local OAM of the incident field. Both simulations have the same simulation setup: They consist of the addition of the point-like particles into the simulation box of the spiral emitter, while the plane wave is adjusted to have no phase structuring and has a uniform cross-section. This setup is an example of the *multisystem* framework of the Octopus code. Here, the emitted radiation is a system using a Maxwell solver box, where its partner system, namely classical point-like particles, is its own system. Here, the two-particle system is propagated using the exponential midpoint scheme [149]

The two-particle system interacts with the radiation via the Lorentz force,

$$\vec{F}(\vec{r}, t) = q(\vec{E}(\vec{r}, t) + \vec{v} \times \vec{B}(\vec{r}, t)), \tag{92}$$

where q is the charge of the particle and $\vec{v}$ its velocity. We compute the angular momentum change of the particle $\vec{L}_p$ induced by the incident radiation with

$$\vec{L}_p = m_p \left[(\vec{r} - \vec{r_0}) \times \vec{v} \right], \tag{93}$$

where m_p is the particle mass, and $\vec{r}_0$ and $\vec{r}$ are the initial and time-dependent positions.

The particle system is located at various positions across the xy plane of the spiral emitter, and then we probe the spatial dependence of angular momentum transfer and connect it to the corresponding local field characteristics. To achieve this, one needs to consider the OAM pattern in the cross-sectional (xy) plane. Since the goal is to capture the full-time resolution of OAM transfer, we form a Fourier-transformed map of the time-dependent local OAM density for the current emitter. The panel (a) of Fig. 12 shows the Fourier transformed map

$$\tilde{\vec{L}}(\vec{r}, \omega) = \int_{-\infty}^{+\infty} \vec{L}(\vec{r}, t) e^{i\omega t} dt. \tag{94}$$

Here, the Fourier component corresponding to 800 nm is chosen.

The resulting Fourier transformed OAM density map in Fig. 12 allows us to distinguish 'hot spots' within the concentric-ring structure generated by the spiral emission. To probe these regions, we place the particle system at the positions labeled 1–4 in Fig. 12 a). Here, the first point is at the center of the emission, while the second one is placed on the 'hot spot' which corresponds to a dense local OAM density. The third one is situated at the following ring, which is another hotspot, and the fourth point corresponds to a low local OAM density. The particle dynamics are then calculated for the external field of the spiral emitter (Fig. 9) and under excitation by a circularly polarized plane wave (Fig. 12 b). The plane-wave pulse is adjusted to match the scaled spiral emitter in amplitude and envelope, enabling a direct comparison. The resulting trajectories, shown in Fig. 12 c) after subtracting the initial positions, show the net displacement of the lighter particle. In both cases, the particle acquires angular momentum within a finite interaction window, comprising a circular orbiting motion and a subsequent return to its starting point. Whereas the trajectories driven by the plane wave remain circular and uniform, those induced by the spiral emitter exhibit noticeable deformations, which are consistent with previous reports [150]. This is expected since the cross-section of the plane wave is uniform, i.e., changing the particle location across the cross-section is not expected to result in a behavior change. Movies of the time-resolved trajectories of the particle system located in point 2 for both cases, spiral emitter and plane wave, can be found in [151].

The change of the point particle's angular momentum, ΔL_p, is presented for positions 1–4 in Fig. 12 d) and e). Here, the particle starts at rest with zero angular momentum, and ΔL_p refers to the difference in angular momentum upon the interaction with the radiation. As can be predicted from the trajectories of panel c), the circularly polarized plane-wave pulse imparts an identical change in angular momentum to the probe particle, independent of its initial location. In contrast, for the OAM-carrying pulse, the angular momentum transfer exhibits a significant spatial dependence. When analyzed in relation to the OAM density distribution shown in Fig. 12 a), we find that the density is maximal at point 2, consistent with the significant angular momentum change observed there. Surprisingly, however, point 1 shows an even larger angular momentum transfer than predicted, despite lying at the vortex center where the OAM density reaches a minimum. For points 3 and 4, the angular momentum change decreases progressively, in accordance with the OAM density trend. Thus, while the spiral emitter reproduces the expected spatial dependence at points 2–4, the anomaly at the vortex center reveals a limitation of the classical OAM density picture in predicting the actual particle response, as well as the limitation of single-frequency,

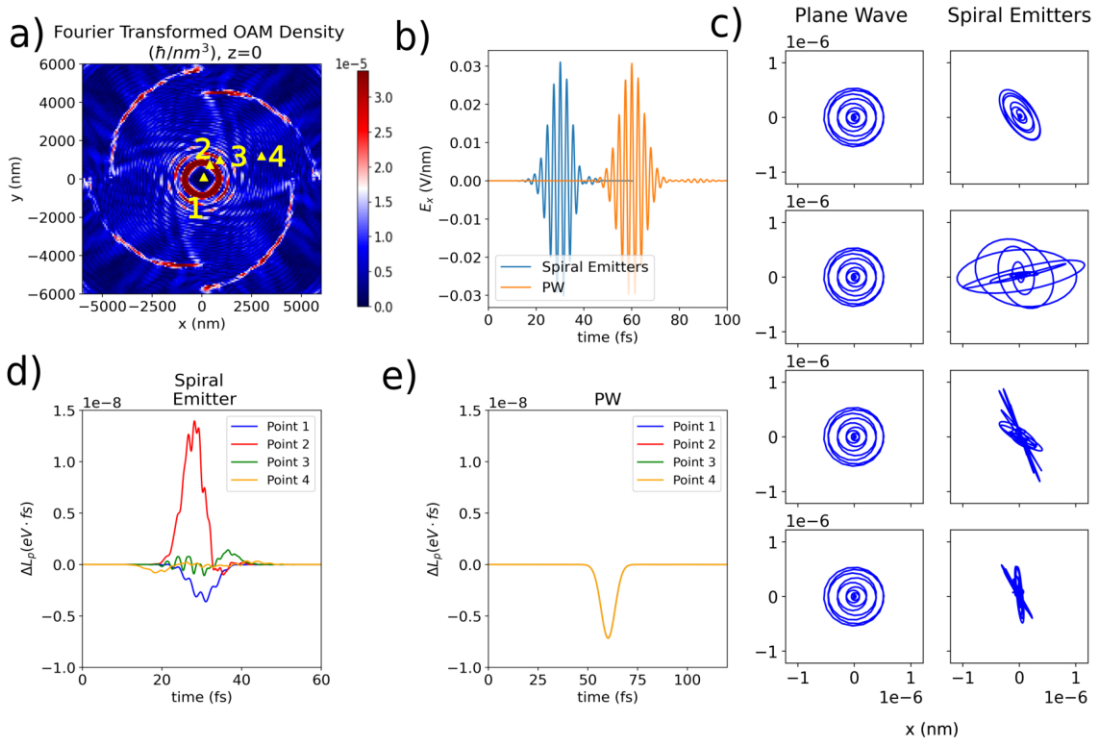

Figure 12: The local OAM of the light field from the spiral emitters is characterized by placing the point particles at different locations. (a) The Fourier component of the time-dependent orbital angular momentum density shown in Eq. (85) at the $z = 0$ plane, at the frequency of 1.55 eV, which corresponds to 800 nm central wavelength used for the spiral emitter. The yellow triangles mark the locations 1-4 of the probe particles. This cross-sectional plot shows the x and y coordinates of both particles; they overlap in the z direction. The lighter particle is at the $z = 0$ plane, and the heavier (anchor) particle resides in the $z = -d_{eq}$ plane. d_{eq} denotes the Lennard-Jones equilibrium distance between the particles. (b) The temporal behavior of the electric field E_x emitted by a spiral-shaped source and right circularly-polarized plane wave at the point (0,0,0) is presented. Both sources show the same amplitude and temporal behavior, except for a delayed arrival of the plane wave pulse at the location of the particle. Here, both the pulse emitted from the spiral emitter and the plane wave have a full width at half maximum (FWHM) of 0.3 eV. (c) The $x - y$ components of the trajectories of the lighter particle are shown when driven by a plane wave pulse (left column) and by the radiation generated by spiral emitters (right column). The labels 1-4 correspond to particle positions 1-4 in panel (a). (d) and (e) z component of the angular momentum change ΔL_p as described in Eq. (93) are given. At (d), results for particles at locations 1-4 from panel (a) in the presence of the vortex-like beam are given. (e) shows the results for the plane wave pulse. Here, the notation ΔL_p is used, since it refers to the difference in angular momentum introduced by radiation after the particle starts at rest with zero angular momentum. The figure is reproduced with permission from E. I. Albar et al., *Sci. Rep.* **13**, 14748 (2023), licensed under CC BY 4.0.

continuous wave analysis of OAM generation. The motion at the center is partly due to several frequency components of the pulse: While the components of 800

nm cancel due to the structuring of emitter branches with a gap of 800 nm, other components do not experience the same pattern. Therefore, they do not cancel exactly at the center and keep acting on the particle system. Moreover, a quantum understanding of the problem is also important: In the following chapters, we will see that even though the field has zero amplitude at the beam center, the electronic Hamiltonian will have quadrupolar and further interactions through gradients in the electromagnetic field, which will result in effects beyond the ones predicted by a classical Lorentz force coupling.

5.4 Discussion & Outlook

The microscopic mechanism of OAM generation in electromagnetic fields upon the interaction with matter is not completely understood. In this work, we have investigated this problem using nanoplasmonic Archimedean spirals within real-time, real-space simulations performed with the Octopus code. Firstly, a circularly polarized plane wave was directed onto plasmonic optical vortex generators, and the resulting twisted light formation was observed with complete spatio-temporal resolution. In agreement with earlier studies, we find that emission from the spiral branches shapes the phase of the incident beam and creates a vortex-like structure, and governs the OAM content of the outgoing electromagnetic field.

We employed the classical description of orbital angular momentum [135], and probed its emergence in the simulation box. We formed OAM density maps that confirmed the formation of a spatially and temporally structured vortex beam. However, the field exhibits modifications from previous theoretical works due to the finite time envelope of the incident pulse. This motivated us to investigate the local OAM density of the radiation further. To do so, we employed a simplified description in which the spiral geometry was mimicked by current emitters. For this description, we proposed an analytical expression for the current distribution capable of generating a similar twisted beam, establishing a link between the nanostructure geometry and the induced currents. This simplification reproduced the essential features of the vortex field and also enabled us to couple a classically described point-particle system to the emitted radiation and resolve the transfer of angular momentum in real time.

When probe particles are positioned at different locations across the beam cross-section, their trajectories and the associated angular momentum transfer show clear spatial variations, which is in contrast with a plane wave beam. This spatial dependence is inherent to structured beams, and challenges the well-established EDA. We will see in the following sections that the full minimal coupling approach can overcome this problem.

For most points where the particle system is located, the transferred angular momentum is well captured by the classical local OAM density. However, at the vortex center, a deviation emerges, precisely in the regime where the non-trivial effects of structured light carrying OAM are expected. This calls for further investigations to assess the validity and the limitations of a classical description of angular momentum for light in such cases, as well as the continuous wave approach.

To enable these multiscale studies, we have employed the Octopus code [116], which allows for the real-time propagation of Maxwell's equations on a real-space grid. Originally designed for quantum dynamics and light-driven phenomena, the code has been extended into a multi-system, multi-physics framework. Within this setting, electromagnetic fields can be coupled both to simplified semiclassical models of matter and, self-consistently, to first-principles electronic descriptions via time-dependent density functional theory (TDDFT) [125] [99]. In the present work, we restricted ourselves to classical susceptibility models to describe the plasmonic medium. However, a natural next step is to model the interaction of vortex beams with matter from first principles, by exploiting the coupling of TDDFT with Maxwell's equations in real time, retaining the complete spatial dependence of the electromagnetic fields through the minimal coupling Hamiltonian [125]. Within this approach, not only the fields emitted by plasmonic vortex generators, but also analytically defined vortex beams (e.g., Bessel beams) can be used to excite electronic systems. It will be detailed in the following chapters that such a methodology paves the way for novel insights that transcend the dipole approximation.

Another promising direction is to design OAM induced setups where additional symmetries are broken beyond the time-reversal symmetry already lifted by circular polarization [152]. We will explore such linear and nonlinear regimes which would open new opportunities for tailoring light–matter interactions in the following sections.

The datasets generated and analysed during the current study are accessible in this repository (DOI:10.5281/zenodo.8208674).

6 High Harmonic Generation Beyond Electric Dipole Approximation*

In this chapter, we employ the FMC framework tool from previous chapters to investigate high-harmonic generation driven by vortex beams beyond the EDA. Using the FMC formalism, we include all multipolar contributions without truncation and address the complete spatio-temporal structure of the incident optical vortex. We analyze beyond-dipole modifications in electron trajectories and in the corresponding harmonic spectra, where the orbital angular momentum of the beam gives rise to both magnetic and quadrupolar contributions. We confirm the existence of nonlinear dipole motion along both the polarization and propagation directions for the case of the plane-wave excitation. In contrast to the plane-wave case, vortex beams induce an additional nonlinear dipole response in the direction orthogonal to both the polarization and propagation axes. We show that the symmetry breaking stemming from beyond-dipole effects becomes particularly evident in the appearance of even harmonics.

Since the discovery of light with OAM, numerous theoretical and experimental investigations have focused on the interaction between twisted light and matter, be it excitation [11–20], ionization [25–32], or scattering [21–24]. The study of HHG) with twisted light has gained a particular momentum [84, 85, 153–162], as it offers a tabletop setup for producing OAM beams.

The first understanding of the HHG process was the three-step model [80]. The steps are simple: first, the electron is driven away from the parent atom; second, it moves in the laser field, and the third and final step comprises its

*Parts of the following chapter, including figures and text excerpts, are adapted from the author's previously published work: Albar, E.I., Kosheleva, V.P., Appel, H., Rubio,A. and Bonafé, F.P., High Harmonic Generation with Orbital Angular Momentum Beams: Beyond-dipole Corrections. Physical Review A 112, 063109 (2025), Published by the American Physical Society under the terms of the Creative Commons Attribution 4.0 International license.

recombination with the parent atom. The recombination of the final step causes the electron to emit high harmonics.

The typical electron motion range is much smaller than the wavelength of a driving laser, especially for optical lasers with intensities smaller than 5.0 V/nm. This entails the approximation that the spatial profile of the laser field in the second step is neglected. As we have seen in Sec. 4.5.3, this means that the EDA can be applied; consequently, the electron is assumed to be driven solely by a time-dependent electric field, neglecting the spatial dependence of the field. This approximation states that the dominant direction of the HHG emission is then governed by the incident field's amplitude and polarization direction. However, the theoretical frameworks that tackle the HHG process have evolved and refined the description of the relevant light–matter interactions. Various corrections to the three-step model, as well as to the EDA picture, were proposed [163]. Subsequent works have shown that the magnetic field interferes with the trajectories of high-speed electrons via the Lorentz force, resulting in a figure-eight electron motion which is well beyond the capability of EDA [55, 91–96]. Such an effect of the magnetic field leads to deviations of the trajectories in the propagation direction of the incident laser. Nevertheless, the effects of the spatial structuring of light on the electron motion in the transversal plane, as is the case in twisted light beams, are yet to be tackled.

The space-dependent intensity profile of the twisted light beams proves the usual EDA to be insufficient to describe the interaction between matter and OAM beams. This shortcoming of the EDA has been addressed both experimentally and theoretically [12, 16]. However, these studies resided in the linear regime, and the effect of OAM beams in the nonlinear regime necessitates further attention. HHG with OAM beams has been previously studied within the local dipole approximation [84, 88], however, this approach merely considers the local values of the incident field. Therefore, magnetic and higher-order terms remain unaddressed within their light-matter coupling treatment.

In this chapter, the coupling between light and matter beyond the dipole approximation is considered with our FMC approach. This enables us to account for the effects of both the field gradients and the magnetic field. We perform real-space and real-time numerical simulations to solve the quantum equation of motion for the electron of a hydrogen atom. We then locate the target atom at different positions with respect to the beam center and inspect the resulting HHG spectra. The symmetry breaking due to the field gradients and the magnetic field manifests in the appearance of even harmonics. We resolve the electron trajectories for plane-wave and OAM beams to identify the effect of orbital angular momentum. The trajectory of the driven electron is not confined to the

polarization or propagation axes only under the effect of OAM beams. We test the angular dependence of the emission of harmonics in the transversal plane, i.e. plane orthogonal to the laser propagation, where the off-axis (perpendicular to the laser polarization) emission shows significant beyond dipole corrections. Consequently, we propose that the off-axis even harmonics can be tuned by the OAM content of the incident beam.

This chapter is organized as follows: in Sec. 6.1 we present the formalism used in this work and provide the expressions for the spectroscopic quantities analyzed thereafter. In Sec. 6.3, we employ a linear beam with strictly one component and identify the effects of gradients that stem from the OAM content of the incident field. After demonstrating the effect of the gradients, we proceed to employ a realistic three-component beam in Sec. 6.6 and investigate the beyond dipole corrections to the HHG process for a case of Bessel beam. We compare the results to the case of HHG driven by a conventional plane wave pulse. We also address the influence of orbital angular momentum on the HHG process in Sec. 6.7. Finally, we expand our analysis to the benzene molecule and report beyond dipole corrections for the case of a circularly polarized plane wave beam in Sec. 6.8.

6.1 Method

In this work, we study the HHG spectrum of the hydrogen atom. We calculate the spectra from the real-time evolution of the system for the cases of different driving lasers. The dynamics are computed by numerically solving the time-dependent Schrödinger equation

$$i\hbar\partial_t\varphi(\vec{r},t) = \mathcal{H}(t)\varphi(\vec{r},t). \tag{95}$$

Here $\hbar$ is the reduced Planck constant and $\mathcal{H}(t)$ is the electronic Hamiltonian. We use the real-space real-time Octopus code [100], as described in the chapter 4. This code has previously been used for the computation of HHG spectra of molecules [164], liquids [165], and solids [166].

For the numerical simulations, a cylindrical simulation box with a radius of 1.32 nm and a length of 3.7 nm was used. The largest excursion is expected to take place in the polarization direction (x direction) of the incident beam; henceforth, the height of the cylinder is aligned with the x direction. The simulation box is surrounded by absorbing boundaries of thickness 0.52 nm with a complex absorbing potential. These boundary conditions prevent spurious effects arising from the reflection of the driven electron [118]. The nucleus of the atom stays fixed. The grid spacing is 0.016 nm and the timestep is adjusted as 0.0036 fs. We employ the approximated enforced time-reversal symmetry (AETRS) scheme

for the time evolution [167]. Our analysis expands beyond the commonly used multipolar expansion [168] and considers the FMC Hamiltonian without resorting to truncations , as shown in Sec. 4, Eq. (61), see [99]. To distinguish the beyond-dipole corrections, we also compare the EDA results with light-matter coupling in the velocity gauge, as shown in Sec. 4, Eq. (50).

6.2 Description of Vortex Pulses: Bessel beams

In the present work, we use Bessel beams to form vortex pulses. The spatial profile of the incident Bessel beam is on a micrometer scale, therefore it is much larger than the relevant scale of the electron dynamics, as shown in Fig. 14a. To address this, the simulation box is shifted in space to the location of interest along the transversal plane of the incident beam. Thus, only the spatial component of the beam overlapping with the electronic simulation box is incorporated into the electronic Hamiltonian.

Circularly polarized beams do not generate high-harmonic radiation with spherical systems. The phase difference between the components reduces the recombination rate dramatically. Hence, we construct the Bessel-beam counterpart of linearly polarized plane-wave beams as [29, 136, 137]

$$\vec{A}^{\mathrm{3C}}_{\mathrm{tw}}(\vec{r},t) = \frac{1}{\sqrt{2}}\left[\vec{A}^{\mathrm{tw}}_{m_{\gamma_1},\lambda=+1,\theta_k}(\vec{r},t) + \vec{A}^{\mathrm{tw}}_{m_{\gamma_2},\lambda=-1,\theta_k}(\vec{r},t)\right], \tag{96}$$

where $m_{\gamma_1} - m_{\gamma_2} = 2$, m_γ denotes the total angular momentum, $\lambda = \pm 1$ represents the helicity, $\theta_k = \arctan\left(\frac{\varkappa}{k_z}\right)$ is the opening angle with k_z and the longitudinal and transversal components of the wave vector $\vec{k}$ are $\varkappa = \sqrt{(\frac{\omega}{c})^2 - k_z^2}$, respectively. Here,

$$\vec{A}^{\mathrm{tw}}_{m_\gamma,\lambda,\theta_k}(\vec{r},t) = f(z)\left(A^{\mathrm{tw}}_{m_\gamma,\lambda,\theta_k,x}(\vec{r},t), A^{\mathrm{tw}}_{m_\gamma,\lambda,\theta_k,y}(\vec{r},t), A^{\mathrm{tw}}_{m_\gamma,\lambda,\theta_k,z}(\vec{r},t)\right)$$

is the vector potential in Coulomb gauge describing a Bessel beam propagating in the z direction,

$$\begin{aligned}
A^{\mathrm{tw}}_{m_\gamma,\lambda,\theta_k,x} &= \frac{A_{\mathrm{tw}}}{\sqrt{2}}\Big[\cos(k_z z + \phi(m_\gamma+1) - \omega_b t + \Phi_{\mathrm{tw}}) d^1_{-1\lambda}(\theta_k)\, J_{m_\gamma+1}(\varkappa r_\perp) \\
&\quad + \cos(k_z z + \phi(m_\gamma-1) - \omega_b t + \Phi_{\mathrm{tw}}) d^1_{1\lambda}(\theta_k)\, J_{m_\gamma-1}(\varkappa r_\perp)\Big], \\
A^{\mathrm{tw}}_{m_\gamma,\lambda,\theta_k,y} &= \frac{A_{\mathrm{tw}}}{\sqrt{2}}\Big[\sin(k_z z + \phi(m_\gamma+1) - \omega_b t + \Phi_{\mathrm{tw}}) d^1_{-1\lambda}(\theta_k)\, J_{m_\gamma+1}(\varkappa r_\perp) \\
&\quad - \sin(k_z z + \phi(m_\gamma-1) - \omega_b t + \Phi_{\mathrm{tw}}) d^1_{1\lambda}(\theta_k)\, J_{m_\gamma-1}(\varkappa r_\perp)\Big], \\
A^{\mathrm{tw}}_{m_\gamma,\lambda,\theta_k,z} &= A_{\mathrm{tw}} \sin(k_z z + m_\gamma\phi - \omega_b t + \Phi_{\mathrm{tw}}) d^1_{0\lambda}(\theta_k)\, J_{m_\gamma}(\varkappa r_\perp),
\end{aligned} \tag{97}$$

where Φ_{tw} is a constant phase, A_0 is the peak amplitude, and ω_b is the central frequency of the pulse, respectively. $J_m(\varkappa r_\perp)$ represents the Bessel function, $r_\perp = \sqrt{x^2+y^2}$, $\phi = \arctan(y/x)$ is the azimuthal angle, and $d^1_{\mu\lambda}(\theta_k)$ denotes the small Wigner matrix.

The real-space envelope function along the propagation direction (z axis), is given by

$$f(z) = \sin^2\left(\frac{\pi(z-R_0)}{w}\right)\theta(z-R_1)\theta(R_0-z), \tag{98}$$

where $z = ct$, $\theta(z)$ is the Heaviside step function, R_0 and R_1 define the spatial extent of the envelope in real space, $w = 8\lambda_w$ with $\lambda_w = 800$ nm being the central wavelength of the laser field. This choice ensures that the pulse contains 8 optical cycles, corresponding to a duration of 21.3 fs.

We illustrate the evolution of the incident electromagnetic pulse used in the calculations. We express the pulse as a function of position as $f(z)$ as seen in Eq. (98), where the time dependence is carried with the compound variable $z = ct$. With our illustration, we aim to demonstrate the correspondence between the space and time dependence of the short pulse, as detailed in Sec. 4.8. As it can be seen in Fig. 13, the pulse is restricted within $z = R_0$ and $z = R_1$. As the calculation progresses in time, the position dependence $f(z)$ of the pulse carries the envelope forward in the simulation box. Each frame in the figure corresponds to another timestep, showcasing the time evolution of the electromagnetic pulse.

We use the *External Source* feature of the Octopus code to evaluate the spatiotemporal shape of the Bessel beam. However, we would like to note that the envelope is only applied in the propagation direction z; therefore, this operation does not convert the field to well-known Bessel-Gauss type beams with finite transverse extent, which are typically used in experiments. Since in the present study a single atom is affected only by the local spatial profile of the beam, an ideal Bessel beam is sufficient to describe the spatial profile in the vicinity of the atom.

The polarization of $\vec{A}^{\text{3C}}_{\text{tw}}(\vec{r},t)$ has 3 components in general (which are specified by index 3C). This twisted-light field $\vec{A}^{\text{3C}}_{\text{tw}}(\vec{r},t)$ can be viewed as the realistic analogue of linearly polarized light, since in the paraxial limit (when the opening angle approaches zero, $\theta_k \to 0$) it reduces to a single transverse component along the x axis,

$$\vec{A}^{\text{1C}}_{\text{tw}}(\vec{r},t) \approx A_{\text{tw}} f(z) J_m(\varkappa r_\perp)\cos(k_z z + m\phi - \omega_b t + \Phi_{\text{tw}})\hat{e}_x. \tag{99}$$

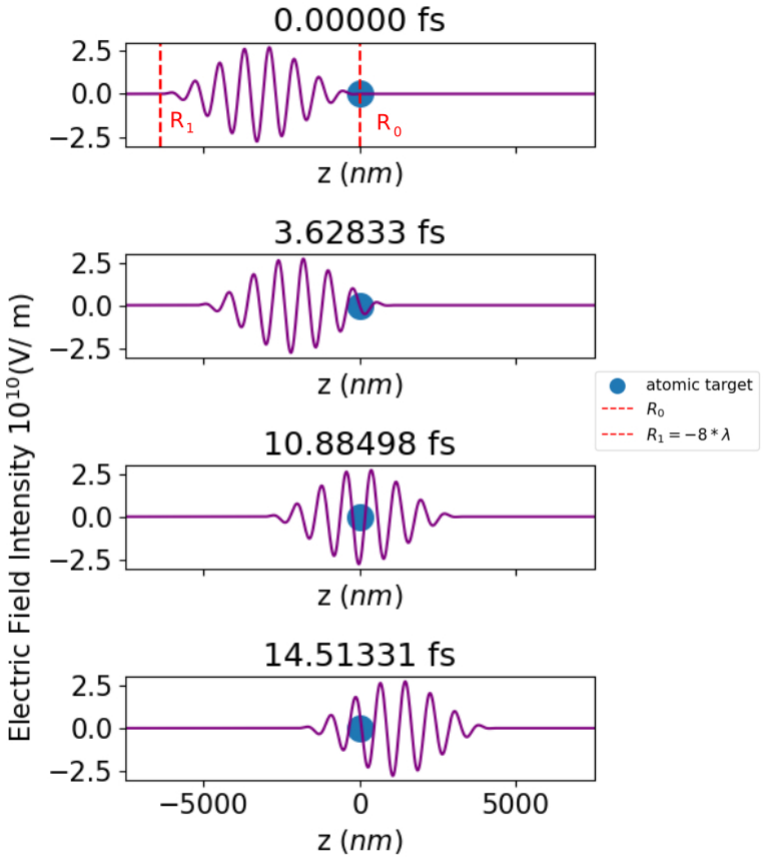

Figure 13: The time evolution of the pulse, expressed in position space. Applying the envelope in the space implies imposing it also in time: R_0 and R_1 mark the initial spatial extent of the pulse. As the pulse evolves in time, it also evolves in space owing to the compound variable $z - ct$. The position of the target is shown with blue markers. The figure is reproduced with permission from the supplemental material of E. I. Albar et al., *Phys. Rev. A* **112**, 063109 (2025), published by the American Physical Society under the terms of the Creative Commons Attribution 4.0 International license.

Here the unit vector is given by $\hat{e}_x = (1, 0, 0)$ and we note that in the paraxial approximation $m_{\gamma_1} \approx m + \lambda = m + 1$ and $m_{\gamma_2} \approx m + \lambda = m - 1$, where m is the projection of OAM. The vector potential $\vec{A}^{1C}_{\text{tw}}(\vec{r}, t)$ only approximately obeys the Coulomb gauge [169]. In Section 6.6 we examine how the observables are strongly affected by the choice between $\vec{A}^{1C}_{\text{tw}}(\vec{r}, t)$ and $\vec{A}^{3C}_{\text{tw}}(\vec{r}, t)$. Therefore, to account for all 3 components of the vector potential is of crucial importance.

To investigate the effects stemming from OAM, we compare the OAM results

with their plane wave counterpart, which does not have OAM content. The expression of the plane wave pulse with explicit space dependence is

$$\vec{A}_{\mathrm{pw}}(\vec{r},t) = A_{\mathrm{pw}} f(z)\cos(k_z z - \omega_b t)\hat{e}_x. \tag{100}$$

The plane wave pulse is adjusted to have the same field amplitude, phase, wavelength (800 nm), and envelope as the $m = 1$ Bessel beam at the position $\vec{r} = (r_\perp, 45°, 0)$ with $r_\perp = 2545$ nm. The matching peak electric field amplitude $E_{\mathrm{pw}} = \omega_b A_{\mathrm{pw}}$ is 2.72×10^{10} V/m. For an accurate comparison of the two cases, this condition will be used throughout the chapter.

The HHG yield is computed from the dipolar emission P^d, i.e. the energy dissipated per unit frequency [170, 171],

$$P^d = \sum_{i=x,y,z} P_i^d = \frac{\mu_0 \omega^4}{12\pi c} \sum_{i=x,y,z} \tilde{d}_i{}^2(\omega), \tag{101}$$

as well as quadrupolar contribution P^Q [170, 171]

$$P^Q = \sum_{i,j=x,y,z} P_{ij}^Q = \frac{\mu_0 \omega^6}{1440\pi c^3} \sum_{i,j=x,y,z} \tilde{Q}_{ij}^2(\omega). \tag{102}$$

The expression for the magnetic dipole (MD) moment P^m contribution is

$$P^m = \frac{\mu_0 \omega^4}{12\pi c^3} \sum_{i=x,y,z} \tilde{m}_i^2(\omega). \tag{103}$$

Here, μ_0 denotes the magnetic vacuum permeability, while $\tilde{d}_i(\omega)$ is the Fourier transformation of ith component of the time-dependent dipole response $d_i(t)$,

$$d_i(t) = |e|\langle\varphi(\vec{r},t)|r_i|\varphi(\vec{r},t)\rangle, \tag{104}$$

and $\tilde{Q}_{ij}(\omega)$ represents the Fourier transform of the time-dependent quadrupole moments $Q_{ij}(t)$ corresponding to directions i and j.

$$Q_{ij}(t) = |e|\langle\varphi(\vec{r},t)|\left(3r_i r_j - r^2\delta_{ij}\right)|\varphi(\vec{r},t)\rangle. \tag{105}$$

Here δ_{ij} is the Kronecker delta.

6.3 HHG of a Hydrogen Atom: Isolating the Effect of Orbital Angular Momentum

The spatial structuring of OAM beams renders the HHG yield dependent on the location of the target relative to the center of the beam. We first tackle this position dependence for the case of the $m = 1$ Bessel beam $\vec{A}^{\mathrm{1C}}_{\mathrm{tw}}$. For the remainder of the chapter, we omit the dependence of the vector potential on $\vec{r}$ and t for brevity. We select three positions to place the atom along the line $\vec{r}_0 = (r_0, 45°, 0)$: The beam center ($r_0 = 0$ nm), first ring (We name this position *hot spot* due to large intensity of the field, $r_0 = 2545$ nm), and the third ring ($r_0 = 12020$ nm), as shown in panel a) of Fig. 14. The path connecting these points was selected so that the beyond-dipole effects in x and y directions receive averaged contributions of the field gradients.

We calculated the harmonic spectra from the electric dipole P^d and electric quadrupole P^Q terms for three selected positions. While we have also calculated the magnetic dipole emission P_m, which can be found in Fig. 15, we present it in a separate figure to highlight its disparity with other contributions. Note that we also adjust the vector potential phase to be the same for all three positions, to avoid spurious effects arising from the phase shifts. Fig. 15 shows the results calculated with this expression.

The panel b) of Fig. 14 shows that the electric field of the beam $\vec{A}^{\mathrm{1C}}_{\mathrm{tw}}$ is zero in the beam center, while the field gradient reaches its maximum. The larger gradients compared to the intensity lead to a quadrupolar P^Q emission that is comparable to the dipolar P^d counterpart, as shown in panel c) of Fig. 14. Since the spectra are computed within the FMC approach, the nonzero dipole emission for the beam center stems from the higher order terms in the full minimal coupling interaction Hamiltonian $\mathcal{H}^{\mathrm{f.m.c.}}_{\mathrm{int}}(t)$ (Eq. (61)). Nevertheless, the yield at the beam center is weak and displays a low cut-off due to the absence of field amplitude. In contrast, the HHG yield for the atom located at the hot spot in the first ring is stronger. The cut-off at this position reaches the 20th peak, in line with the classical three-step model trajectory prediction for the peak amplitude of the electric field, even though the peaks subside after the 15th harmonic. The dipolar emission follows the well-known selection rules and peaks at odd harmonics, while the quadrupolar emission displays peaks of even harmonics due to symmetry breaking, as reported previously [171]. Finally, at the position located at the third intensity ring ($r_0 = 12020$ nm), the Bessel beam has a small amplitude in comparison to the hot spot and almost zero gradients (as shown in Fig. 14 panel b). A weaker field amplitude leads to an earlier cut-off as expected, which is found at the 11th harmonic, accompanied by weaker peaks.

Both for the second and third studied positions, even though the effects of the field gradient are minimal, the magnetic field produces a symmetry-breaking that leads to a quadrupolar yield at even harmonics. Quadrupolar emission persists with higher harmonics owing to its ω^6 dependence described in Eq (102), and it reaches considerable yields at the hot spot thanks to the larger cut-off at the location. The quadrupolar emission, which is fully addressed only within beyond-dipole treatment, will become even more prominent at higher intensities, which will entail even higher harmonics. This analysis confirms the necessity of going beyond the EDA as the intensity increases [83].

The hot spot combines the strongest field amplitude with a nonzero field gradient, as shown in Fig. 14 panels b) and c). This entails a strong dipolar and non-negligible quadrupolar spectrum. Henceforth, we select this position of the atom for the remainder of the chapter.

6.4 Disentangling the Beyond-dipole Effects in Structured Beams

We now compare the spectra resulting from this point using a Bessel beam $\vec{A}^{\mathrm{1C}}_{\mathrm{tw}}$ with a plane wave to discern the OAM influence. Fig. 17 shows the frequency-resolved dipole component spectra (P^d_x, P^d_y, and P^d_z) produced by the plane wave $\vec{A}_{\mathrm{pw}}$ and Bessel beam $\vec{A}^{\mathrm{1C}}_{\mathrm{tw}}$, in its first and second column. The Bessel beam and plane wave spectra are indistinguishable when the coupling Hamiltonian is restricted within EDA. This limitation is born from the discarding of the spatial dependence of the OAM beam, which is imprinted on the trajectory of the driven electron. To overcome such a limitation, the beyond-dipole treatment of FMC is necessary, as seen in Fig. 17. The dipolar spectra shown in this figure demonstrate that while the Bessel beam can access all dipole components, the plane wave only drives the dipole in the x and z directions. The excited dipole component in the z direction, namely the propagation direction for both beams, is a clear outcome of the beyond-dipole coupling, as it has been shown previously by computing the Lorentz force in the propagation direction, which is proportional to the $\nabla_z A_{\mathrm{tw/pw}}$ [55, 93]. Unlike the P^d_x spectrum, which is governed by the dipole interactions, the spectral components P^d_z and P^d_y, arising from beyond-dipole corrections, both exhibit larger amplitudes at the even harmonics. The Bessel beam spectra have contributions from components other than the beam polarization (x) direction. This points to the need for a beyond dipole approach to analyze the spectrum, as well as the underlying dynamics.

We name the y and z contributions to the spectra *off-axis* contributions. We show their dipole moment dynamics $d_i(t)$, excited by the linear Bessel beams $\vec{A}^{\mathrm{1C}}_{\mathrm{tw}}$,

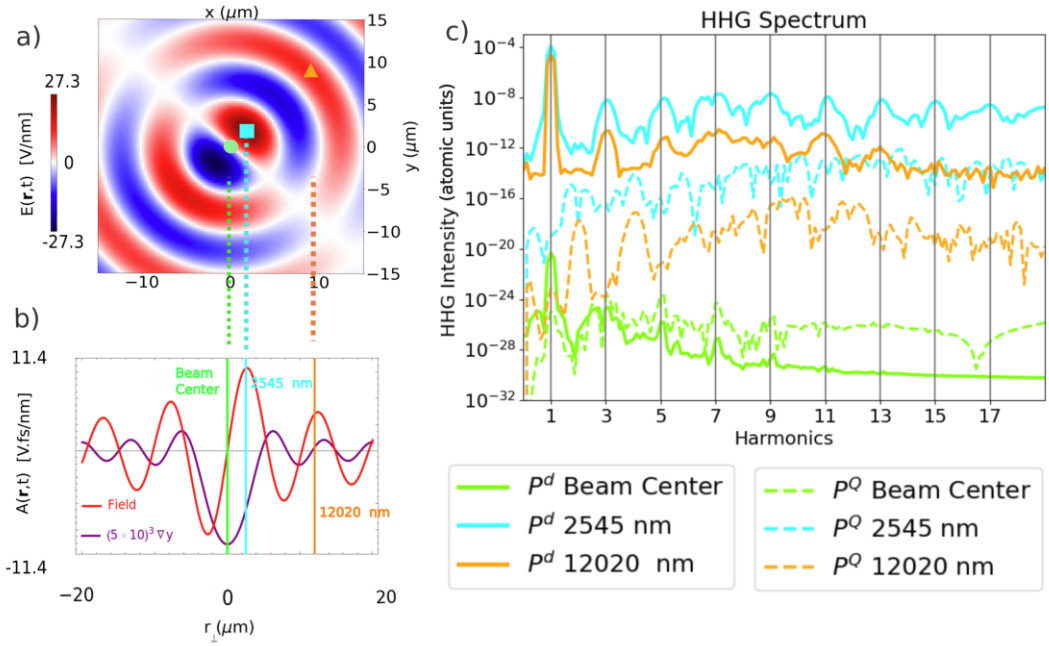

Figure 14: HHG spectra from three locations across the transversal plane. a) We depict the electric field $E_{\text{tw}}(\vec{r},t) = -\frac{\partial A^{1C}_{\text{tw}}(\vec{r},t)}{\partial t}$ of the Bessel beam. The one-component Bessel beam A^{1C}_{tw} with OAM number $m = 1$ has a singularity at the beam center due to the cancellation of the fields, marked in green. A hydrogen atom is first located in this position, where the driving electric and magnetic fields are absent. In contrast, the maximum of the field gradient occurs here, as shown in panel b), where the amplitude A^{1C}_{tw} and the spatial gradient in terms of y position of the corresponding vector potential A^{1C}_{tw} are plotted as a function of $r_\perp$. The next location is the hot spot at the first ring of the Bessel beam ($r_0 = 2545$ nm, marked by cyan color, with the highest field amplitude and non-zero gradient). The final point is at the third ring ($r_0 = 12020$ nm, shown in orange); the field amplitude is still considerable, and the gradient is zero. c) The HHG spectra in FMC from all three locations. Solid lines depict the dipolar emission spectrum P^d (See Eq. (101)), while dashed lines point to the quadrupolar P^Q (See Eq. (102)) counterpart. The results are computed beyond the dipole approximation. Throughout the chapter, the yields below $\approx 10^{-35}$ are considered numerically zero. The figure is reproduced with permission from E. I. Albar et al., *Phys. Rev. A* **112**, 063109 (2025), published by the American Physical Society under the terms of the Creative Commons Attribution 4.0 International license.

in Fig. 16. Since the dipole moment $d_i(t)$ described in Eq. (104) is the expectation value of the position of the electron in the Cartesian direction i, it is referred to as the trajectory. An animation of the trajectory shown in Fig. 16 can be accessed at Ref. [172]. The off-axis spectral signals are connected to the electron's trajectory: as the electron is driven further away from the ion, it accelerates, reaching a higher velocity. This leads to a greater Lorentz force acting on the electron, which then

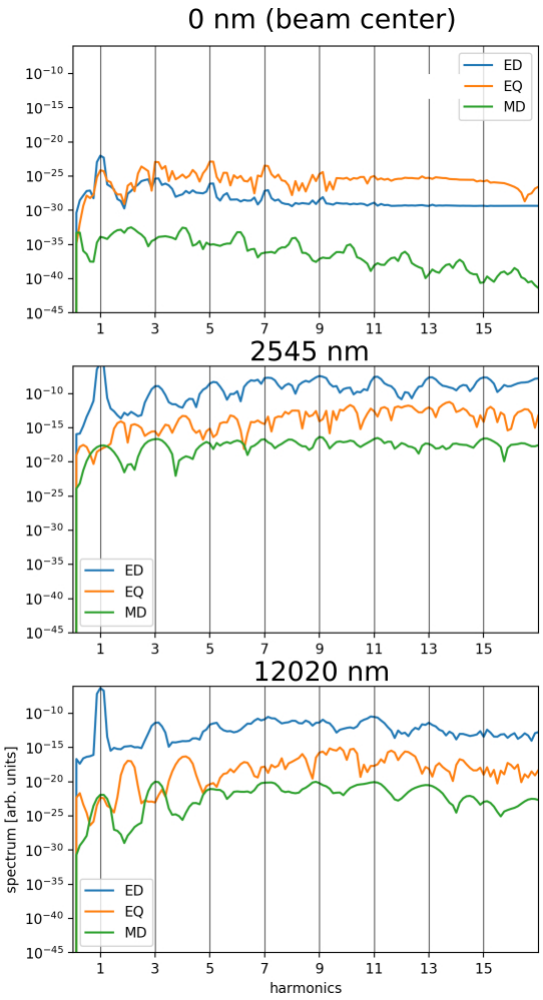

Figure 15: Magnetic dipole (MD) P^m contributions to spectra compared to those of electric dipole (ED) and electric quadrupole (EQ). Results are presented at three locations of the target system: At the beam center (0 nm), at a radial distance of 2545 nm (hot spot), and 12020 nm away from the beam center. $A_{\mathrm{tw}}^{1\mathrm{C}}$ beam is used for calculations. P^m is observed to be the weakest contribution to the spectra. The figure is reproduced with permission from the supplemental material of E. I. Albar et al., *Phys. Rev. A* **112**, 063109 (2025), published by the American Physical Society under the terms of the Creative Commons Attribution 4.0 International license.

deviates the electron from a linear path constrained to the polarization axis of the incident beam [91]. Accounting for only the electric field amplitude (dipolar coupling) when calculating the electron's trajectory cannot capture this behavior [173, 174].

The amplitudes of the electric and magnetic field amplitudes, the field gradients in the direction of propagation in the vicinity of the atom, of both the linear Bessel beam $\vec{A}_{\mathrm{tw}}^{1\mathrm{C}}$ and plane wave pulse are equal as shown in Fig. 17. This naturally leads to the contribution in the z axis, which stems from the longitudinal field gradients being identical. However, adding to the said magnetic-field-

induced figure-eight motion in the xz plane, the Bessel beam leads to a nonzero electron trajectory in all directions due to the xy-plane field gradients (see Fig. 23). These beyond-dipole trajectory components influence the angular distribution of the emission as shown in Fig. 24. The nonzero dynamics of the d_y dipole component can be attributed to the field gradients $\nabla_y A_{tw/pw}$, which are inherent to the structured beams. Therefore, measuring the P_y component of the emission could provide information about the transverse gradients, and vice versa. See Eq. (108) for an analytical expression of the field gradients of the Bessel beams.

However, we note that the results in Fig. 17 demonstrate that the effects of transverse gradients (P_y) are much smaller than the ones from longitudinal gradients P_z, particularly for the $\vec{A}^{\mathrm{1C}}_{\mathrm{tw}}$ case. This is established for paraxial beams, and further confirmed by the comparison given in Fig. 20. Regardless, investigating the angular distribution of the emission could help discern the effects on these two directions, as we will see in the following sections.

In Fig. 16, we depict the trajectory induced by the Bessel beam. In the upper part, blue lines point to FMC dipole moment dynamics, while red lines depict those in the EDA. The latter shows a one-directional oscillation along the polarization direction. Meanwhile, the FMC shows the excitation of both y and z dipole components. Deviations due to the magnetic field are already visible and equal for both beams as shown in the lower panels of Fig. 16.

6.5 Accounting for the Complete Structure of the Beams

The results we have presented up until this point have been computed with the approximated expression (99) for the vector potential $A^{\mathrm{1C}}_{\mathrm{tw}}$ that discards the y and z components, to isolate and identify gradient-driven motion. While the discarded components are small, especially considering the small opening angle used here, their effect persists [12, 16, 168, 175]. Therefore, as Ref. [12] experimentally and Ref. [16] theoretically demonstrated, to ignore the longitudinal field fails drastically, especially in the case of counterrotating spin and orbital angular momentum, even for paraxial beams. To unravel the effects of these usually disregarded components, we compare the frequency-resolved dipole component spectra for the cases of $A^{\mathrm{1C}}_{\mathrm{tw}}$ and $\vec{A}^{\mathrm{3C}}_{\mathrm{tw}}$, see Fig. 17, second and third columns. Considering the dipolar contribution P^d_x (which is the dominant contribution to the total dipolar emission P^d), both beam configurations $\vec{A}^{\mathrm{3C}}_{\mathrm{tw}}$ and $\vec{A}^{\mathrm{1C}}_{\mathrm{tw}}$ result in the spectra.

It is worth noting that both P^d_y and P^d_z emission spectra in the case of $\vec{A}^{\mathrm{1C}}_{\mathrm{tw}}$ driving beam lack the first harmonic (the largest contribution). This stems from the fact that the x polarized field is unable to efficiently excite dipoles in respective

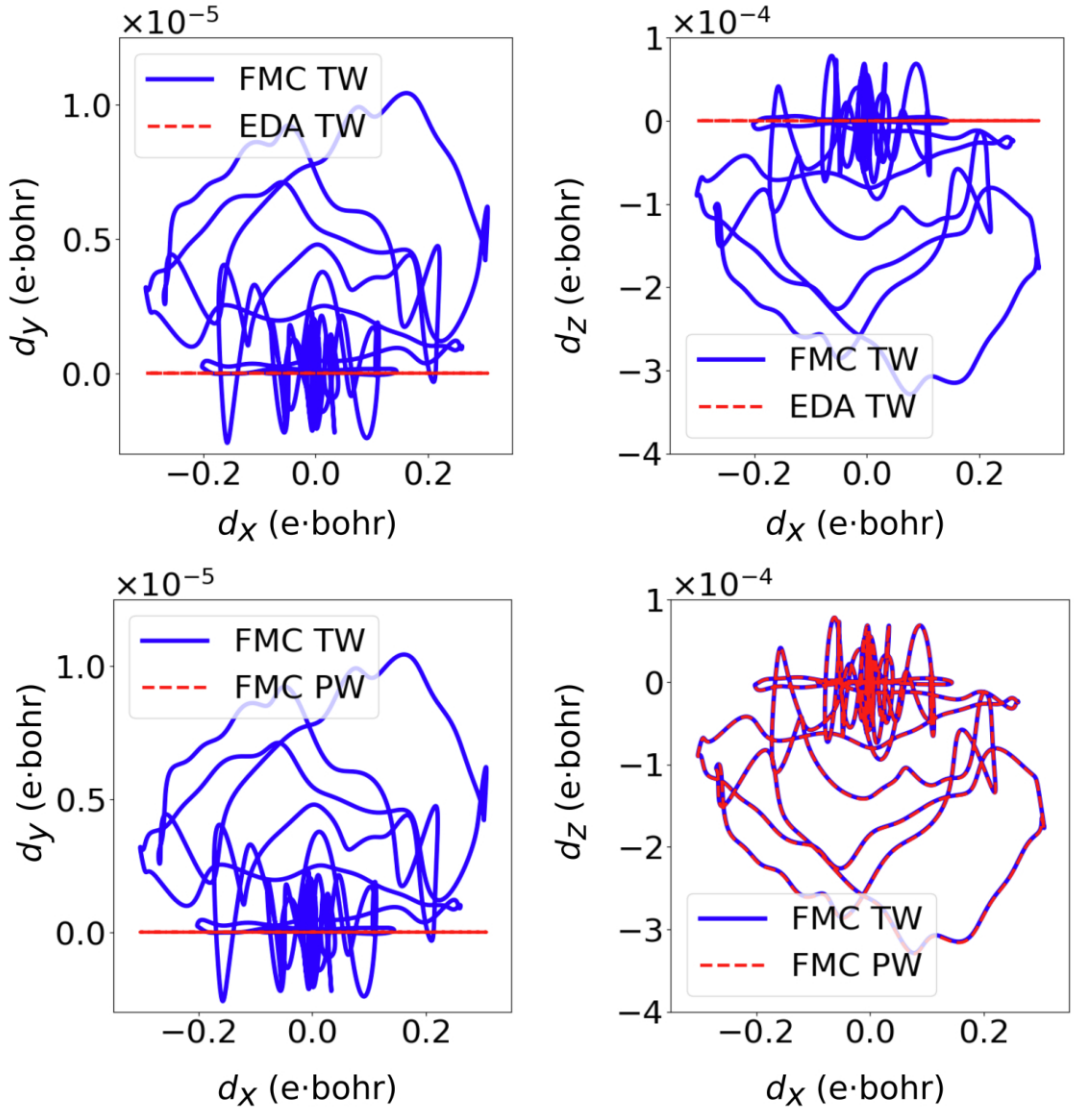

Figure 16: Comparison of dipole moment $d_i(t)$ dynamics with one component Bessel Beam OAM $\vec{A}^{1C}_{tw}$ and plane wave using EDA and FMC approaches. We show the dynamics from the Bessel beam in FMC (TW, blue) and velocity-gauge dipole (EDA TW, red) approaches in the upper panels. The dipole coupling is insufficient to capture off-axis deviations. Plane wave-induced off-axis motion and OAM beam-induced motion are plotted in the lower panels. The lower right panel shows that the plane wave also has a beyond dipole correction on the electron's trajectory.The figure is reproduced with permission from the supplemental material of E. I. Albar et al., *Phys. Rev. A* **112**, 063109 (2025), published by the American Physical Society under the terms of the Creative Commons Attribution 4.0 International license.

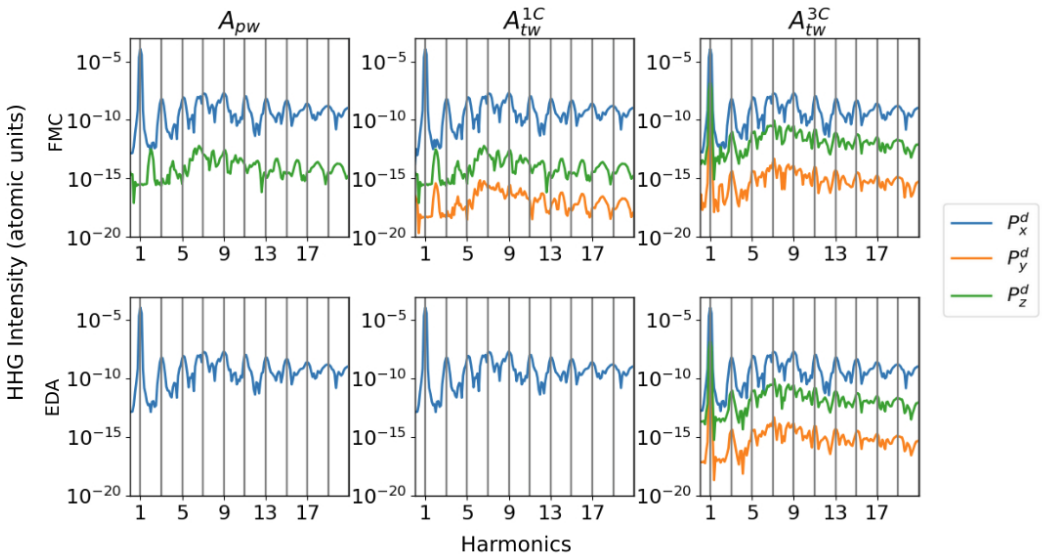

Figure 17: Dipole component resolved spectra for a plane wave beam and the Bessel beam. The target atom is located at the hot spot ($r_0 = 2545$ nm). At this point, the field amplitude, frequency, phase, and envelope of the x component of the Bessel beam with all three components ($\vec{A}_{\rm tw}^{3C}$, the Bessel beam with one component $\vec{A}_{\rm tw}^{1C}$) and plane wave match. The upper panel shows the dipolar emission in all three directions calculated with FMC, while the lower panel depicts the emission calculated within EDA. The figure is reproduced with permission from E. I. Albar et al., *Phys. Rev. A* **112**, 063109 (2025), published by the American Physical Society under the terms of the Creative Commons Attribution 4.0 International license.

directions alone.

We proceed to present FMC spectra of the Bessel beams in comparison with a plane wave without OAM content in Fig. 18. In such a case, y and z components of $\vec{A}_{\rm tw}^{3C}(\vec{r},t)$ have a nonzero magnitude: all three directions are excited, therefore all of the dipolar contributions are accessed with $\vec{A}_{\rm tw}^{3C}(\vec{r},t)$. The spatial structure of the Bessel beam provides access to all quadrupolar components; on the other hand, the plane wave lacks the cross components $\tilde{Q}_{yz}(\omega)$ and $\tilde{Q}_{xy}(\omega)$, due to the absence of field gradients in the y direction. These calculations are performed within the FMC approach.

The Bessel beam described by $\vec{A}_{\rm tw}^{\rm 3C}$ is more realistic and provides insight into dipole-level and beyond-dipole effects on all components of the emission. Since we have accomplished the mission of discerning and demonstrating gradient-driven motion in Sec. 6.3 free of dipolar contributions, now we switch to the realistic

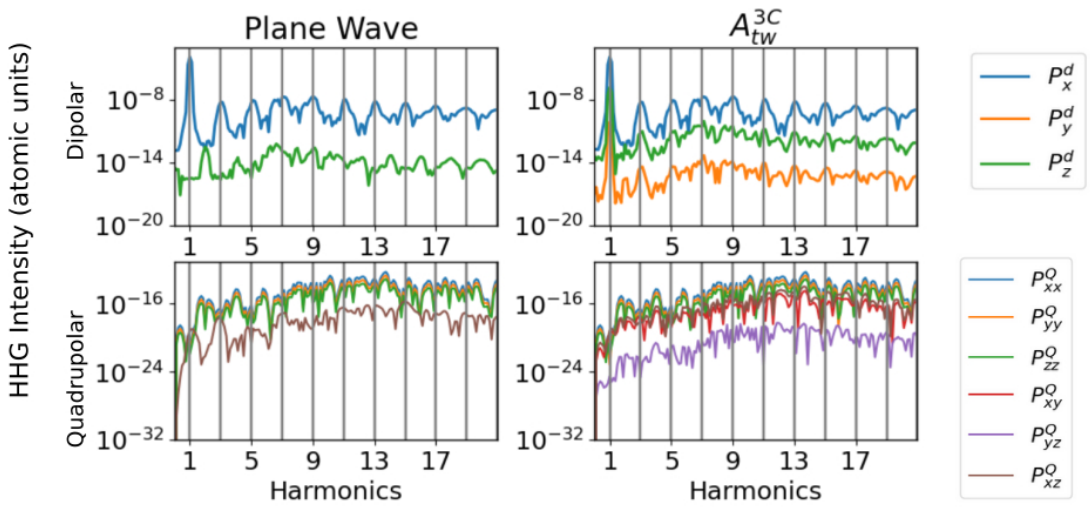

Figure 18: Component resolved spectra comparison for a plane wave and for a $\vec{A}_{\mathrm{tw}}^{3C}(\vec{r},t)$ Bessel beam. Without the paraxial approximation, the $\vec{A}_{\mathrm{tw}}^{3C}(\vec{r},t)$ beam preserves non-zero y and z components which drive oscillations in these directions, causing a contribution in these components of the spectra. In contrast to a Plane Wave, all dipolar and quadrupolar directions are excited. These calculations are within the FMC approach. The figure is reproduced with permission from the supplemental material of E. I. Albar et al., *Phys. Rev. A* **112**, 063109 (2025), published by the American Physical Society under the terms of the Creative Commons Attribution 4.0 International license.

beams. We will use $\vec{A}_{\mathrm{tw}}^{3C}$ for the remainder of this chapter.

6.6 Angular Beyond-dipole Corrections in HHG with Bessel beams

In this section, we focus on the beyond-dipole corrections caused by the structured fields. We show the results for the $\vec{A}_{\mathrm{tw}}^{3C}$ Bessel beam (TW) and the plane wave cases (PW) in Figure 19a. Here, we plot the normalized difference between the total HHG FMC spectra in comparison to their EDA counterpart, given in Fig. 17. The beyond dipole correction is plotted as a percentage. We observe that the beyond-dipole correction is around 100% for both cases in the second harmonic. This common correction has its roots in the magnetic field component in the y direction. The magnetic field in y direction acts on the electron trajectory with the Lorentz force in z direction. This results in a drift in the propagation direction for both PW and TW beams, since this effect, namely radiation pressure, is free of OAM. For the greater even harmonics (6th, 8th, 10th, and 12th), the correction in the TW case lies between 2% and 10%, which is much larger than the PW correction. Keeping in mind that the corrections stemming from the gradients in the z direction are identical for both beams, such deviations between the two

cases for greater even harmonics can be associated with the gradients in the xy plane. In other words, the spatial structure of the Bessel beam causes a beyond dipole correction that survives in even harmonics.

A relevant observable related to the HHG process is the emission in the far field. We analyze the beyond-dipole corrections to the angular distribution of the resulting emission, $P^d(\omega,\theta)$. The definition is $P^d(\omega) = \int d\Omega P^d(\omega,\theta)$ where $d\Omega = \sin\theta d\theta d\varphi$ is the solid angle, and $P^d(\omega,\theta)$ is computed as

$$P^d(\omega,\theta) = \frac{\mu_0 |\tilde{\vec{d}}(\omega)|^2 \omega^4}{32\pi^2 c} \sin^2\theta. \tag{106}$$

Here, θ is the angle between the dipole moment $\tilde{\vec{d}}(\omega)$ and the direction of observation. The expression is normalized by the total emission driven by a plane wave pulse $P^d_{\mathrm{pw}}(\omega) = \int d\Omega P^d_{\mathrm{pw}}(\omega,\theta)$.

In Fig. 19, panel b), we show the dipole emission of the second and third harmonics in the top left and top right panels, respectively, in the xy-plane (orthogonal to the propagation direction of the beams). The beyond-dipole corrections, also resolved in the azimuthal angle, are shown in the xy plane in the lower panels. The emission produced by the plane wave and the Bessel beam is seen in the upper left panel, calculated with FMC. The difference in the angular dependence of the normalized $P^d(\omega,\theta)$ is larger in the case of even harmonics, as evidenced by the second harmonic for both cases. As seen in the upper left panel of Fig. 19b), the amplitude of the OAM beam emission shows an angle with respect to its plane wave counterpart.

The difference of emission calculated within EDA from that in the FMC approach (which can be seen in the beyond-dipole correction, Fig. 19b) lower left panel), clearly demonstrates that the angular difference is caused by the field gradient effects, henceforth the off-axis motion. The amplitude difference is up to 11.5 %, while a slight tilt emerges due to the P_y. We note that a beyond dipole correction for the plane wave case persists due to the z gradients; however, this correction displays no angular dependence in the xy plane.

Odd harmonics are much stronger because the driving field and the atomic potential have inversion symmetry. This forces the electron to accelerate in a way that naturally cancels even harmonics and reinforces odd ones. Hence, it is expected that the beyond-dipole corrections are much less considerable in the case of the odd harmonics. This is confirmed as seen in the case of the third harmonic angular spectrum in 19b), upper right panel. The dipolar contribution dominates the distribution strongly; therefore, the beyond-dipole correction is only on the order of 0.01%, as shown in the beyond-dipole correction plotted in the lower right panel. Thus, for the plane wave case, the correction in the second

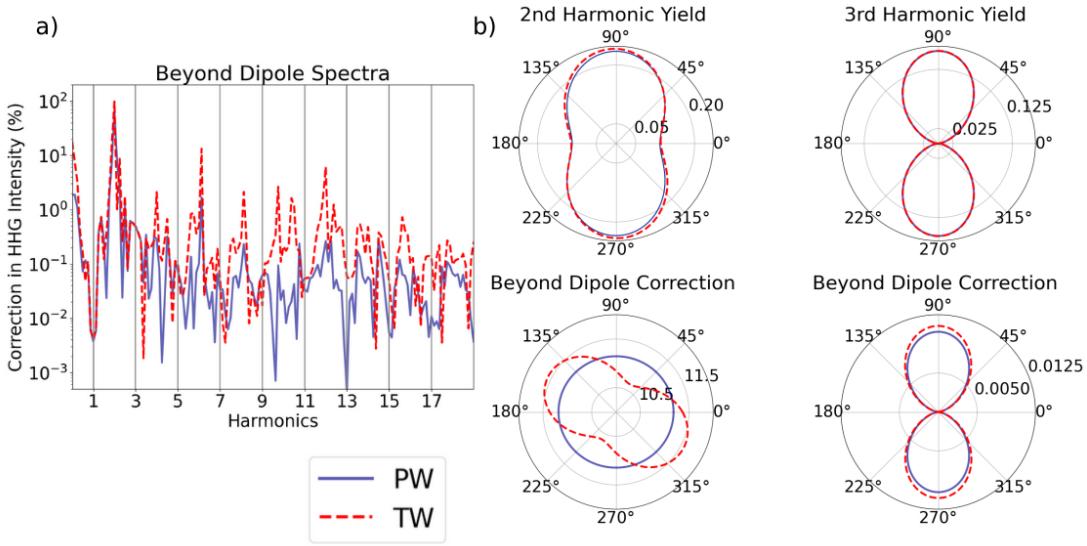

Figure 19: a) We calculate the spectra first using the FMC approach and then with the EDA for two cases: firstly, we use a Bessel beam with three components, A_{tw}^{3C}, (OAM), and then a plane wave (PW). We report the percentage difference between the two spectra. Beyond-dipole contributions are considerable at even harmonics, highlighting the need for beyond-dipole treatments to identify the symmetry-breaking phenomena. b) Angular distribution of the emission in the xy plane $\mathbf{P}^d(\omega, \theta)$ for second and third harmonics. The panels on the left correspond to the second harmonic, while the one on the right shows the results from the third harmonic. The upper panel from the left describes the angular distribution of total emission induced by a PW and a Bessel beam. In contrast, the lower left one describes the beyond dipole correction compared to the EDA. The right side shows total emission induced by a plane wave (PW) and Bessel beam for the third harmonic on the upper part, and the beyond dipole correction on the lower panel. Results here are normalized by total emission induced by the plane wave $P_{\mathrm{pw}}^d(\omega) = \int d\Omega P_{\mathrm{pw}}^d(\omega, \theta)$, where $d\Omega = \sin\theta d\theta d\varphi$. The figure is reproduced with permission from E. I. Albar et al., *Phys. Rev. A* **112**, 063109 (2025), published by the American Physical Society under the terms of the Creative Commons Attribution 4.0 International license.

harmonic is almost 100 times larger than that of the third harmonic.

In our simulations, we are also able to directionally resolve the beyond dipole corrections. Such corrections demonstrate the effect of gradient-driven motion. This then enables us to compare the scales of motion induced in the direction y and the propagation direction z. Note that the excitation in the y direction is only accessible with the transverse gradients of OAM beams. We plot the comparison of the corrections in these two directions in Fig. 20. We observe that

even though the beyond dipole correction in the y direction is limited to ≈ 1 %, it persists throughout the spectrum and stays relevant for even harmonics.

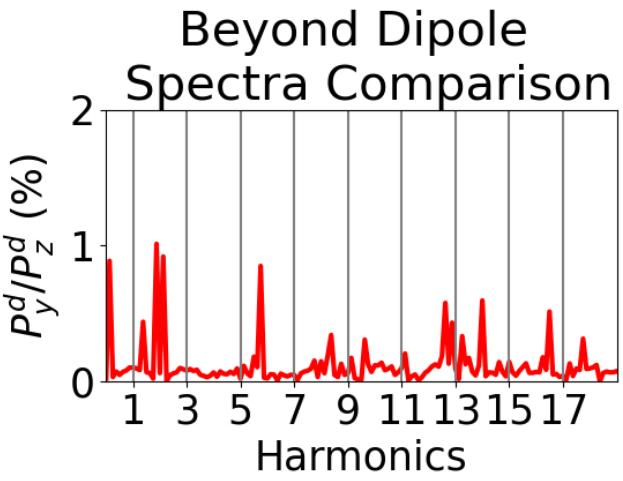

Figure 20: The ratio of beyond dipole corrections for y and z directions induced by a Bessel beam $\vec{A}_{\mathrm{tw}}^{3C}(\vec{r},t)$. The z component correction is considerable due to the combination of the large velocity in the x direction with the large magnetic field B_y. On the other hand, the y correction contains only the gradient-induced correction in the presence of transversal gradients of the OAM beam. However, the correction in the y direction remains relevant for all even harmonics and is inaccessible with plane waves.

Added to the possibility of measuring even harmonics without dipolar background [96], we believe the considerable correction in the emission visible in the second harmonic yield given in panel b) of Fig. 19 due to the deviations in the electron trajectory confirms that the second harmonic emission is a fitting candidate for an experimental observable, which provides a playground where the effect of OAM can be used to induce emission in all directions. While such a correction seen in Fig. 19 is not limited to an OAM-carrying Bessel beam, the correction for the plane wave is azimuthally symmetric, hinting that an angular deviation is inherent to incident OAM.

Predicting strong beyond-dipole corrections in the even harmonics is promising for experiments. Similar OAM induced effects in HHG have previously been observed in high odd harmonics [176]. As shown in Fig. 14, quadrupolar contributions dominate the even harmonics, making these harmonics fitting probes of beyond-dipole phenomena, in line with earlier work [171]. Combined with the fact that even harmonics can be measured without a dipolar background [96], the sizable correction shown in the second-harmonic yield (panel b of Fig. 19), which stems from modified electron trajectories, suggests that the second harmonic is a suitable experimental observable candidate. Even harmonics observed in the

off-axis directions offer a setting in which OAM can excite emission in all angular directions. Although similar corrections do appear for a plane-wave, they remain azimuthally symmetric, indicating that the angular asymmetry is connected to the OAM content of the incident field.

6.7 OAM as a Parameter to Tune Off-axis HHG

We propose the OAM number m as a tuning parameter for the off-axis emission, i.e., the third direction which is neither the polarization nor the propagation direction. To investigate the effect, we construct $\vec{A}_{\mathrm{tw}}^{\mathrm{3C}}$ Bessel beams with higher m. We place the atom at the first intensity ring (hot spot) for each case of m, with the amplitude and phase of the beams matched in the x direction, so that the dipolar effects are identical for all the beams. This implies that the field amplitude A_{tw} at the atomic position matches the plane-wave amplitude value $A_{\mathrm{pw}} = 0.053$ a.u. at $t = 0$. The atom is placed at $\vec{r}_0 = (r_0, 45°, 0)$ with r_0 adjusted for each OAM number m to locate the atom at the first intensity ring of the beam (hot spot). The chosen parameters used for all beams are reported in the Table 6.7.

Matching the phase for different beams is crucial, since the carrier envelope phase is shown to impact the HHG process strongly [177]. To match the total phase Φ_{pw} of the plane wave at $t = 0$ and $z = 0$ we calculate Φ_{tw} from the condition,

$$m\phi + \Phi_{\mathrm{tw}} = 0, \tag{107}$$

where $\phi = 45°$. For the case of $\vec{A}_{\mathrm{tw}}^{\mathrm{3C}}$, we used the same set of parameters as for $\vec{A}_{\mathrm{tw}}^{\mathrm{1C}}$. For the case of $\vec{A}_{\mathrm{tw}}^{\mathrm{3C}}$ we use the following formulas for the total angular momentum $m_{\gamma_1} \approx m + 1$ and $m_{\gamma_2} \approx m - 1$. We present the completely matched temporal behavior, including the envelope, of the beams in Fig. 21.

The complete matching of the temporal behavior and the amplitude of the beams presented in Fig. 21 enables us to perform an accurate comparison between different m. Adjusting solely m and the phase results in uncontrolled changes in the amplitude of the beams, which causes dipolar effects on the spectrum. Therefore, matching the amplitude in addition eliminates any undesired dipolar effect on the spectrum: the sole difference is the OAM number m. Therefore, one can connect the difference in spectra directly with the gradients at play.

In Fig. 22 we show the y dipole component spectra P_y^d normalized by the $m = 1$ case, for values of m ranging from 1 to 21. As shown in Fig. 17, the P_y^d spectra provide unequivocal evidence of effects arising from in-plane spatial structuring of the beams. Here, it becomes clear that this quantity is sensitive to

Table 1: Parameters used for the calculations of $\vec{A}_{\mathrm{tw}}^{1\mathrm{C}}$ and $\vec{A}_{\mathrm{tw}}^{3\mathrm{C}}$.

m	A_{tw} a. u.	r_0 nm	Φ_{tw}
1	0.0455	2545	1.4915
2	0.0543	4596	3.8481
3	0.0608	6081	6.2033
4	0.0661	7920	2.2779
5	0.0705	9334	4.6344
6	0.0745	10960	0.7059
10	0.0872	17324	3.8516
11	0.0898	18738	6.2082
20	0.1084	32527	2.2816
21	0.1102	33941	4.6332

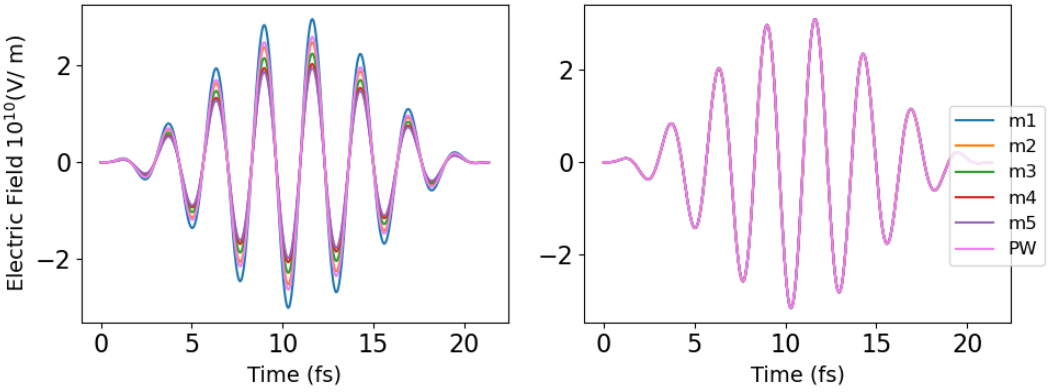

Figure 21: Phase-adjusted pulses for the cases of plane wave and OAM numbers ranging from 1 to 5. The left side shows the phase adjustment with the same assigned amplitude A_{tw}. Since the envelope and phase adjustment impose different amplitudes for varying OAM numbers m, we adjust the amplitudes as seen on the right side, where the temporal behavior of different beams matches in intensity and phase completely. With this setup, any dipolar variance between the beams is eliminated, and we can operate with the isolated effect of gradients governed by m.

the OAM number.

The top panel of Fig. 22 shows y dipole component spectra P_y^d as a function of OAM number m for the second harmonic, while the top panels show the results for the third harmonics. We observe that the second harmonic yield monotonously increases with m. On the other hand, the third harmonic yield shows a sudden drop between m from 1 to 3, and then increases. A saturation trend emerges for larger values of m in both cases. This trend follows the behavior of the field gradient for increasing values of m as shown in Fig. 23, where the y-derivative of the electric field of each beam is plotted at the hot-spot location. The explicit expression for the gradient of the linearly polarized Bessel beam

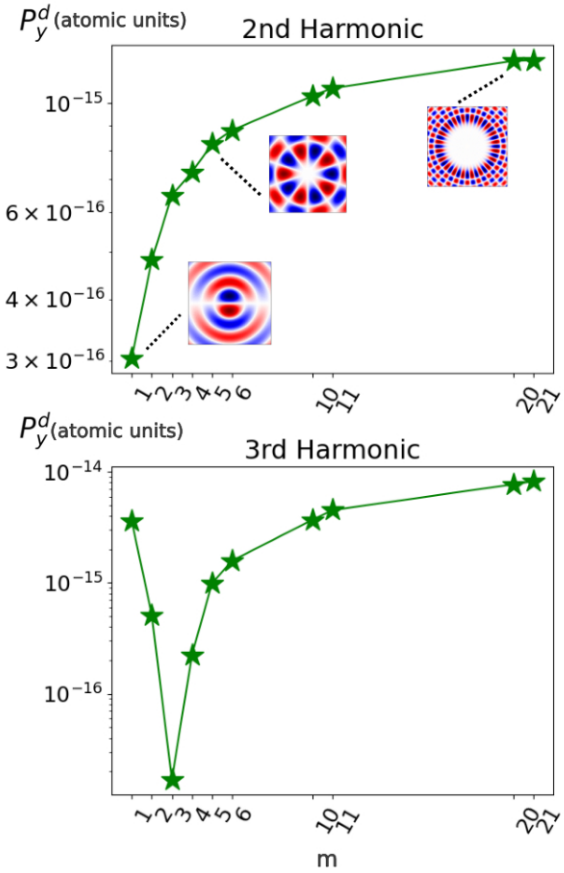

Figure 22: The y-dipole component spectra P_y^d for m ranging from 1 to 21 for the second and third harmonics. It is visible that P_y^d drastically depends on m. Here, the change of m affects mostly the second harmonic. Both harmonics show a saturation regime after $m = 10$. Here, the inset in the second harmonic graph displays the cross sections of beams with $m = 1$, $m = 5$, and $m = 20$. The presented results are calculated beyond the dipole approximation.The figure is reproduced with permission from E. I. Albar et al., *Phys. Rev. A* **112**, 063109 (2025), published by the American Physical Society under the terms of the Creative Commons Attribution 4.0 International license.

$\vec{A}_{\rm tw}^{\rm 1C}(\vec{r},t) = A_{\rm tw}^{\rm 1C}(\vec{r},t)\vec{e}_x$ from Eq. (99), is given as

$$\nabla_y A_{\rm tw}^{\rm 1C}(\vec{r},t) = A_{\rm tw} f(z)\left(\frac{\kappa y\left(J_{m-1}\left(r_\perp\kappa\right) - J_{m+1}\left(r_\perp\kappa\right)\right)\cos\left(m\phi + kz - \omega t\right)}{2r_\perp} - \frac{mxJ_m\left(r_\perp\kappa\right)\sin\left(m\phi + kz - t\omega\right)}{x^2+y^2}\right). \tag{108}$$

Fig. 23 shows the magnitude of the y gradient at the hotspots of each m number.

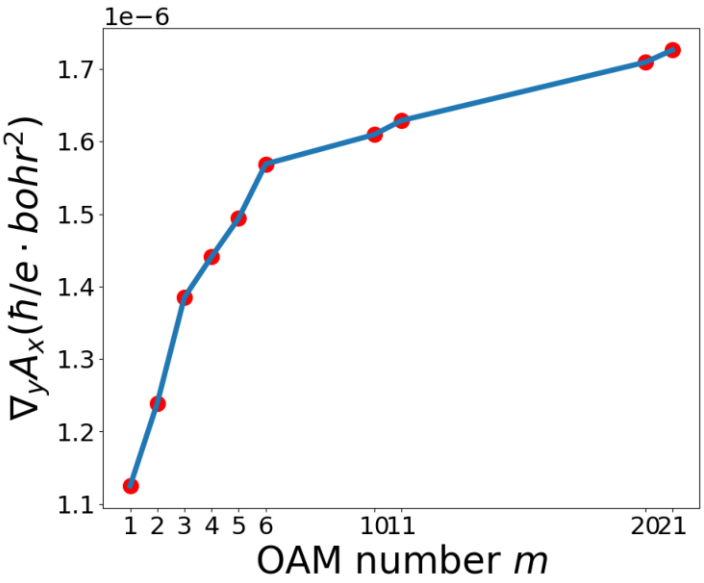

Figure 23: Maximum y gradient (∇_y) for each OAM number m. The rapid initial increase of the amplitude of the gradient is saturated as one moves to higher OAM numbers.The figure is reproduced with permission from the supplemental material of E. I. Albar et al., *Phys. Rev. A* **112**, 063109 (2025), published by the American Physical Society under the terms of the Creative Commons Attribution 4.0 International license.

In addition to the P_y^d dipole component, we calculated the angular emission spectra for different values of m for the second and third harmonic in Fig. 24. Here, we report the correction entailed by the OAM number m. We observe that this correction for the second and third harmonics also exhibits angular dependence. It can be seen that for the second harmonic, both the angle and intensity of the emission depend on the OAM number. This implies that not only the amplitude of the yield, but also the angle of the emission for the second harmonic, represents a fitting candidate for OAM tuning. In contrast, for the third harmonic shown in Fig. 24, only the intensity increases.

These findings demonstrate that the nonlinear response for the even harmonics depends strongly on the OAM number of the beam, following a similar trend to the field gradients. This suggests that a path to incorporate beyond-dipole effects in simulations of HHG from a gas-phase target is possible through the even harmonics of off-axis direction.

6.8 Effects of Molecular Symmetry: Benzene

To investigate effects of molecular symmetry, we perform in this section HHG calculations using the benzene molecule and a circularly polarized plane wave beam. We compare the EDA and the FMC approaches to identify beyond dipole corrections. We confirm that the effects of symmetry breaking in the propagation

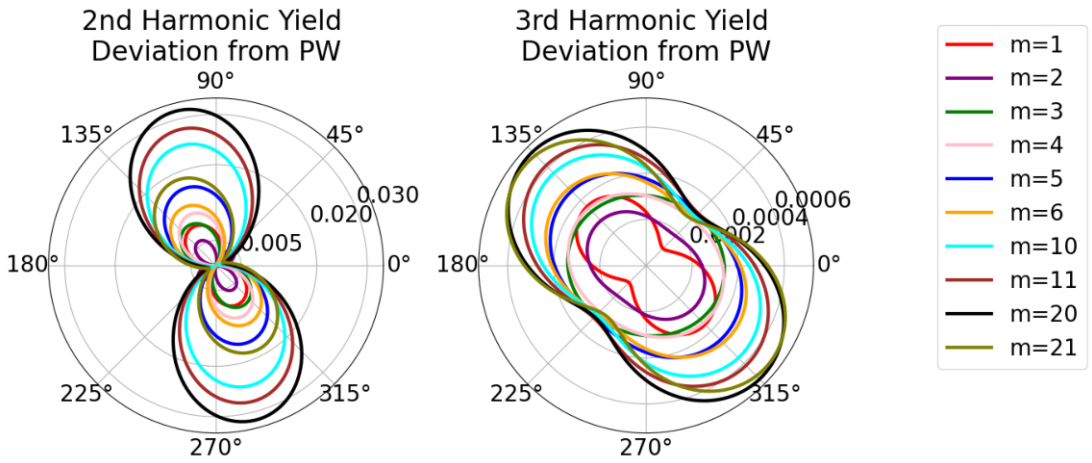

Figure 24: Angular distribution of the deviation from plane wave results as a function of OAM number m. The left panel is reserved for the correction of the second harmonic, while the right panel shows that of the third harmonic.The figure is reproduced with permission from the supplemental material of E. I. Albar et al., *Phys. Rev. A* **112**, 063109 (2025), published by the American Physical Society under the terms of the Creative Commons Attribution 4.0 International license.

direction of the incident field survive in the beyond dipole HHG spectra of the benzene molecule.

As before, we perform the real-space real-time TDDFT calculations with Octopus. In particular here, we employ Troullier-Martins norm-conserving pseudopotentials as provided by the Octopus distribution to describe carbon and hydrogen cores, see [178]. The timestep is set to 0.0036 fs, and for the time propagation, the AETRS scheme is employed. A rectangular simulation box of $4.44\times4.44\times3.2$ nm^3 is employed, where the benzene molecule is aligned with the xy plane as shown in Fig. 25. The pulse is also polarized in x and y directions, where the excursion is expected to be the largest. The grid spacing is 0.02 nm. Absorbing boundaries of 0.52 nm are placed around the electronic box [118].

We employ a right-circular polarized beam

$$\vec{A}_{\rm pw}(\vec{r},t) = A_{\rm pw} f(z)\cos(k_z z - \omega_b t)\hat{e}_x + A_{\rm pw} f(z)\sin(k_z z - \omega_b t)\hat{e}_y, \qquad (109)$$

with a central wavelength of 800 nm. Following the recipe described in Sec. 6.1, we impose a spatiotemporal envelope on the beam and form a pulse of 10 cycles. The beam amplitude is set to yield a peak electric field of 3.82×10^{10} V/m.

We present our results in Fig. 25. Here, part a) depicts the setup, while part b) shows the dipole moment dynamics on xz plane. We observe that the EDA approach is insufficient to capture the radiation pressure effects in the propagation direction, similar to the case of hydrogen as shown in Fig. 16. In part c) of the

figure we present HHG spectra: the left side of the upper panel shows the spectra calculated with the two approaches. We would like to highlight that the EDA results are multiplied by a factor of 5 for visualisation purposes of this plot. Hence, we can observe the symmetry effect on the HHG spectrum of benzene. Since the dipole operator allows only one unit of angular momentum transfer, the 6-fold symmetry of the molecule yields $6k \pm 1$ peaks within EDA [179, 180]. However, when one moves beyond the EDA, the contribution from other peaks such as $6k \pm 2$ is visible, as seen clearly in the right-hand logarithmic side.

The lower part of Fig.25c) shows the direction-resolved spectra for the benzene molecule. The left side shows the FMC results, while the right side shows the EDA results. Similar to the previous section, we see that the contribution in the propagation direction P_z^d is invisible within the EDA. This can be explained with the dynamics shown in Fig.25b): since the motion in the z direction is not captured, the corresponding contribution to the spectrum is discarded within the EDA. Moreover, the beyond-dipole side peaks at $6k \pm 2$ and beyond, stemming from the inclusion of beyond dipole effects, are visible in P_x^d and P_y^d components on the left-hand side. We observe that the symmetry-breaking effect in the z direction is visible in the even harmonics in particular. The even P_z^d peaks show yet another interesting pattern, where the 6th and 12th harmonics are the strongest peaks, which shows that the effect of the 6-fold symmetry is also imprinted on the even harmonics.

To conclude, we study the beyond-dipole effects in HHG in the presence of optical vortices with OAM. We find that these corrections are predominant for even harmonics, which appear due to the symmetry breaking. We show that the in-plane gradients of the structured fields excite the dynamics. This behavior is visible solely beyond the dipole approximation and results in a tilt in the angular distribution of the emitted radiation for the second harmonic, a tendency that can be generalized to even harmonics.

We have shown that the effect of the often neglected components of the vector potential for optical vortices is non-negligible and demonstrate that taking them into account while analyzing component-resolved spectra is of utmost importance. We show that it is possible to tune the harmonic yield in both off-axis and on-axis directions by adjusting the OAM number of the Bessel beam, since the beyond-dipole corrections of the even harmonics match the trend of the electric field gradients, especially the second harmonic. We extend our analysis to the benzene molecule in the final section and investigate the beyond dipole implications that the molecular symmetry entails. An approach that incorporates both microscopic and macroscopic effects, for instance, studies an extensive gas target and models the propagation in a medium while accounting for the phase

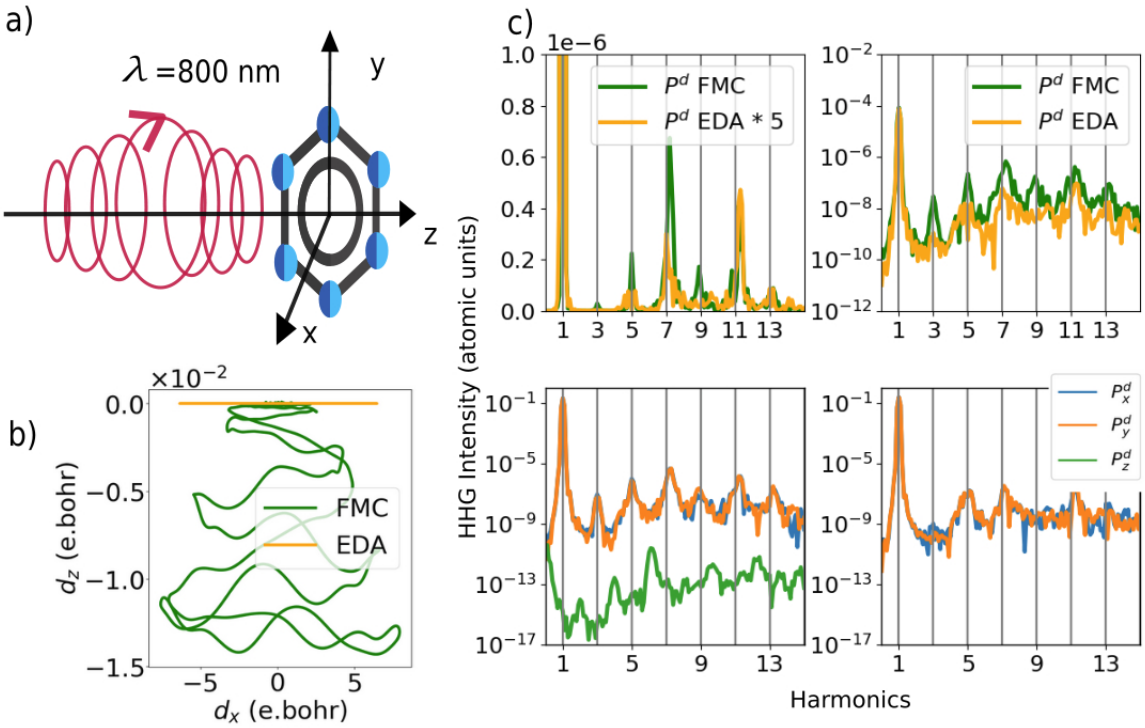

Figure 25: a)High harmonic generation with a benzene molecule aligned with the xy plane, using a circularly polarized pulse with a wavelength of 800 nm. b) Dipole moment dynamics in xz plane, showing that the neglected component in the propagation direction z is captured by the FMC approach. c) High harmonic generation spectra for the EDA and the FMC approaches. On the upper panel, results are shown on the linear scale to highlight $6k \pm 1$ peaks on the left side, and the right side shows the logarithmic scale. The EDA approach is multiplied by a factor of 5 in the linear scale for visualization purposes. The lower panel is reserved for the direction-resolved spectra for two approaches: the left side shows the FMC spectra and the right side shows the EDA spectra.

matching from individual dipoles, can provide further insights into possible experimental setups for detecting and manipulating beyond-dipole effects in nonlinear spectroscopy with structured light.

7 Wave Packet Dynamics: an Application of the Full Minimal Coupling FMC Formalism*

A wave packet is a combination (packet) of plane waves with a spanning a range of frequencies around a central frequency ω. Usually described with a Gaussian form, a wave packet evolves with time, with momentum defined by its wave vector. The wave-particle duality finds a fitting expression in the concept of a wavepacket. In quantum mechanics, wave functions are used to describe wave properties of the system, such as interference and diffraction. However, a single plane wave is completely delocalized, i.e., it extends infinitely and thus cannot represent a particle confined in space. When many plane waves with slightly different momenta are superposed, as in the case of a wave packet, a localized quantum state that moves as a whole through space and time is formed. This picture brings the wave and the particle together [181]: the oscillatory components of the wave packet correspond to the wave nature, while the localization imposed by the envelope encapsulates the particle-like behavior.

Consequently, a wave packet model provides a unified description of classical and quantum phenomena. A well-localized wave packet under a smooth potential U represents the classical properties via its mean position $\langle x \rangle$ and mean momentum $\langle p \rangle$, which reproduces Newton's second law as described with Ehrenfest's theorem

*Parts of this chapter, including figures and text excerpts, are adapted from the author's previously published work: Bonafé, F.P., Albar, E.I., Ohlmann, S., Kosheleva, V.P. et al. Full minimal coupling Maxwell-TDDFT: An ab initio framework for light-matter interaction beyond the dipole approximation Phys. Rev. B 111, 085114 (2025), Published by the American Physical Society under the terms of the Creative Commons Attribution 4.0 International license.

$$- m\frac{d\langle x\rangle}{dt} = \langle p\rangle, \qquad \frac{d\langle p\rangle}{dt} = -\frac{dU}{dx}. \tag{110}$$

The wave packet moves with the group velocity $v_g = \frac{d\omega}{dk}$ as a whole, which can be used to model a classical trajectory. On the other hand, a wave packet follows the Schrodinger equation and displays quantum behavior since it spreads, splits, tunnels, and interferes.

The flexibility of the wave packet then makes it a powerful tool for modeling a vast variety of phenomena, ranging from the tunneling of nuclei, photons and electrons, to photoelectrons in high-harmonic generation [182–184]. In this chapter, we employ the simple wave packet to model a charged particle with the goal of investigating the Vavilov-Cherenkov Radiation.

Vavilov-Cherenkov Radiation is the emitted radiation from a particle that is traveling faster than the speed of light in a medium [185, 186]. The shape of the accompanying emission, namely 'Cherenkov cone', can be thought of as the electromagnetic counterpart of the acoustic phenomenon of the Mach cone [187]. A Mach cone forms when particles in the air fail to respond to a supersonic object and accumulate into a shock front while clashing into each other. Similarly, a charged particle moving rapidly through a medium outruns the polarization response of its constituents. Since the fastest way for the dipoles to align themselves to the moving particle would be to react with the speed of light, and since the phase velocity of light is exceeded by the particle as it travels, a similar shock wave appears. Finally, an instantaneous burst of radiation emerges in the Cherenkov case, similar to the sonic boom of the Mach cone.

Cherenkov radiation is used for imaging in any setup where energetic charged particles move faster than light in a medium, producing a cone of coherent blue light that can be recorded and analyzed. In nuclear reactors, Cherenkov imaging verifies the presence of beta particles in water. In astrophysics, imaging atmospheric Cherenkov telescopes detect Cherenkov light in the atmosphere. In medical applications, Cherenkov luminescence imaging visualizes the distribution of the delivery of radiation dose inside tissue [188]. Across all these fields, Cherenkov imaging provides clues about the high-energy particles via detectable light patterns. As probing the Cherenkov angle is crucial to extract information from the superluminal travel of particles in such a wide range of applications [189], beyond-dipole self-consistent corrections to the spatial distribution of the wavepacket, as well as its dynamics, would have practical implications.

In this chapter, we perform numerical simulations employing a wave packet traveling at a higher speed than that of light in a medium, intending to investigate

Cherenkov radiation. To understand the effect of coupling between the wave packet and its emitted radiation, we put a variety of approaches to test: we first compare the EDA and FMC approaches, which enable us to account for the spatial variations of the electromagnetic field. Then, we switch the back reaction of the emitted field on the wave packet on and compare the observables with the switched-off case. As the radiated Cherenkov field is highly inhomogeneous and is emitted in the vicinity of the particle, backward-coupling of the induced radiation in the dynamics of the particle itself could, in principle, have considerable effects. This framework is a thorough demonstration of the beyond-dipole light-matter interaction.

To observe the effect of back-reaction and the level of coupling on the particle, we employ a Gaussian electronic wave packet. However, real-time propagation of the wave packet in real space proves to be nontrivial numerically. In the following subsections, we provide the details of this challenge imposed by the principle of uncertainty, and we provide our optimized simulation parameters. Then we proceed to present our results, which show that in order to capture the spatiotemporal symmetry breaking in Cherenkov radiation, one needs to account for both the beyond dipole corrections and the back reaction of the emitted radiation on the wave packet.

7.1 The Real-Space Real-Time Simulation Challenge: The Principle of Uncertainty

A challenge is to simulate the system with the following constraints: a wave packet requires several grid points to capture the oscillations of the wave function, while the finite simulation box sets a limit on the width and path of the system, as described in the schematic Fig. 26. The principle of uncertainty binds the momentum spread δp and the position spread δx of the wave-packet inversely:

$$\delta p = \frac{\hbar}{2\delta x}. \tag{111}$$

We need a well-defined momentum to get a considerable width in space to observe the time evolution of the wave packet shape. If the width is large enough, the wave packet disperses slowly and preserves its initial shape while traveling in space. This eases the observation of temporal changes in the shape of the wave packet. Only when the wave packet is allowed to propagate for a sufficient time without fully dispersing does the emitted radiation become observable and begin to act back on the wave packet.

The De Broglie wavelength of the system is a decisive parameter. The phase velocity of the wave packet has to be larger than that of light in the medium

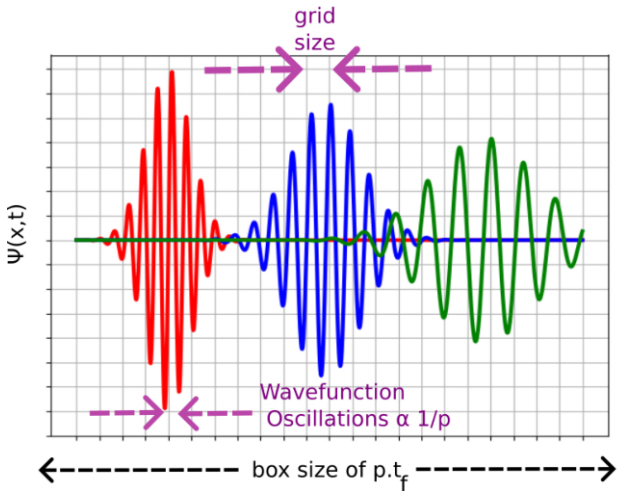

Figure 26: The schematic describing the bottlenecks of the simulation. The box size should be large enough to cover the motion. On the other hand, the grid spacing should be sufficiently small to describe the oscillations of the various components of the wave packet.

to observe Cherenkov radiation. However, as the momentum $\vec{p}$ increases, the accompanying wavelength λ decreases due to the De Broglie relation

$$\lambda = \frac{2\pi}{\vec{p}}. \tag{112}$$

7.2 Optimization of the numerical setup implemented in the Octopus-Code

The spatial oscillations have to be described accurately with the discretization of the simulation box. Therefore, the decreasing wavelength entails the need for a denser mesh to fully describe the wave characteristics. As the spreading in the position necessitates a larger simulation box, the dense grid represents a challenge in the calculation. With this in mind, we perform calculations to cover a sufficiently long simulation duration (with an elongated box in the propagation direction) where we can thoroughly capture the deformation of the wave packet as it disperses and emits.

The initial condition for a single electron wave packet is

$$\varphi(x,y,z,t=0) = C_0 e^{-ip(x-x_0)} e^{-\frac{1}{4}\left(\frac{x^2}{(\Delta x)^2}+\frac{y^2}{(\Delta y)^2}+\frac{z^2}{(\Delta z)^2}\right)}. \tag{113}$$

Here C_0 denotes the amplitude while Δx, Δy, and Δz indicate the width of the wave packet in three directions. The phase factor $e^{-ip(x-x_0)}$ describes the motion: the wave packet moves with a velocity of amplitude p along the x direction,

starting from point x_0. Due to the system being a simple one-electron Gaussian electronic wave packet, the Kohn-Sham Hartree exchange-correlation potential is zero. The explicit coupling between the electronic and Maxwell subsystems is through the FMC or EDA Hamiltonian, depending on the approach.

The simulation setup defines two subsystems using the multisystem feature of the Octopus-code, as detailed in Sec. 4.7. The first system is a Maxwell subsystem, which solves the time-dependent Maxwell's equations for the emitted electromagnetic field, and the second one is an electronic subsystem that evolves according to the time-dependent Schrödinger equation. The grid spacing for the matter subsystem is set to 0.016 nanometers, while the Maxwell grid is coarser by a factor of two. This nested grid configuration allows the electromagnetic fields to propagate into the Maxwell grid. The Maxwell box surrounds the electronic one and extends for another 0.53 nm in each direction to capture the emitting radiation. The Maxwell boundary conditions are set to a Perfectly matched layer (PML), as detailed in 5 [190]. The PML region spans another 0.53 nm around the Maxwell grid so that electromagnetic energy leaving the domain is attenuated and parasitic reflections are prevented.

Both the electromagnetic and electronic systems are propagated in time using the exponential midpoint integrator described in Sec. 4.2, Eq. (15). The bottleneck for the timestep is the emission solved by Maxwell's equations. According to the Courant-Friedrichs–Lewy (CFL) stability criterion, which ensures that the physical wave cannot travel faster than one spacing at one time step, the spacing Δx is bound with time discretisation

$$\Delta t < \frac{1}{c}\sqrt{\frac{1}{\Delta x^2 + \Delta y^2 + \Delta y^2}}. \tag{114}$$

Thus, a time step of 0.0025 atomic units of time (6.05 $\times 10^5$ fs) is chosen for both systems to respect the stability condition. The common timestep allows for the direct exchange of the relevant quantities during the calculation without time interpolation. For instance, the vector potential in the case of backwards reaction plus the full minimal coupling case, or the current density from the wave packet to the Maxwell box.

For the calculations, we optimized the electronic simulation box for the Octopus-code calculation to have the non-uniform dimensions of $60\times18\times18$ bohr^3 with an equal spacing of 0.3 bohr. We employ a box with a larger dimension in the propagation direction for a longer time evolution. The wave packet has a full width half maximum (FWHM), i.e. a position spread δx of 5.5 bohr, while the spread in the other two dimensions is $\delta y = \delta z = 2.5$ bohr. We apply an offset of -30 nm in the x direction. This allows us to propagate the system for a short time before

it arrives at the box boundary, hence we can observe time-dependent differences between different approaches. The wave packet has a velocity $v = \frac{p}{m} = 2.5$ a.u., where the phase velocity of light is set to 1.37 a.u., which yields a factor of 1.825 between the velocities of the wave packet and that of light in the medium.

With these parameters, we are able to propagate the wave packet and observe the emergence of a Cherenkov cone, while analysing the effect of the emitted field on the density distribution of the wave packet. We present the results of these two simulation setups in the following section.

7.3 Results

We aim to understand the beyond-dipole mechanisms at play during Cherenkov radiation. With this goal, we employ the flexible multisystem approach of the Octopus code and perform calculations with EDA and FMC approaches. As detailed before, in the FMC approach, both the spatial and temporal dependence of the vector potential are retained, meaning that the effects of the magnetic field, the radiation pressure, and retardation are naturally included. On the other hand, the simulations of an electronic wave packet travelling at a higher velocity than the phase velocity of light in a medium serve yet another purpose: not only the space dependence, but also the cross-talk of light and matter is also a topic of interest. We refer to the effect of the emitted field back on the wave packet as *'back-reaction'*. Our setup allows us to switch the back-reaction on and off freely, hence we can investigate the different levels of coupling (EDA and FMC) while accounting for this contribution.

An observable that many applications extract information from is the Cherenkov angle, which is the angle the Cherenkov cone has with the axis of motion. The non-dispersive Cherenkov angle where the system does not experience energy losses is defined as

$$\beta_{non-disp} = \arctan\left(\frac{c_m}{v_{wp}}\right). \tag{115}$$

Here, c_m denotes the speed of light in the medium and v_{wp} denotes the speed of the particle described by the wave packet. As the wave packet travels from right to left in Fig. 27, we measure the Cherenkov angle and compare it to the non-dispersive Cherenkov angle. Since we can describe the time-dependent behavior of both the particle and the emission, we observe that this angle is indeed time-dependent. As the particle starts the motion, the angle starts from zero to reach the usually defined ratio. This demonstrates how spherical wavefronts interfere and form an angle as the wave packet travels. The spherical form of the newly forming wave is visible in the left panel of Fig. 27.

As shown in the three top rows of Fig. 27, as time evolves, the wavepacket

disperses, while the emitted electric field (x-component, in this case) starts to develop the well-known Cherenkov cone. The non-dispersive Cherenkov angle is given by $\beta_{non-disp} = 56.8°$. Here we study the birth of the Cherenkov radiation and the time evolution of the angle, being first close to 90° (initial field aligned with the axis of propagation), as it develops and tends to $\approx 54°$ as can be seen in the bottom panel of Fig. 27. The slight difference with the non-dispersive value can be attributed to the dispersion of the wave packet and the numerical resolution of the grid. This is a dynamic demonstration of the spherical wave fronts interfering and forming the angle as the wave packet travels.

When we include the back-action corrections, as shown in the middle panels of Fig. 27, both for dipolar and full minimal couplings, we observe that the corrections to the density and the emitted field are around 0.1% with dipolar back-reaction (spatial average of the radiated field), but over 3% with full minimal coupling back-reaction. The dipolar correction shows the expected dipolar pattern in the direction of propagation of the wave packet, namely a slight shift in space of the density (which can be interpreted as a slightly larger velocity with respect to the uncoupled case). However, the correction with full minimal coupling displays a rich spatial distribution, creating a slight accumulation on the front and lateral sides, and a strong depletion on the back of the wave packet, thereby deforming the shape of the wave packet. The emitted field also shows an increase in the wavefront width and a decrease (in absolute values) of the field at the tip of the cone. In the literature, the corrections to Cherenkov dynamics have been addressed in a non-perturbative QED approach [191].

As expected, the wave packet disperses as it moves. In Fig. 28, the leftmost panel shows the density distribution of the electronic wave packet calculated with the FMC formalism. It discards the contribution from the back reaction of the emitted radiation. The middle panel is reserved for the difference between backward reactions on and off cases for the EDA approach. In the EDA, the space dependence of the emitted field is not considered, hence we see a uniform difference between the two cases. Therefore, the change in the dispersion of the wave packet due to its emitting fields and the effect of the field acting back on the packet are not fully captured. The rightmost panel shows the FMC calculations with the difference in the back-reaction. The difference stemming from the effect of the back-reaction grows with time. This is due to the emitted field growing in intensity and acting back more strongly; henceforth, accounting for the space dependence is not sufficient to capture the interaction thoroughly.

The symmetry breaking of the wave packet along the axis of propagation is visible only when the FMC approach is combined with the effect of back-reaction, as presented in Fig. 28. The electronic density distribution of the wave packet

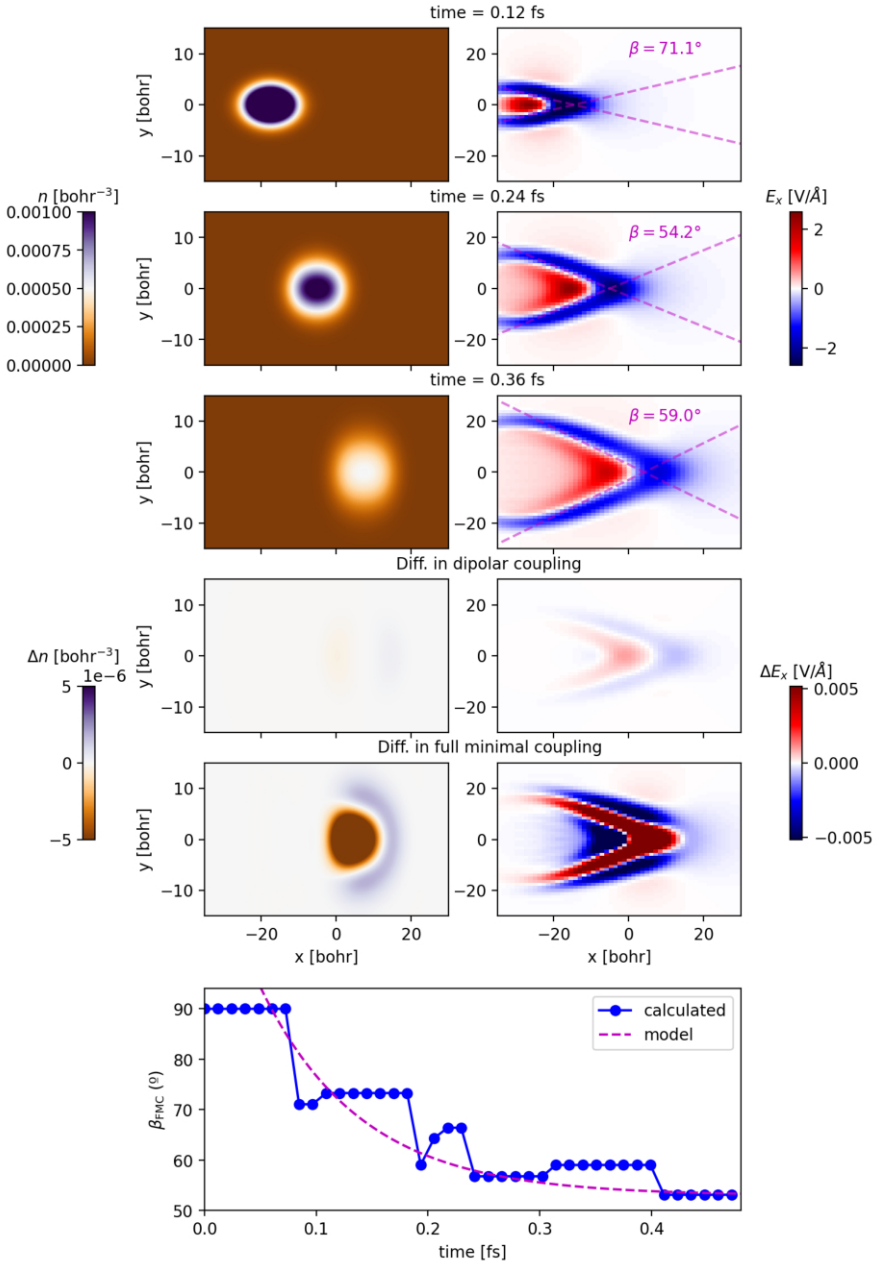

Figure 27: The electronic density distribution and transverse electric field for different time steps are given at the top panel, beyond dipole corrections that are the difference of dipolar and full minimal coupling reside in the middle; and dynamics of the Cherenkov angle formation are given in the bottom. For the three time snapshots chosen in the top panels, the wave packet is not subjected to an external drive and is free of the back-reaction of the emission. It can be seen how the wave packet disperses while the radiation forms the well-known cone. We observe that a rich angular dependence arises in our full minimal coupling approach. The angle dynamics (bottom) show the time evolution of the angle measured from the simulations (calculated) together with an exponential fit (model) with a characteristic time of 0.09 fs. The figure is reproduced with permission from Bonafé et al., *Physical Review B* **111**, 085114 (2025), licensed under CC BY 4.0.

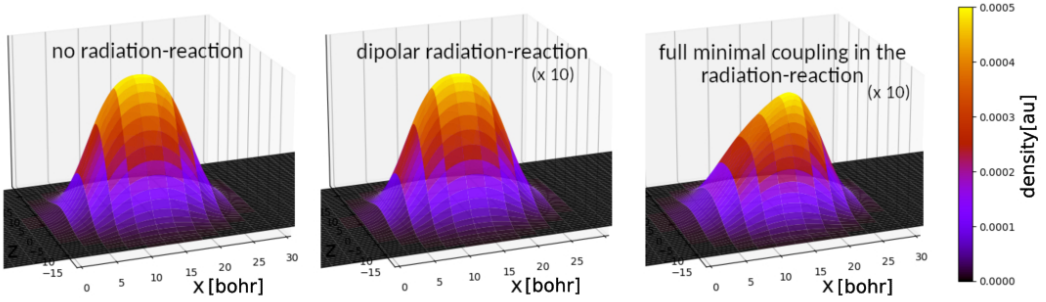

Figure 28: Evolution of the density of the wave packet for different time steps, and the difference when the back-reaction is turned on. The first panel plots the density of the wave packet as it travels. This panel shows the result of a calculation without back-reaction. The middle panel shows the difference in density for the electric dipole approximation and the case without back-reaction. We observe that the difference between the levels of coupling, i.e., the space dependence of the phenomenon, increases as time progresses. The third panel shows the density difference when the calculation is performed using the full minimal coupling approach, while the back reaction of the emitted field is taken into account. Only with the combination of these two approaches, the symmetry breaking along the propagation axis becomes visible.

is deformed from its initial Gaussian shape during the time evolution, and going beyond the dipole approximation is necessary to distinguish the directionality of the motion and its effect on the dispersion of the wave packet. Moreover, accounting for the back reaction of the field is the only way of observing the pressure difference that results in the spatial redistribution of the density. We want to stress that, while the spatial deformation of the wave packet has been exaggerated by a factor of 10 to be able to visualize it, the actual deformation of 3% after only 0.36 fs of dynamics is already surprising, and a huge motivation to study this topic further using the new tools developed in this thesis.

To sum up, we have demonstrated that observables such as the angle of Cherenkov radiation are time-dependent phenomena. Moreover, the symmetry breaking of the phenomenon can only be captured when two tools are combined: the FMC approach and the accounting of the back reaction of the electromagnetic field to the matter side. This highlights that the EDA approach is insufficient in modeling the emission of radiation with strong spatial dependence within the scales of the matter system. The fact that the back reaction of the emitted field was detectable in our calculations calls for further investigation of the forward-backward coupling of light and matter. Finally, the present toolbox enables us to simulate the non-perturbative dynamics of arbitrary particles described at the first principles level. Extending this framework to larger and more complex systems could provide a range of spectroscopic opportunities where detecting, as

well as engineering the symmetry-breaking mechanisms, becomes possible.

8 Conclusions & Outlook

8.1 Conclusion

In this thesis, we have contributed to the development and implementation of a multiscale approach to investigate light-matter interactions. Placing a spatial emphasis on the structured light, the starting point was to perform classical electrodynamics calculations to observe the structuring of such fields with a linear, non-magnetic medium. This has provided insights in terms of the classical formulation of OAM generation, and we were able to resolve the transformation of an ultra-short circularly polarized plane-wave pulse into a Bessel-like field. While the OAM density showed a pattern resembling earlier predictions [72], it was modified by the finite time envelope of the driving pulse. We discovered that the real space cross-section of a short pulse does not match completely with an idealized case with a pure OAM number: Since the openings of the spiral branches are matched to the central wavelength of the pulse, the structuring does not apply to all components of the frequency bandwidth. This concept is intensely studied in the context of spatiotemporal optical vortices (STOV)s, which are light pulses whose vortex structure is combined with temporal shape [192, 193]. Upon discovering that the geometry of current emitters emulates the nanoplasmonic structure and imprints their spatial distribution onto the phase structure of the far-propagating wave, we have investigated the impact of the imitated pulse on a two-particle test charge system, which we used as a probe of the local OAM density. When we displaced the position of the probe system, we saw that the trajectory was susceptible to the positioning across the transversal plane of the beam. This verified the necessity of accounting for the spatial structure of short OAM pulses.

Accounting for the spatial structuring of the light implies going beyond the EDA. To uncover the beyond-dipole phenomena that emerge from the interaction

of matter with the spatial structuring of light, we have applied the FMC tool to the HHG process. We discovered that the beyond dipole symmetry breaking induced by a plane wave in the propagation via the radiation pressure mechanism, predicted by other beyond dipole studies, is well captured within this approach. We firstly worked on the hydrogen atom to show that the OAM of light is expressed in the even harmonics of the beyond dipole trajectory components. We observed that the OAM induces motion in the third direction, which is neither the polarization nor the propagation direction of the linearly polarized beam. Named as the off-axis component, the even harmonics response of this contribution was perfectly tunable with the incident OAM content. When the gradient behavior is plotted as a function of OAM number, it becomes clear that this component was governed by the magnitude of the field gradients.

We also included the usually neglected components of the vector potential in twisted beams and showed that they are crucial for the accurate interpretation of the component-resolved spectra. To be consistent with the Coulomb gauge and to account for the longitudinal components of the Bessel beam is crucial to identify the contributions from the gradients.

The symmetry breaking induced by OAM beams manifests in the angular distribution of the light emission. Moreover, the benzene molecule investigation with a circular polarized plane wave showed that beyond dipole fingerprints are identifiable when a molecular symmetry is imposed as well.

The forward-backward coupling also proved to be relevant, as demonstrated in the Cherenkov wavepacket case. We captured how the Cherenkov angle evolves as a function of time thanks to our real-space real-time calculations. Most importantly, we combined two ingredients: the FMC description and the inclusion of the electromagnetic field's back-reaction on the particle, namely the forward-backward coupling. This combination revealed symmetry-breaking in the electronic density distribution of the wavepacket that the EDA cannot reproduce. This showed the importance of the strong variation of the radiation across the spatial scale of the matter system. The fact that the back-reaction is visible in our simulations also points to the need for further studies that account for the forward-backward coupling between light and matter.

Finally, the results of this thesis demonstrate that once the spatial structure, magnetic components, and induced fields of light are taken into account, the dynamics of light–matter interaction can differ noticeably from the predictions of the EDA. The FMC approach consistently revealed symmetry-breaking patterns and responses that the EDA cannot reproduce, whether in generated HHG or Cherenkov wavepacket propagation. These findings highlight that beyond-dipole effects need to be considered whenever structured fields vary on the scale of the

system or when the induced transverse fields become significant. The methods developed here provide a practical route for capturing such phenomena, and they offer a foundation for future studies aimed at understanding and utilizing these effects in more complex or experimentally realistic scenarios. Such outlooks will be discussed in the next section.

8.2 Outlook

The ramifications of this thesis work span many scales. Following the demonstration of the spatial dependence of the produced beam with Archimedean spirals and its slight difference from a pure OAM beam due to the temporal shape, a study that scans other designs can pave the way to better understand the interplay of STOVs and the design structure. Particularly, the structures with other phase-matching mechanisms than branch gaps, for instance, forked holograms, could yield beneficial insight that can be employed in plasmon-enhanced scattering spectra such as tip-enhanced Raman Spectroscopy (TERS).

The enforced understanding of nanoplasmonic generation of OAM has also significant implications for the use of structured fields with OAM inside cavities. It is already known that the time-reversal symmetry is broken in such setups with circularly polarized light [152]. On the other hand, experimental works using twisted light in cavities have already taken off [194]. Therefore, an analytical treatment that solves Maxwell's equations with active mirrors using the twisted light modes could have exciting applications and reveal additional symmetry-breaking mechanisms in non-equilibrium quantum materials.

The HHG part of the thesis shows that the extension of the formalism to the X-ray regime is necessary: The beyond dipole trajectory components of HHG are expected to persist in the produced X-ray radiation. The combination of the short wavelength that varies across the scale of the target, combined with the structured light, forms a fitting playground to uncover beyond dipole mechanisms.

Moreover, experimental studies of even harmonics that are the fingerprints of the symmetry breaking would be highly informative in both plane-wave and OAM driven cases. Particularly, our demonstration of OAM as a tuning parameter of even harmonics in the off-axis emission, combined with the circularly polarized driving of benzene, implies that intrinsic molecular symmetries could act as a knob of the HHG process. The possibility of selectively enhancing or suppressing specific harmonic peaks arises. The used symmetries of both the incident light and matter can effectively serve as a symmetry-sensitive filter or amplifier.

An extension of the HHG work is to incorporate the propagation through a medium instead of studying an individual emitter. Realistic experimental setups

necessitate the study of a larger number of target atoms and molecules. The first step would be to include more than one target atom in the electronic box and propagate the resulting HHG emission in a Maxwell solver box. This could help to investigate the phase-matching conditions between the emitters. Moreover, when it comes to molecules with inherent symmetries, the orientation conditions of the molecule with the incident beam should also be studied.

Following our work on the Cherenkov radiation, a natural next step is to extend our wavepacket framework to the regime of continuum states driven by twisted light [195]. The Cherenkov case already demonstrated the importance of accounting for the spatial distribution of the emitted radiation and capturing the back-reaction of the emitted field. Applying this approach to twisted ionization would enable us to explore how beyond-dipole mechanisms mediate the transfer of OAM from the driving field to continuum states. This direction is especially relevant for understanding light–matter interactions at the center of an OAM beam, where the field amplitude vanishes and the spatial gradients are at play.

The combination of the classical and quantum structured fields and the full minimal coupling can be expanded beyond the Born-Oppenheimer approximation. One can allow the ions to respond to the radiation pressure and optical torque of twisted fields [196], while also accounting for the beyond dipole electronic response. Although the results presented here focus on finite systems, the same approach naturally extends to periodic systems. This opens new routes for modeling and controlling light-driven dynamics in complex molecules and solids. Therefore, the present work lays the foundations for a new class of optical spectroscopies capable of probing beyond dipole fingerprints of nonequilibrium phenomena.

References

[1] Miguel A. L. Marques, Carsten A. Ullrich, Fernando Nogueira, Angel Rubio, Kieron Burke, and Eberhard K. U. Gross. *Time-Dependent Density Functional Theory*. Springer, Berlin, 2006. ISBN 9783540354260. doi: 10.1007/b11767107. URL http://dx.doi.org/10.1007/b11767107.

[2] Les Allen, Marco W. Beijersbergen, Rob J. C. Spreeuw, and Jan P. Woerdman. Orbital angular momentum of light and the transformation of laguerre-gaussian laser modes. *Physical Review A*, 45(11):8185–8189, 1992. doi: 10.1103/PhysRevA.45.8185.

[3] H. He, M. E. J. Friese, N. R. Heckenberg, and Halina Rubinsztein-Dunlop. Direct observation of transfer of angular momentum to absorptive particles from a laser beam with a phase singularity. *Phys. Rev. Lett.*, 75:826–829, Jul 1995. doi: 10.1103/PhysRevLett.75.826. URL https://link.aps.org/doi/10.1103/PhysRevLett.75.826.

[4] David G. Grier. A revolution in optical manipulation. *Nature*, 424:810–816, 2003.

[5] Changjun Min, Zhe Shen, Junfeng Shen, Yuquan Zhang, Hui Fang, Guanghui Yuan, Luping Du, Siwei Zhu, Ting Lei, and Xiaocong Yuan. Focused plasmonic trapping of metallic particles. *Nat. Commun.*, 4:2891, 2013. doi: 10.1038/ncomms3891.

[6] F. Tamburini, G. Anzolin, G. Umbriaco, A. Bianchini, and C. Barbieri. Overcoming the rayleigh criterion limit with optical vortices. *Physical Review Letters*, 97(16), October 2006. doi: 10.1103/physrevlett.97.163903. URL https://doi.org/10.1103/physrevlett.97.163903.

[7] C. Maurer, A. Jesacher, S. Bernet, and M. Ritsch-Marte. What spatial light modulators can do for optical microscopy. *Laser & Photonics Reviews*, 5 (1):81–101, December 2010. doi: 10.1002/lpor.200900047. URL https://doi.org/10.1002/lpor.200900047.

[8] Martín Drechsler, Sebastian Wolf, Christian T. Schmiegelow, and Ferdinand Schmidt-Kaler. Optical superresolution sensing of a trapped ion's wave packet size. *Physical Review Letters*, 127(14), September 2021. doi: 10.1103/physrevlett.127.143602. URL https://doi.org/10.1103/physrevlett.127.143602.

[9] Omar S Magaña-Loaiza and Robert W Boyd. Quantum imaging and information. *Reports on Progress in Physics*, 82(12):124401, nov 2019. doi: 10.1088/1361-6633/ab5005. URL https://dx.doi.org/10.1088/1361-6633/ab5005.

[10] Daniele Cozzolino, Davide Bacco, Beatrice Da Lio, Kasper Ingerslev, Yunhong Ding, Kjeld Dalgaard, Poul Kristensen, Michael Galili, Karsten Rottwitt, Siddharth Ramachandran, and Leif Katsuo Oxenløwe. Orbital angular momentum states enabling fiber-based high-dimensional quantum communication. *Phys. Rev. Appl.*, 11:064058, Jun 2019. doi: 10.1103/PhysRevApplied.11.064058. URL https://link.aps.org/doi/10.1103/PhysRevApplied.11.064058.

[11] Maria Solyanik-Gorgone, Andrei Afanasev, Carl E. Carlson, Christian T. Schmiegelow, and Ferdinand Schmidt-Kaler. Excitation of e1-forbidden atomic transitions with electric, magnetic, or mixed multipolarity in light fields carrying orbital and spin angular momentum [invited]. *Journal of the Optical Society of America B*, 36(3):565, February 2019. ISSN 1520-8540. doi: 10.1364/josab.36.000565. URL http://dx.doi.org/10.1364/JOSAB.36.000565.

[12] Christian T. Schmiegelow, Jonas Schulz, Henning Kaufmann, Thomas Ruster, Ulrich G. Poschinger, and Ferdinand Schmidt-Kaler. Transfer of optical orbital angular momentum to a bound electron. *Nature Communications*, 7, 10 2016. ISSN 20411723. doi: 10.1038/ncomms12998.

[13] J. I. Fuks, G. F. Quinteiro Rosen, H. Appel, and P. I. Tamborenea. Probing many-body effects in harmonic traps with twisted light. *Physical Review B*, 107, 2 2023. ISSN 24699969. doi: 10.1103/PhysRevB.107.L081111.

[14] Andrei Afanasev, Carl E. Carlson, and Asmita Mukherjee. Off-axis excitation of hydrogenlike atoms by twisted photons. *Phys. Rev. A*, 88:

033841, Sep 2013. doi: 10.1103/PhysRevA.88.033841. URL https://link.aps.org/doi/10.1103/PhysRevA.88.033841.

[15] Andrei Afanasev, Carl E. Carlson, Christian T. Schmiegelow, Jonas Schulz, Ferdinand Schmidt-Kaler, and Maria Solyanik. Experimental verification of position-dependent angular-momentum selection rules for absorption of twisted light by a bound electron. *New Journal of Physics*, 20, 2 2018. ISSN 13672630. doi: 10.1088/1367-2630/aaa63d.

[16] G. F. Quinteiro, Ferdinand Schmidt-Kaler, and Christian T. Schmiegelow. Twisted-Light-Ion Interaction: The Role of Longitudinal Fields. *Phys. Rev. Lett.*, 119(25):1–5, 2017. ISSN 10797114. doi: 10.1103/PhysRevLett.119.253203.

[17] Jean Luc Bégin, Ashish Jain, Andrew Parks, Felix Hufnagel, Paul Corkum, Ebrahim Karimi, Thomas Brabec, and Ravi Bhardwaj. Nonlinear helical dichroism in chiral and achiral molecules. *Nature Photonics*, 17:82–88, 1 2023. ISSN 17494893. doi: 10.1038/s41566-022-01100-0.

[18] A. A. Peshkov, Y. M. Bidasyuk, R. Lange, N. Huntemann, E. Peik, and A. Surzhykov. Interaction of twisted light with a trapped atom: Interplay between electronic and motional degrees of freedom. *Phys. Rev. A*, 107:023106, Feb 2023. doi: 10.1103/PhysRevA.107.023106. URL https://link.aps.org/doi/10.1103/PhysRevA.107.023106.

[19] R. Lange, N. Huntemann, A. A. Peshkov, A. Surzhykov, and E. Peik. Excitation of an electric octupole transition by twisted light. *Phys. Rev. Lett.*, 129:253901, Dec 2022. doi: 10.1103/PhysRevLett.129.253901. URL https://link.aps.org/doi/10.1103/PhysRevLett.129.253901.

[20] Anton A. Peshkov, Elena Jordan, Markus Kromrey, Karan K. Mehta, Tanja E. Mehlstäubler, and Andrey Surzhykov. Excitation of forbidden electronic transitions in atoms by hermite–gaussian modes. *Annalen der Physik*, 535(9):2300204, 2023. doi: https://doi.org/10.1002/andp.202300204. URL https://onlinelibrary.wiley.com/doi/abs/10.1002/andp.202300204.

[21] A. A. Peshkov, A. V. Volotka, A. Surzhykov, and S. Fritzsche. Rayleigh scattering of twisted light by hydrogenlike ions. *Phys. Rev. A*, 97:023802, Feb 2018. doi: 10.1103/PhysRevA.97.023802. URL https://link.aps.org/doi/10.1103/PhysRevA.97.023802.

[22] A A Peshkov, S Fritzsche, and A Surzhykov. Scattering of twisted light from a crystal. *Physica Scripta*, 94(10):105402, aug 2019. doi: 10.1088/1402-4896/ab1c74. URL https://dx.doi.org/10.1088/1402-4896/ab1c74.

[23] Valeriy G. Serbo, Andrey Surzhykov, and Andrey Volotka. Resonant scattering of plane-wave and twisted photons at the gamma factory. *Annalen der Physik*, 534(3):2100199, 2022. doi: https://doi.org/10.1002/andp.202100199. URL https://onlinelibrary.wiley.com/doi/abs/10.1002/andp.202100199.

[24] Kayn A. Forbes and A. Salam. Kramers-heisenberg dispersion formula for scattering of twisted light. *Phys. Rev. A*, 100:053413, Nov 2019. doi: 10.1103/PhysRevA.100.053413. URL https://link.aps.org/doi/10.1103/PhysRevA.100.053413.

[25] V. P. Kosheleva, V. A. Zaytsev, R. A. Müller, A. Surzhykov, and S. Fritzsche. Resonant two-photon ionization of atoms by twisted and plane-wave light. *Physical Review A*, 102, 12 2020. ISSN 24699934. doi: 10.1103/PhysRevA.102.063115.

[26] A. Picón, A. Benseny, J. Mompart, J. R. De Vázquez Aldana, L. Plaja, G. F. Calvo, and L. Roso. Transferring orbital and spin angular momenta of light to atoms. *New Journal of Physics*, 12, 8 2010. ISSN 13672630. doi: 10.1088/1367-2630/12/8/083053.

[27] Sucharita Giri, Misha Ivanov, and Gopal Dixit. Signatures of the orbital angular momentum of an infrared light beam in the two-photon transition matrix element: A step toward attosecond chronoscopy of photoionization. *Phys. Rev. A*, 101:033412, Mar 2020. doi: 10.1103/PhysRevA.101.033412. URL https://link.aps.org/doi/10.1103/PhysRevA.101.033412.

[28] Yongkun Chen, Yueming Zhou, Min Li, Kunlong Liu, Marcelo F. Ciappina, and Peixiang Lu. Atomic photoionization by spatiotemporal optical vortex pulses. *Phys. Rev. A*, 107:033112, Mar 2023. doi: 10.1103/PhysRevA.107.033112. URL https://link.aps.org/doi/10.1103/PhysRevA.107.033112.

[29] Maksim D. Kiselev, Elena V. Gryzlova, and Alexei N. Grum-Grzhimailo. Angular distribution of photoelectrons generated in atomic ionization by the twisted radiation. *arXiv:2303.17272*, 2023.

[30] Maksim D. Kiselev, Elena V. Gryzlova, and Alexei N. Grum-Grzhimailo. Vector parameters in atomic ionization by twisted light: Polarization of the electron and residual ion. *Phys. Rev. A*, 109:023108, Feb 2024. doi: 10.1103/PhysRevA.109.023108. URL https://link.aps.org/doi/10.1103/PhysRevA.109.023108.

[31] T. Kaneyasu, Y. Hikosaka, M. Fujimoto, T. Konomi, M. Katoh, H. Iwayama, and E. Shigemasa. Limitations in photoionization of helium by an extreme ultraviolet optical vortex. *Phys. Rev. A*, 95:023413, Feb 2017. doi: 10.1103/PhysRevA.95.023413. URL https://link.aps.org/doi/10.1103/PhysRevA.95.023413.

[32] Giovanni De Ninno, Jonas Wätzel, Primož Rebernik Ribič, Enrico Allaria, Marcello Coreno, Miltcho B. Danailov, Christian David, Alexander Demidovich, Michele Di Fraia, Luca Giannessi, Klavs Hansen, Špela Krušič, Michele Manfredda, Michael Meyer, Andrej Mihelič, Najmeh Mirian, Oksana Plekan, Barbara Ressel, Benedikt Rösner, Alberto Simoncig, Simone Spampinati, Matija Stupar, Matjaž Žitnik, Marco Zangrando, Carlo Callegari, and Jamal Berakdar. Photoelectric effect with a twist. *Nature Photonics*, 14:554–558, 9 2020. ISSN 17494893. doi: 10.1038/s41566-020-0669-y.

[33] Willis E. Lamb and Robert C. Retherford. Fine structure of the hydrogen atom by a microwave method. *Phys. Rev.*, 72:241–243, Aug 1947. doi: 10.1103/PhysRev.72.241. URL https://link.aps.org/doi/10.1103/PhysRev.72.241.

[34] D. A. Glazov, A. V. Volotka, O. V. Andreev, V. P. Kosheleva, S. Fritzsche, V. M. Shabaev, G. Plunien, and Th. Stöhlker. Ground-state hyperfine splitting of b-like ions in the high-z region. *Phys. Rev. A*, 99:062503, Jun 2019. doi: 10.1103/PhysRevA.99.062503. URL https://link.aps.org/doi/10.1103/PhysRevA.99.062503.

[35] V. P. Kosheleva, A. V. Volotka, D. A. Glazov, D. V. Zinenko, and S. Fritzsche. g factor of lithiumlike silicon and calcium: Resolving the disagreement between theory and experiment. *Phys. Rev. Lett.*, 128:103001, Mar 2022. doi: 10.1103/PhysRevLett.128.103001. URL https://link.aps.org/doi/10.1103/PhysRevLett.128.103001.

[36] D. V. Zinenko, D. A. Glazov, V. P. Kosheleva, A. V. Volotka, and S. Fritzsche. Electron correlation effects on the g factor of lithiumlike ions. *Phys. Rev. A*, 107:032815, Mar 2023. doi: 10.1103/PhysRevA.107.032815. URL https://link.aps.org/doi/10.1103/PhysRevA.107.032815.

[37] V. P. Kosheleva, A. V. Volotka, D. A. Glazov, and S. Fritzsche. Many-electron effects in the hyperfine splitting of lithiumlike ions. *Phys. Rev. Res.*, 2:013364, Mar 2020. doi: 10.1103/PhysRevResearch.2.013364. URL https://link.aps.org/doi/10.1103/PhysRevResearch.2.013364.

[38] Tao E. Li, Hsing Ta Chen, Abraham Nitzan, and Joseph E. Subotnik. Understanding the nature of mean-field semiclassical light-matter dynamics: An investigation of energy transfer, electron-electron correlations, external driving, and long-time detailed balance. *Phys. Rev. A*, 100(6): 62509, 2019. ISSN 24699934. doi: 10.1103/PhysRevA.100.062509. URL https://doi.org/10.1103/PhysRevA.100.062509.

[39] Norah M. Hoffmann, Christian Schäfer, Niko Säkkinen, Angel Rubio, Heiko Appel, and Aaron Kelly. Benchmarking semiclassical and perturbative methods for real-time simulations of cavity-bound emission and interference. *J. Chem. Phys.*, 151(24), 2019. ISSN 00219606. doi: 10.1063/1.5128076. URL https://doi.org/10.1063/1.5128076.

[40] Norah M. Hoffmann, Christian Schäfer, Angel Rubio, Aaron Kelly, and Heiko Appel. Capturing vacuum fluctuations and photon correlations in cavity quantum electrodynamics with multitrajectory Ehrenfest dynamics. *Phys. Rev. A*, 99(6):063819, jun 2019. ISSN 2469-9926. doi: 10.1103/PhysRevA.99.063819. URL https://link.aps.org/doi/10.1103/PhysRevA.99.063819.

[41] Carlos M. Bustamante, Esteban D. Gadea, Andrew Horsfield, Tchavdar N. Todorov, Mariano C. González Lebrero, and Damián A. Scherlis. Dissipative Equation of Motion for Electromagnetic Radiation in Quantum Dynamics. *Phys. Rev. Lett.*, 126(8):87401, 2021. ISSN 10797114. doi: 10.1103/PhysRevLett.126.087401. URL https://doi.org/10.1103/PhysRevLett.126.087401.

[42] Maxim Sukharev. Efficient parallel strategy for molecular plasmonics – A numerical tool for integrating Maxwell-Schrödinger equations in three dimensions. *J. Comput. Phys.*, 477:111920, mar 2023. ISSN 00219991. doi: 10.1016/j.jcp.2023.111920. URL https://doi.org/10.1016/j.jcp.2023.111920https://linkinghub.elsevier.com/retrieve/pii/S0021999123000153.

[43] René Jestädt, Michael Ruggenthaler, Micael J.T. Oliveira, Angel Rubio, and Heiko Appel. Light-matter interactions within the Ehrenfest–Maxwell–Pauli–Kohn–Sham framework: fundamentals, implementa-

tion, and nano-optical applications. *Adv. Phys.*, 68(4):225–333, 2019. ISSN 14606976. doi: 10.1080/00018732.2019.1695875.

[44] Atsushi Yamada and Kazuhiro Yabana. Multiscale time-dependent density functional theory for a unified description of ultrafast dynamics: Pulsed light, electron, and lattice motions in crystalline solids. *Phys. Rev. B*, 99 (24):1–10, 2019. ISSN 24699969. doi: 10.1103/PhysRevB.99.245103.

[45] Nicholas; Rivera, Ido; Kaminer, Bo; Zhen, John D..; Joannopoulos, and Marin Soljačić. Shrinking light to allow forbidden transitions on the atomic scale. *Science*, 353:263–269, 7 2016. ISSN 0036-8075. doi: 10.1126/science.aaf6308. URL `http://www.sciencemag.org/lookup/doi/10.1126/science.aaf6308`.

[46] Stephan Bernadotte, Andrew J. Atkins, and Christoph R. Jacob. Origin-independent calculation of quadrupole intensities in X-ray spectroscopy. *J. Chem. Phys.*, 137(20), 2012. ISSN 00219606. doi: 10.1063/1.4766359.

[47] Patrick J. Lestrange, Franco Egidi, and Xiaosong Li. The consequences of improperly describing oscillator strengths beyond the electric dipole approximation. *J. Chem. Phys.*, 143(23), 2015. ISSN 00219606. doi: 10.1063/1.4937410. URL `http://dx.doi.org/10.1063/1.4937410`.

[48] Nicolás O. Foglia, Dimitrios Maganas, and Frank Neese. Going beyond the electric-dipole approximation in the calculation of absorption and (magnetic) circular dichroism spectra including scalar relativistic and spin-orbit coupling effects. *J. Chem. Phys.*, 157(8), 2022. ISSN 10897690. doi: 10.1063/5.0094709. URL `https://doi.org/10.1063/5.0094709`.

[49] Nanna Holmgaard List, Joanna Kauczor, Trond Saue, Hans Jørgen Aagaard Jensen, and Patrick Norman. Beyond the electric-dipole approximation: A formulation and implementation of molecular response theory for the description of absorption of electromagnetic field radiation. *J. Chem. Phys.*, 142(24), 2015. ISSN 00219606. doi: 10.1063/1.4922697. URL `http://dx.doi.org/10.1063/1.4922697`.

[50] Arto Sakko, Angel Rubio, Mikko Hakala, and Keijo Hämäläinen. Time-dependent density functional approach for the calculation of inelastic x-ray scattering spectra of molecules. *J. Chem. Phys.*, 133(17), 2010. ISSN 00219606. doi: 10.1063/1.3503594.

[51] Einar Aurbakken, Benedicte Sverdrup Ofstad, Håkon Emil Kristiansen, Øyvind Sigmundson Schøyen, Simen Kvaal, Lasse Kragh Sørensen, Roland

Lindh, and Thomas Bondo Pedersen. Transient spectroscopy from time-dependent electronic-structure theory without multipole expansions. *Phys. Rev. A*, 109(1):1–17, 2024. ISSN 24699934. doi: 10.1103/PhysRevA.109.013109.

[52] Dennis W. Lindle and Oliver Hemmers. Breakdown of the dipole approximation in soft-X-ray photoemission. *J. Electron Spectros. Relat. Phenomena*, 100(1-3):297–311, 1999. ISSN 03682048. doi: 10.1016/s0368-2048(99)00052-3.

[53] Morten Førre and Aleksander Skjerlie Simonsen. Generalized velocity-gauge form of the light-matter interaction Hamiltonian beyond the dipole approximation. *Phys. Rev. A*, 93(1):1–6, 2016. ISSN 24699934. doi: 10.1103/PhysRevA.93.013423.

[54] Takeshi Iwasa and Katsuyuki Nobusada. Nonuniform light-matter interaction theory for near-field-induced electron dynamics. *Phys. Rev. A - At. Mol. Opt. Phys.*, 80(4):1–11, 2009. ISSN 10502947. doi: 10.1103/PhysRevA.80.043409.

[55] M. Førre, J. P. Hansen, L. Kocbach, S. Selstø, and L. B. Madsen. Nondipole ionization dynamics of atoms in superintense high-frequency attosecond pulses. *Physical Review Letters*, 97:043601, 7 2006. ISSN 0031-9007. doi: 10.1103/PhysRevLett.97.043601. URL `https://link.aps.org/doi/10.1103/PhysRevLett.97.043601`.

[56] M. Førre, S. Selstø, J. P. Hansen, and L. B. Madsen. Exact nondipole Kramers-Henneberger form of the light-atom Hamiltonian: An application to atomic stabilization and photoelectron energy spectra. *Phys. Rev. Lett.*, 95(4):1–4, 2005. ISSN 00319007. doi: 10.1103/PhysRevLett.95.043601.

[57] Simon Vendelbo Bylling Jensen, Mads Middelhede Lund, and Lars Bojer Madsen. Nondipole strong-field-approximation hamiltonian. *Physical Review A*, 101(4), April 2020. ISSN 2469-9934. doi: 10.1103/physreva.101.043408. URL `http://dx.doi.org/10.1103/PhysRevA.101.043408`.

[58] Rešad KahvedŽić and Stefanie Gräfe. Shift of the photoelectron momentum against the radiation pressure force in linearly polarized intense midinfrared laser fields. *Phys. Rev. A*, 106(4):1–7, 2022. ISSN 24699934. doi: 10.1103/PhysRevA.106.043122.

[59] Kang Lin, Sebastian Eckart, Alexander Hartung, Daniel Trabert, Kilian Fehre, Jonas Rist, Lothar Ph H. Schmidt, Markus S. Schöffler, Till Jahnke,

Maksim Kunitski, and Reinhard Dörner. Photoelectron energy peaks shift against the radiation pressure in strong-field ionization. *Sci. Adv.*, 8(12): 1–6, 2022. ISSN 23752548. doi: 10.1126/sciadv.abn7386.

[60] Shichao Sun, Ryan A. Beck, David Williams-Young, and Xiaosong Li. Simulating Magnetic Circular Dichroism Spectra with Real-Time Time-Dependent Density Functional Theory in Gauge including Atomic Orbitals. *J. Chem. Theory Comput.*, 15(12):6824–6831, 2019. ISSN 15499626. doi: 10.1021/acs.jctc.9b00632.

[61] Shichao Sun, Bing Gu, and Shaul Mukamel. Polariton ring currents and circular dichroism of Mg-porphyrin in a chiral cavity. *Chem. Sci.*, 13(4): 1037–1048, 2022. ISSN 20416539. doi: 10.1039/d1sc04341b.

[62] Rosario R. Riso, Laura Grazioli, Enrico Ronca, Tommaso Giovannini, and Henrik Koch. Strong Coupling in Chiral Cavities: Nonperturbative Framework for Enantiomer Discrimination. *Phys. Rev. X*, 13(3): 31002, 2023. ISSN 21603308. doi: 10.1103/PhysRevX.13.031002. URL `https://doi.org/10.1103/PhysRevX.13.031002`.

[63] Christian Schäfer and Denis G. Baranov. Chiral Polaritonics: Analytical Solutions, Intuition, and Use. *J. Phys. Chem. Lett.*, 14(15):3777–3784, 2023. ISSN 19487185. doi: 10.1021/acs.jpclett.3c00286.

[64] Xing Chen, Pengchong Liu, Zhongwei Hu, and Lasse Jensen. High-resolution tip-enhanced Raman scattering probes sub-molecular density changes. *Nat. Commun.*, 10(1):2567, dec 2019. ISSN 2041-1723. doi: 10.1038/s41467-019-10618-x. URL `http://dx.doi.org/10.1038/s41467-019-10618-xhttp://www.nature.com/articles/s41467-019-10618-x`.

[65] Pengchong Liu, Xing Chen, Hepeng Ye, and Lasse Jensen. Resolving Molecular Structures with High-Resolution Tip-Enhanced Raman Scattering Images. *ACS Nano*, page acsnano.9b03980, 2019. ISSN 1936-0851. doi: 10.1021/acsnano.9b03980. URL `http://pubs.acs.org/doi/10.1021/acsnano.9b03980`.

[66] Yair Litman, Franco P. Bonafé, Alaa Akkoush, Heiko Appel, and Mariana Rossi. First-Principles Simulations of Tip Enhanced Raman Scattering Reveal Active Role of Substrate on High-Resolution Images. *J. Phys. Chem. Lett.*, 14(30):6850–6859, 2023. ISSN 19487185. doi: 10.1021/acs.jpclett.3c01216.

[67] Kayn A. Forbes. Raman Optical Activity Using Twisted Photons. *Phys. Rev. Lett.*, 122(10):103201, 2019. ISSN 10797114. doi: 10.1103/PhysRevLett.122.103201. URL https://doi.org/10.1103/PhysRevLett.122.103201.

[68] K. Sueda, G. Miyaji, N. Miyanaga, and M. Nakatsuka. Laguerre-gaussian beam generated with a multilevel spiral phase plate for high intensity laser pulses. *Opt. Express*, 12(15):3548–3553, Jul 2004. doi: 10.1364/OPEX.12.003548. URL https://opg.optica.org/oe/abstract.cfm?URI=oe-12-15-3548.

[69] N. R. Heckenberg, R. McDuff, C. P. Smith, and A. G. White. Generation of optical phase singularities by computer-generated holograms. *Opt. Lett.*, 17(3):221–223, Feb 1992. doi: 10.1364/OL.17.000221. URL https://opg.optica.org/ol/abstract.cfm?URI=ol-17-3-221.

[70] Ebrahim Karimi, Bruno Piccirillo, Eleonora Nagali, Lorenzo Marrucci, and Enrico Santamato. Efficient generation and sorting of orbital angular momentum eigenmodes of light by thermally tuned q-plates. *Applied Physics Letters*, 94(23):231124, June 2009. doi: 10.1063/1.3154549. URL https://doi.org/10.1063/1.3154549.

[71] Eva Prinz, Michael Hartelt, Grisha Spektor, Meir Orenstein, and Martin Aeschlimann. Orbital angular momentum in nanoplasmonic vortices. *ACS Photonics*, 10:340–367, 2023. ISSN 23304022. doi: 10.1021/acsphotonics.2c01321.

[72] R M Kerber, J M Fitzgerald, X Xiao, S S Oh, S A Maier, V Giannini, and D E Reiter. Interaction of an archimedean spiral structure with orbital angular momentum light. *New Journal of Physics*, 20:095005, 9 2018. ISSN 1367-2630. doi: 10.1088/1367-2630/aae105. URL http://stacks.iop.org/1367-2630/20/i=9/a=095005?key=crossref.1b6319e70a57b9dda476d387525a9ec7.

[73] Esra Ilke Albar, Franco P. Bonafé, Valeriia P. Kosheleva, Sebastian T. Ohlmann, Heiko Appel, and Angel Rubio. Time-resolved plasmon-assisted generation of optical-vortex pulses. *Sci. Rep.*, 13(1):1–9, 2023. ISSN 20452322. doi: 10.1038/s41598-023-41606-3. URL https://doi.org/10.1038/s41598-023-41606-3.

[74] Rui Chen, Hong Zhou, Marco Moretti, Xiaodong Wang, and Jiandong Li. Orbital angular momentum waves: Generation, detection, and emerging

applications. *IEEE Communications Surveys & Tutorials*, 22(2):840–868, 2020. doi: 10.1109/COMST.2019.2952453.

[75] Xinyuan Fang, Haoran Ren, Keyao Li, Haitao Luan, Yilin Hua, Qiming Zhang, Xi Chen, and Min Gu. Nanophotonic manipulation of optical angular momentum for high-dimensional information optics. *Advances in Optics and Photonics*, 13(4):772–833, December 2021. ISSN 1943-8206. doi: 10.1364/AOP.414320.

[76] Y. Gorodetski, A. Niv, V. Kleiner, and E. Hasman. Observation of the spin-based plasmonic effect in nanoscale structures. *Physical Review Letters*, 101: 1–4, 2008. ISSN 00319007. doi: 10.1103/PhysRevLett.101.043903.

[77] Tomoki Ohno and Shintaro Miyanishi. Study of surface plasmon chirality induced by archimedes' spiral grooves. *Optics Express*, 14:6285, 2006. ISSN 10944087. doi: 10.1364/oe.14.006285.

[78] Jed I. Ziegler and Richard F. Haglund. Plasmonic response of nanoscale spirals. *Nano Letters*, 10:3013–3018, 2010. ISSN 15306984. doi: 10.1021/nl101475n.

[79] Roderick B. Davidson, Jed I. Ziegler, Guillermo Vargas, Sergey M. Avanesyan, Yu Gong, Wayne Hess, and Richard F. Haglund. Eflcient forward second-harmonic generation from planar archimedean nanospirals. *Nanophotonics*, 4:108–113, 2015. ISSN 21928606. doi: 10.1515/nanoph-2015-0002.

[80] M. Lewenstein, Ph. Balcou, M. Yu. Ivanov, Anne L'Huillier, and P. B. Corkum. Theory of high-harmonic generation by low-frequency laser fields. *Physical Review A*, 49:2117–2132, 3 1994. ISSN 1050-2947. doi: 10.1103/PhysRevA.49.2117. URL `https://link.aps.org/doi/10.1103/PhysRevA.49.2117`.

[81] A. D. Shiner, B. E. Schmidt, C. Trallero-Herrero, H. J. Wörner, S. Patchkovskii, P. B. Corkum, J. C. Kieffer, F. Légaré, and D. M. Villeneuve. Probing collective multi-electron dynamics in xenon with high-harmonic spectroscopy. *Nature Physics 2011 7:6*, 7:464–467, 3 2011. ISSN 1745-2481. doi: 10.1038/nphys1940. URL `https://www.nature.com/articles/nphys1940`.

[82] Nicolas Tancogne-Dejean and Angel Rubio. Atomic-like high-harmonic generation from two-dimensional materials. *Science Advances*, 4(2), Febru-

ary 2018. ISSN 2375-2548. doi: 10.1126/sciadv.aao5207. URL http://dx.doi.org/10.1126/sciadv.aao5207.

[83] H. R. Reiss. Limits on tunneling theories of strong-field ionization. *Physical Review Letters*, 101:043002, 7 2008. ISSN 0031-9007. doi: 10.1103/PhysRevLett.101.043002. URL https://link.aps.org/doi/10.1103/PhysRevLett.101.043002.

[84] Carlos Hernández-García, Antonio Picón, Julio San Román, and Luis Plaja. Attosecond extreme ultraviolet vortices from high-order harmonic generation. *Physical Review Letters*, 111:083602, 8 2013. ISSN 0031-9007. doi: 10.1103/PhysRevLett.111.083602. URL https://link.aps.org/doi/10.1103/PhysRevLett.111.083602.

[85] Fanqi Kong, Chunmei Zhang, Frédéric Bouchard, Zhengyan Li, Graham G. Brown, Dong Hyuk Ko, T. J. Hammond, Ladan Arissian, Robert W. Boyd, Ebrahim Karimi, and P. B. Corkum. Controlling the orbital angular momentum of high harmonic vortices. *Nature Communications*, 8:14970, 4 2017. ISSN 2041-1723. doi: 10.1038/ncomms14970. URL https://www.nature.com/articles/ncomms14970.

[86] Willi Paufler, Birger Böning, and Stephan Fritzsche. High harmonic generation with laguerre–gaussian beams. *Journal of Optics*, 21:094001, 9 2019. ISSN 2040-8978. doi: 10.1088/2040-8986/ab31c3. URL https://iopscience.iop.org/article/10.1088/2040-8986/ab31c3.

[87] A Picón, A Benseny, J Mompart, J R Vázquez de Aldana, L Plaja, G F Calvo, and L Roso. Transferring orbital and spin angular momenta of light to atoms. *New Journal of Physics*, 12:083053, 8 2010. ISSN 1367-2630. doi: 10.1088/1367-2630/12/8/083053. URL https://iopscience.iop.org/article/10.1088/1367-2630/12/8/083053.

[88] Laura Rego, Julio San Román, Antonio Picón, Luis Plaja, and Carlos Hernández-García. Nonperturbative twist in the generation of extreme-ultraviolet vortex beams. *Physical Review Letters*, 117:163202, 10 2016. ISSN 0031-9007. doi: 10.1103/PhysRevLett.117.163202. URL https://link.aps.org/doi/10.1103/PhysRevLett.117.163202.

[89] Nida Haram, Robert T Sang, and Igor V Litvinyuk. Transverse electron momentum distributions in strong-field ionization: nondipole and coulomb focusing effects. *Journal of Physics B: Atomic, Molecular and Optical Physics*, 53:154005, 8 2020. ISSN 0953-4075. doi: 10.1088/1361-6455/ab9272. URL https://iopscience.iop.org/article/10.1088/1361-6455/ab9272.

[90] Nida Haram, Igor Ivanov, Han Xu, Kyung Taec Kim, A. Atia-tul Noor, U. Satya Sainadh, R. D. Glover, D. Chetty, I. V. Litvinyuk, and R. T. Sang. Relativistic nondipole effects in strong-field atomic ionization at moderate intensities. *Phys. Rev. Lett.*, 123:093201, Aug 2019. doi: 10.1103/PhysRevLett.123.093201. URL https://link.aps.org/doi/10.1103/PhysRevLett.123.093201.

[91] J Maurer and U Keller. Ionization in intense laser fields beyond the electric dipole approximation: concepts, methods, achievements and future directions. *Journal of Physics B: Atomic, Molecular and Optical Physics*, 54(9): 094001, May 2021. ISSN 1361-6455. doi: 10.1088/1361-6455/abf731. URL http://dx.doi.org/10.1088/1361-6455/abf731.

[92] M. W. Walser, C. H. Keitel, A. Scrinzi, and T. Brabec. High harmonic generation beyond the electric dipole approximation. *Physical Review Letters*, 85:5082–5085, 12 2000. ISSN 0031-9007. doi: 10.1103/PhysRevLett.85.5082. URL https://link.aps.org/doi/10.1103/PhysRevLett.85.5082.

[93] Lars Bojer Madsen. Disappearance and reappearance of above-threshold-ionization peaks. *Physical Review A*, 106:043118, 10 2022. ISSN 2469-9926. doi: 10.1103/PhysRevA.106.043118. URL https://link.aps.org/doi/10.1103/PhysRevA.106.043118.

[94] M. C. Suster, J. Derlikiewicz, K. Krajewska, F. Cajiao Vélez, and J. Z. Kamiński. Nondipole signatures in ionization and high-order harmonic generation. *Physical Review A*, 107:053112, 5 2023. ISSN 2469-9926. doi: 10.1103/PhysRevA.107.053112. URL https://link.aps.org/doi/10.1103/PhysRevA.107.053112.

[95] Simon Vendelbo Bylling Jensen, Middelhede Lund, and Lars Bojer Madsen. Nondipole strong-field-approximation hamiltonian. *Physical Review A*, 101: 43408, 2020. doi: 10.1103/PhysRevA.101.043408.

[96] Simon Vendelbo Bylling Jensen and Lars Bojer Madsen. Propagation time and nondipole contributions to intraband high-order harmonic generation. *Physical Review A*, 105:L021101, 2 2022. ISSN 2469-9926. doi: 10.1103/PhysRevA.105.L021101. URL https://link.aps.org/doi/10.1103/PhysRevA.105.L021101.

[97] C. T. L. Smeenk, L. Arissian, B. Zhou, A. Mysyrowicz, D. M. Villeneuve, A. Staudte, and P. B. Corkum. Partitioning of the linear photon momentum in multiphoton ionization. *Physical Review Letters*, 106:193002, 5 2011.

ISSN 0031-9007. doi: 10.1103/PhysRevLett.106.193002. URL https://link.aps.org/doi/10.1103/PhysRevLett.106.193002.

[98] Alok Kumar Pandey, Alba De Las Heras, Tanguy Larrieu, Julio San Román, Javier Serrano, Luis Plaja, Elsa Baynard, Moana Pittman, Guillaume Dovillaire, Sophie Kazamias, Carlos Hernández-García, and Olivier Guilbaud. Characterization of extreme ultraviolet vortex beams with a very high topological charge. *ACS Photonics*, 9:944–951, 3 2022. ISSN 23304022. doi: 10.1021/acsphotonics.1c01768.

[99] Franco P. Bonafé, Esra Ilke Albar, Sebastian T. Ohlmann, Valeriia P. Kosheleva, Carlos M. Bustamante, Francesco Troisi, Angel Rubio, and Heiko Appel. Full minimal coupling maxwell-tddft: An ab initio framework for light-matter interaction beyond the dipole approximation. *Phys. Rev. B*, 111:085114, Feb 2025. doi: 10.1103/PhysRevB.111.085114. URL https://link.aps.org/doi/10.1103/PhysRevB.111.085114.

[100] Nicolas Tancogne-Dejean, Micael J. T. Oliveira, Xavier Andrade, Heiko Appel, Carlos H. Borca, Guillaume Le Breton, Florian Buchholz, Alberto Castro, Stefano Corni, Alfredo A. Correa, Umberto De Giovannini, Alain Delgado, Florian G. Eich, Johannes Flick, Gabriel Gil, Adrián Gomez, Nicole Helbig, Hannes Hübener, René Jestädt, Joaquim Jornet-Somoza, Ask H. Larsen, Irina V. Lebedeva, Martin Lüders, Miguel A. L. Marques, Sebastian T. Ohlmann, Silvio Pipolo, Markus Rampp, Carlo A. Rozzi, David A. Strubbe, Shunsuke A. Sato, Christian Schäfer, Iris Theophilou, Alicia Welden, and Angel Rubio. Octopus, a computational framework for exploring light-driven phenomena and quantum dynamics in extended and finite systems. *J. Chem. Phys.*, 152(12):124119, mar 2020. ISSN 0021-9606. doi: 10.1063/1.5142502. URL https://doi.org/10.1063/1.5142502http://aip.scitation.org/doi/10.1063/1.5142502https://aip.scitation.org/doi/10.1063/1.5142502.

[101] P. Hohenberg and W. Kohn. Inhomogeneous electron gas. *Physical Review*, 136(3B):B864–B871, November 1964. ISSN 0031-899X. doi: 10.1103/physrev.136.b864. URL http://dx.doi.org/10.1103/PhysRev.136.B864.

[102] W. Kohn and L. J. Sham. Self-consistent equations including exchange and correlation effects. *Physical Review*, 140(4A):A1133–A1138, November 1965. ISSN 0031-899X. doi: 10.1103/physrev.140.a1133. URL http://dx.doi.org/10.1103/PhysRev.140.A1133.

[103] John P. Perdew, Kieron Burke, and Matthias Ernzerhof. Generalized gradient approximation made simple. *Physical Review Letters*, 77(18):3865–3868, October 1996. ISSN 1079-7114. doi: 10.1103/physrevlett.77.3865. URL http://dx.doi.org/10.1103/PhysRevLett.77.3865.

[104] J. P. Perdew and Alex Zunger. Self-interaction correction to density-functional approximations for many-electron systems. *Physical Review B*, 23(10):5048–5079, May 1981. ISSN 0163-1829. doi: 10.1103/physrevb.23.5048. URL http://dx.doi.org/10.1103/PhysRevB.23.5048.

[105] A. D. Becke. Density-functional exchange-energy approximation with correct asymptotic behavior. *Physical Review A*, 38(6):3098–3100, September 1988. ISSN 0556-2791. doi: 10.1103/physreva.38.3098. URL http://dx.doi.org/10.1103/PhysRevA.38.3098.

[106] John P. Perdew. Jacob's ladder of density functional approximations for the exchange-correlation energy. In *AIP Conference Proceedings*, volume 577, page 1–20. AIP, 2001. doi: 10.1063/1.1390175. URL http://dx.doi.org/10.1063/1.1390175.

[107] Roberto D'Agosta and Giovanni Vignale. Non-v-representability of currents in time-dependent many-particle systems. *Physical Review B*, 71(24), June 2005. ISSN 1550-235X. doi: 10.1103/physrevb.71.245103. URL http://dx.doi.org/10.1103/PhysRevB.71.245103.

[108] Erich Runge and E. K. U. Gross. Density-functional theory for time-dependent systems. *Physical Review Letters*, 52(12):997–1000, March 1984. ISSN 0031-9007. doi: 10.1103/physrevlett.52.997. URL http://dx.doi.org/10.1103/PhysRevLett.52.997.

[109] Robert van Leeuwen. Mapping from densities to potentials in time-dependent density-functional theory. *Physical Review Letters*, 82(19):3863–3866, May 1999. ISSN 1079-7114. doi: 10.1103/physrevlett.82.3863. URL http://dx.doi.org/10.1103/PhysRevLett.82.3863.

[110] M. Gross and S. Haroche. Superradiance: An essay on the theory of collective spontaneous emission. *Physics Reports*, 93(5):301–396, 1982. ISSN 0370-1573. doi: https://doi.org/10.1016/0370-1573(82)90102-8. URL https://www.sciencedirect.com/science/article/pii/0370157382901028.

[111] Carsten A. Ullrich. *Time-dependent density-functional theory: concepts and applications*. Oxford University Press, 2011.

[112] Neepa T. Maitra, Kieron Burke, and Chris Woodward. Memory in time-dependent density functional theory. *Physical Review Letters*, 89(2), June 2002. ISSN 1079-7114. doi: 10.1103/physrevlett.89.023002. URL http://dx.doi.org/10.1103/PhysRevLett.89.023002.

[113] Neepa T. Maitra. Perspective: Fundamental aspects of time-dependent density functional theory. *The Journal of Chemical Physics*, 144(22), June 2016. ISSN 1089-7690. doi: 10.1063/1.4953039. URL http://dx.doi.org/10.1063/1.4953039.

[114] Volker Blum, Ralf Gehrke, Felix Hanke, Paula Havu, Ville Havu, Xinguo Ren, Karsten Reuter, and Matthias Scheffler. Ab initio molecular simulations with numeric atom-centered orbitals. *Computer Physics Communications*, 180(11):2175–2196, November 2009. ISSN 0010-4655. doi: 10.1016/j.cpc.2009.06.022. URL http://dx.doi.org/10.1016/j.cpc.2009.06.022.

[115] Alberto Castro, Heiko Appel, Micael Oliveira, Carlo A. Rozzi, Xavier Andrade, Florian Lorenzen, M. A. L. Marques, E. K. U. Gross, and Angel Rubio. octopus:a tool for the application of time-dependent density functional theory. *physica status solidi (b)*, 243(11):2465–2488, June 2006. ISSN 1521-3951. doi: 10.1002/pssb.200642067. URL http://dx.doi.org/10.1002/pssb.200642067.

[116] Nicolas Tancogne-Dejean, Micael J. T. Oliveira, Xavier Andrade, Heiko Appel, Carlos H. Borca, Guillaume Le Breton, Florian Buchholz, Alberto Castro, Stefano Corni, Alfredo A. Correa, Umberto De Giovannini, Alain Delgado, Florian G. Eich, Johannes Flick, Gabriel Gil, Adrián Gomez, Nicole Helbig, Hannes Hübener, René Jestädt, Joaquim Jornet-Somoza, Ask H. Larsen, Irina V. Lebedeva, Martin Lüders, Miguel A. L. Marques, Sebastian T. Ohlmann, Silvio Pipolo, Markus Rampp, Carlo A. Rozzi, David A. Strubbe, Shunsuke A. Sato, Christian Schäfer, Iris Theophilou, Alicia Welden, and Angel Rubio. Octopus, a computational framework for exploring light-driven phenomena and quantum dynamics in extended and finite systems. *The Journal of Chemical Physics*, 152(12):124119, March 2020. doi: 10.1063/1.5142502. URL https://doi.org/10.1063/1.5142502.

[117] Heiko Appel. *Time-Dependent Quantum Many-Body Systems: Linear Response, Electronic Transport, and Reduced Density Matrices*. PhD thesis, Freie Universität Berlin, 2007. URL https://refubium.fu-berlin.de/handle/fub188/11190.

[118] Umberto De Giovannini, Ask Hjorth Larsen, and Angel Rubio. Modeling electron dynamics coupled to continuum states in finite volumes with absorbing boundaries. *The European Physical Journal B*, 88(3), March 2015. ISSN 1434-6036. doi: 10.1140/epjb/e2015-50808-0. URL http://dx.doi.org/10.1140/epjb/e2015-50808-0.

[119] Sohrab Ismail-Beigi, Eric K. Chang, and Steven G. Louie. Coupling of nonlocal potentials to electromagnetic fields. *Phys. Rev. Lett.*, 87(8):87402–1–87402–4, 2001. ISSN 10797114. doi: 10.1103/PhysRevLett.87.087402.

[120] Chris J. Pickard and Francesco Mauri. Nonlocal Pseudopotentials and Magnetic Fields. *Phys. Rev. Lett.*, 91(19):196401, nov 2003. ISSN 0031-9007. doi: 10.1103/PhysRevLett.91.196401. URL https://link.aps.org/doi/10.1103/PhysRevLett.91.196401.

[121] Ludwig Silberstein. Elektromagnetische grundgleichungen in bivektorieller behandlung. *Annalen der Physik*, 327(3):579–586, January 1907. ISSN 1521-3889. doi: 10.1002/andp.19073270313. URL http://dx.doi.org/10.1002/andp.19073270313.

[122] I. Białynicki-Birula. On the wave function of the photon. *Acta Physica Polonica A*, 86(1–2):97–116, July 1994. ISSN 1898-794X. doi: 10.12693/aphyspola.86.97. URL http://dx.doi.org/10.12693/APhysPolA.86.97.

[123] Iwo Bialynicki-Birula. *V Photon Wave Function*, page 245–294. Elsevier, 1996. ISBN 9780444825308. doi: 10.1016/s0079-6638(08)70316-0. URL http://dx.doi.org/10.1016/S0079-6638(08)70316-0.

[124] René Jestädt. Fully coupled maxwell-kohn-sham systems. 2020. doi: 10.14279/DEPOSITONCE-9825. URL https://depositonce.tu-berlin.de/handle/11303/10932.

[125] René Jestädt, Michael Ruggenthaler, Micael J. T. Oliveira, Angel Rubio, and Heiko Appel. Light-matter interactions within the ehrenfest–maxwell–pauli–kohn–sham framework: fundamentals, implementation, and nano-optical applications. *Advances in Physics*, 68(4):225–333, October 2019. doi: 10.1080/00018732.2019.1695875. URL https://doi.org/10.1080/00018732.2019.1695875.

[126] Kane Yee. Numerical solution of initial boundary value problems involving maxwell's equations in isotropic media. *IEEE Transactions on Antennas and Propagation*, 14(3):302–307, 1966. doi: 10.1109/TAP.1966.1138693.

[127] Allen Taflove and Susan C. Hagness. *Computational electrodynamics: the finite-difference time-domain method*. Artech House, Norwood, 3rd edition, 2005.

[128] I. I. Rabi. Space quantization in a gyrating magnetic field. *Physical Review*, 51(8):652–654, April 1937. ISSN 0031-899X. doi: 10.1103/physrev.51.652. URL http://dx.doi.org/10.1103/PhysRev.51.652.

[129] E.T. Jaynes and F.W. Cummings. Comparison of quantum and semiclassical radiation theories with application to the beam maser. *Proceedings of the IEEE*, 51(1):89–109, 1963. ISSN 0018-9219. doi: 10.1109/proc.1963.1664. URL http://dx.doi.org/10.1109/PROC.1963.1664.

[130] Michael Tavis and Frederick W. Cummings. Exact solution for an n-molecule—radiation-field hamiltonian. *Physical Review*, 170(2):379–384, June 1968. ISSN 0031-899X. doi: 10.1103/physrev.170.379. URL http://dx.doi.org/10.1103/PhysRev.170.379.

[131] R. H. Dicke. Coherence in spontaneous radiation processes. *Physical Review*, 93(1):99–110, January 1954. ISSN 0031-899X. doi: 10.1103/physrev.93.99. URL http://dx.doi.org/10.1103/PhysRev.93.99.

[132] Kayn A. Forbes and David L. Andrews. Optical orbital angular momentum: twisted light and chirality. *Optics Letters*, 43(3):435, January 2018. ISSN 1539-4794. doi: 10.1364/ol.43.000435. URL http://dx.doi.org/10.1364/OL.43.000435.

[133] VB Berestetskii, EM Lifshitz, and P Pitaevskii. *Relativistic Quantum Theory, Part 1*. Pergamon, 1971. ISBN 978-0080160252.

[134] A. M. Stewart. Vector potential of the Coulomb gauge. *Eur. J. Phys.*, 24 (5):519–524, 2003. ISSN 01430807. doi: 10.1088/0143-0807/24/5/308.

[135] Walter Greiner. *Classical Electrodynamics*. Springer New York, 1998. doi: 10.1007/978-1-4612-0587-6. URL https://doi.org/10.1007/978-1-4612-0587-6.

[136] R. P. Schmidt, S. Ramakrishna, A. A. Peshkov, N. Huntemann, E. Peik, S. Fritzsche, and A. Surzhykov. Atomic photoexcitation as a tool for probing purity of twisted light modes. *Phys. Rev. A*, 109:033103, Mar 2024. doi: 10.1103/PhysRevA.109.033103. URL https://link.aps.org/doi/10.1103/PhysRevA.109.033103.

[137] S. A.-L. Schulz, A. A. Peshkov, R. A. Müller, R. Lange, N. Huntemann, Chr. Tamm, E. Peik, and A. Surzhykov. Generalized excitation of atomic multipole transitions by twisted light modes. *Phys. Rev. A*, 102:012812, Jul 2020. doi: 10.1103/PhysRevA.102.012812. URL https://link.aps.org/doi/10.1103/PhysRevA.102.012812.

[138] Mark I. Stockman. Nanoplasmonics: past, present, and glimpse into future. *Opt. Express*, 19(22):22029–22106, Oct 2011. doi: 10.1364/OE.19.022029. URL https://opg.optica.org/oe/abstract.cfm?URI=oe-19-22-22029.

[139] William L. Barnes, Alain Dereux, and Thomas W. Ebbesen. Surface plasmon subwavelength optics. *Nature*, 424(6950):824–830, August 2003. ISSN 1476-4687. doi: 10.1038/nature01937. URL http://dx.doi.org/10.1038/nature01937.

[140] Maria Solyanik-Gorgone, Andrei Afanasev, Carl E. Carlson, Christian T. Schmiegelow, and Ferdinand Schmidt-Kaler. Excitation of e1-forbidden atomic transitions with electric, magnetic or mixed multipolarity in light fields carrying orbital and spin angular momentum. 36, 2018. URL http://arxiv.org/abs/1811.05871.

[141] Richard M. Kerber, Jamie M. Fitzgerald, Doris E. Reiter, Sang Soon Oh, and Ortwin Hess. Reading the orbital angular momentum of light using plasmonic nanoantennas. *ACS Photonics*, 4:891–896, 2017. ISSN 23304022. doi: 10.1021/acsphotonics.6b00980.

[142] Hwi Kim, Junghyun Park, Seong Woo Cho, Seung Yeol Lee, Minsu Kang, and Byoungho Lee. Synthesis and dynamic switching of surface plasmon vortices with plasmonic vortex lens, 2010. ISSN 15306984.

[143] G. Spektor, D. Kilbane, A. K. Mahro, B. Frank, S. Ristok, L. Gal, P. Kahl, D. Podbiel, S. Mathias, H. Giessen, F.-J. Meyer zu Heringdorf, M. Orenstein, and M. Aeschlimann. Revealing the subfemtosecond dynamics of orbital angular momentum in nanoplasmonic vortices. *Science*, 355:1187–1191, 3 2017. ISSN 0036-8075. doi: 10.1126/science.aaj1699. URL http://www.sciencemag.org/lookup/doi/10.1126/science.aaj1699.

[144] Denis Garoli, Pierfrancesco Zilio, Yuri Gorodetski, Francesco Tantussi, and Francesco De Angelis. Optical vortex beam generator at nanoscale level. *Scientific Reports*, 6(1), July 2016. doi: 10.1038/srep29547. URL https://doi.org/10.1038/srep29547.

[145] Openscad – the programmers solid 3d cad modeller. https://openscad.org.

[146] The CGAL Project. *CGAL User and Reference Manual*. CGAL Editorial Board, 5.5.2 edition, 2023. URL https://doc.cgal.org/5.5.2/Manual/packages.html.

[147] Aleksandar D. Rakić, Aleksandra B. Djurišić, Jovan M. Elazar, and Marian L. Majewski. Optical properties of metallic films for vertical-cavity optoelectronic devices. *Applied Optics*, 37(22):5271, August 1998. doi: 10.1364/ao.37.005271. URL https://doi.org/10.1364/ao.37.005271.

[148] Jean-Pierre Berenger. A perfectly matched layer for the absorption of electromagnetic waves. *Journal of Computational Physics*, 114(2):185–200, October 1994. ISSN 0021-9991. doi: 10.1006/jcph.1994.1159. URL http://dx.doi.org/10.1006/jcph.1994.1159.

[149] Adrián Gómez Pueyo, Sergio Blanes, and Alberto Castro. Propagators for quantum-classical models: Commutator-free magnus methods. *Journal of Chemical Theory and Computation*, 16(3):1420–1430, 2020. doi: 10.1021/acs.jctc.9b01031.

[150] V E Lembessis, S Al-Awfi, M Babiker, and D L Andrews. Surface plasmon optical vortices and their influence on atoms. *Journal of Optics*, 13(6):064002, apr 2011. doi: 10.1088/2040-8978/13/6/064002. URL https://dx.doi.org/10.1088/2040-8978/13/6/064002.

[151] Esra Ilke Albar, Franco Paul Bonafé, Valeriia Kosheleva, Heiko Appel, Sebastian Ohlmann, and Angel Rubio. Time-resolved plasmon-assisted generation of arbitrary optical-vortex pulses - supporting information - trajectories, 2023. URL https://zenodo.org/record/8208595.

[152] Hannes Hübener, Umberto De Giovannini, Christian Schäfer, Johan Andberger, Michael Ruggenthaler, Jerome Faist, and Angel Rubio. Engineering quantum materials with chiral optical cavities. *Nature Materials*, 20(4):438–442, November 2020. doi: 10.1038/s41563-020-00801-7. URL https://doi.org/10.1038/s41563-020-00801-7.

[153] Carlos Hernández-García, Jorge Vieira, Jose T. Mendonça, Laura Rego, Julio San Román, Luis Plaja, Primoz R. Ribic, David Gauthier, and Antonio Picón. Generation and applications of extreme-ultraviolet vortices. *Photonics*, 4(2), 2017. ISSN 2304-6732. doi: 10.3390/photonics4020028. URL https://www.mdpi.com/2304-6732/4/2/28.

[154] Y. Toda, S. Honda, and R. Morita. Dynamics of a paired optical vortex generated by second-harmonic generation. *Opt. Express*, 18(17):17796–17804, Aug 2010. doi: 10.1364/OE.18.017796. URL https://opg.optica.org/oe/abstract.cfm?URI=oe-18-17-17796.

[155] M. Zürch, C. Kern, P. Hansinger, A. Dreischuh, and Ch Spielmann. Strong-field physics with singular light beams. *Nature Physics*, 8:743–746, 2012. ISSN 17452481. doi: 10.1038/nphys2397.

[156] Genevieve Gariepy, Jonathan Leach, Kyung Taec Kim, T. J. Hammond, E. Frumker, Robert W. Boyd, and P. B. Corkum. Creating high-harmonic beams with controlled orbital angular momentum. *Phys. Rev. Lett.*, 113: 153901, Oct 2014. doi: 10.1103/PhysRevLett.113.153901. URL https://link.aps.org/doi/10.1103/PhysRevLett.113.153901.

[157] D. Gauthier, P. Rebernik Ribic, G. Adhikary, A. Camper, C. Chappuis, R. Cucini, L. F. Dimauro, G. Dovillaire, F. Frassetto, R. Géneaux, P. Miotti, L. Poletto, B. Ressel, C. Spezzani, M. Stupar, T. Ruchon, and G. De Ninno. Tunable orbital angular momentum in high-harmonic generation. *Nature Communications*, 8, 4 2017. ISSN 20411723. doi: 10.1038/ncomms14971.

[158] Alok Kumar Pandey, Alba de las Heras, Tanguy Larrieu, Julio San Román, Javier Serrano, Luis Plaja, Elsa Baynard, Moana Pittman, Guillaume Dovillaire, Sophie Kazamias, Carlos Hernández-García, and Olivier Guilbaud. Characterization of extreme ultraviolet vortex beams with a very high topological charge. *ACS Photonics*, 9(3):944–951, 2022. doi: 10.1021/acsphotonics.1c01768. URL https://doi.org/10.1021/acsphotonics.1c01768.

[159] R. Géneaux, A. Camper, T. Auguste, O. Gobert, J. Caillat, R. Taïeb, and T. Ruchon. Synthesis and characterization of attosecond light vortices in the extreme ultraviolet. *Nature Communications*, 7, 8 2016. ISSN 20411723. doi: 10.1038/ncomms12583.

[160] F. Sanson, A. K. Pandey, F. Harms, G. Dovillaire, E. Baynard, J. Demailly, O. Guilbaud, B. Lucas, O. Neveu, M. Pittman, D. Ros, M. Richardson, E. Johnson, W. Li, Ph. Balcou, and S. Kazamias. Hartmann wavefront sensor characterization of a high charge vortex beam in the extreme ultraviolet spectral range. *Opt. Lett.*, 43(12):2780–2783, Jun 2018. doi: 10.1364/OL.43.002780. URL https://opg.optica.org/ol/abstract.cfm?URI=ol-43-12-2780.

[161] Laura Rego, Nathan J. Brooks, Quynh L. D. Nguyen, Julio San Román, Iona Binnie, Luis Plaja, Henry C. Kapteyn, Margaret M. Murnane, and Carlos Hernández-García. Necklace-structured high-harmonic generation for low-divergence, soft x-ray harmonic combs with tunable line spacing. *Science Advances*, 8(5):eabj7380, 2022. doi: 10.1126/sciadv.abj7380. URL https://www.science.org/doi/abs/10.1126/sciadv.abj7380.

[162] Laura Rego, Kevin M. Dorney, Nathan J. Brooks, Quynh L. Nguyen, Chen-Ting Liao, Julio San Román, David E. Couch, Allison Liu, Emilio Pisanty, Maciej Lewenstein, Luis Plaja, Henry C. Kapteyn, Margaret M. Murnane, and Carlos Hernández-García. Generation of extreme-ultraviolet beams with time-varying orbital angular momentum. *Science*, 364(6447): eaaw9486, 2019. doi: 10.1126/science.aaw9486. URL https://www.science.org/doi/abs/10.1126/science.aaw9486.

[163] A. Ludwig, J. Maurer, B.W. Mayer, C.R. Phillips, L. Gallmann, and U. Keller. Breakdown of the dipole approximation in strong-field ionization. *Physical Review Letters*, 113(24), December 2014. ISSN 1079-7114. doi: 10.1103/physrevlett.113.243001. URL http://dx.doi.org/10.1103/PhysRevLett.113.243001.

[164] Alberto Castro, Angel Rubio, and Eberhard K. U. Gross. Enhancing and controlling single-atom high-harmonic generation spectra: a time-dependent density-functional scheme. *The European Physical Journal B*, 88(8), August 2015. ISSN 1434-6036. doi: 10.1140/epjb/e2015-50889-7. URL http://dx.doi.org/10.1140/epjb/e2015-50889-7.

[165] Ofer Neufeld, Zahra Nourbakhsh, Nicolas Tancogne-Dejean, and Angel Rubio. Ab initio cluster approach for high harmonic generation in liquids. *Journal of Chemical Theory and Computation*, 18(7):4117–4126, June 2022. ISSN 1549-9626. doi: 10.1021/acs.jctc.2c00235. URL http://dx.doi.org/10.1021/acs.jctc.2c00235.

[166] Nicolas Tancogne-Dejean and Angel Rubio. Atomic-like high-harmonic generation from two-dimensional materials. *Science Advances*, 4(2), February 2018. ISSN 2375-2548. doi: 10.1126/sciadv.aao5207. URL http://dx.doi.org/10.1126/sciadv.aao5207.

[167] Adrián Gómez Pueyo, Miguel A. L. Marques, Angel Rubio, and Alberto Castro. Propagators for the time-dependent kohn–sham equations: Multistep, runge–kutta, exponential runge–kutta, and commutator free magnus methods. *Journal of Chemical Theory and Computation*, 14(6):3040–3052,

April 2018. ISSN 1549-9626. doi: 10.1021/acs.jctc.8b00197. URL http://dx.doi.org/10.1021/acs.jctc.8b00197.

[168] Jonas Wätzel and Jamal Berakdar. Multipolar, polarization-shaped high-order harmonic generation by intense vector beams. *Phys. Rev. A*, 101: 043409, Apr 2020. doi: 10.1103/PhysRevA.101.043409. URL https://link.aps.org/doi/10.1103/PhysRevA.101.043409.

[169] G. F. Quinteiro, C. T. Schmiegelow, D. E. Reiter, and T. Kuhn. Re-examination of bessel beams: A generalized scheme to derive optical vortices. *Physical Review A*, 99(2), February 2019. ISSN 2469-9934. doi: 10.1103/physreva.99.023845. URL http://dx.doi.org/10.1103/PhysRevA.99.023845.

[170] J. D. Jackson. Electrodynamics, classical, April 2003. URL http://dx.doi.org/10.1002/3527600434.eap109.

[171] Alexey Gorlach, Ofer Neufeld, Nicholas Rivera, Oren Cohen, and Ido Kaminer. The quantum-optical nature of high harmonic generation. *Nature Communications*, 11(1), September 2020. ISSN 2041-1723. doi: 10.1038/s41467-020-18218-w. URL http://dx.doi.org/10.1038/s41467-020-18218-w.

[172] Esra Ilke Albar. Animated trajectories for hhg with oam light beyond dipole, 2025. https://zenodo.org/record/14930614
DOI: 10.5281/zenodo.14930614.

[173] E. S. Sarachik and G. T. Schappert. Classical theory of the scattering of intense laser radiation by free electrons. *Physical Review D*, 1:2738–2753, 5 1970. ISSN 0556-2821. doi: 10.1103/PhysRevD.1.2738. URL https://link.aps.org/doi/10.1103/PhysRevD.1.2738.

[174] H R Reiss. The tunnelling model of laser-induced ionization and its failure at low frequencies. *Journal of Physics B: Atomic, Molecular and Optical Physics*, 47:204006, 10 2014. ISSN 0953-4075. doi: 10.1088/0953-4075/47/20/204006. URL https://iopscience.iop.org/article/10.1088/0953-4075/47/20/204006.

[175] Jonas Wätzel and Jamal Berakdar. Topological light fields for highly nonlinear charge quantum dynamics and high harmonic generation. *Optics Express*, 28(13):19469, June 2020. ISSN 1094-4087. doi: 10.1364/oe.395590. URL http://dx.doi.org/10.1364/OE.395590.

[176] Alba de las Heras, Alok Kumar Pandey, Julio San Román, Javier Serrano, Elsa Baynard, Guillaume Dovillaire, Moana Pittman, Charles G. Durfee, Luis Plaja, Sophie Kazamias, Olivier Guilbaud, and Carlos Hernández-García. Extreme-ultraviolet vector-vortex beams from high harmonic generation. *Optica*, 9:71, 1 2022. ISSN 2334-2536. doi: 10.1364/OPTICA.442304. URL https://opg.optica.org/abstract.cfm?URI=optica-9-1-71.

[177] Nobuhisa Ishii, Keisuke Kaneshima, Kenta Kitano, Teruto Kanai, Shuntaro Watanabe, and Jiro Itatani. Carrier-envelope phase-dependent high harmonic generation in the water window using few-cycle infrared pulses. *Nature Communications*, 5(1), February 2014. ISSN 2041-1723. doi: 10.1038/ncomms4331. URL http://dx.doi.org/10.1038/ncomms4331.

[178] N. Troullier and José Luriaas Martins. Efficient pseudopotentials for plane-wave calculations. *Physical Review B*, 43(3):1993–2006, January 1991. ISSN 1095-3795. doi: 10.1103/physrevb.43.1993. URL http://dx.doi.org/10.1103/PhysRevB.43.1993.

[179] Ofir E. Alon, Vitali Averbukh, and Nimrod Moiseyev. Selection rules for the high harmonic generation spectra. *Physical Review Letters*, 80(17): 3743–3746, April 1998. ISSN 1079-7114. doi: 10.1103/physrevlett.80.3743. URL http://dx.doi.org/10.1103/PhysRevLett.80.3743.

[180] Roi Baer, Daniel Neuhauser, Petra R. Ždánská, and Nimrod Moiseyev. Ionization and high-order harmonic generation in aligned benzene by a short intense circularly polarized laser pulse. *Physical Review A*, 68(4), October 2003. ISSN 1094-1622. doi: 10.1103/physreva.68.043406. URL http://dx.doi.org/10.1103/PhysRevA.68.043406.

[181] Claude Cohen-Tannoudji, Bernard Diu, and Franck Laloe. *Quantum mechanics: Vol. 1.* Wiley, New York, 1977. ISBN 047116433X.

[182] Genko S Vasilev, Daniel Ljunggren, and Axel Kuhn. Single photons made-to-measure. *New Journal of Physics*, 12(6):063024, June 2010. ISSN 1367-2630. doi: 10.1088/1367-2630/12/6/063024. URL http://dx.doi.org/10.1088/1367-2630/12/6/063024.

[183] Kilian Hader, Julian Albert, E. K. U. Gross, and Volker Engel. Electron-nuclear wave-packet dynamics through a conical intersection. *The Journal of Chemical Physics*, 146(7), February 2017. ISSN 1089-7690. doi: 10.1063/1.4975811. URL http://dx.doi.org/10.1063/1.4975811.

[184] Markus C. Kohler, Christian Ott, Philipp Raith, Robert Heck, Iris Schlegel, Christoph H. Keitel, and Thomas Pfeifer. High harmonic generation via continuum wave-packet interference. *Physical Review Letters*, 105(20), November 2010. ISSN 1079-7114. doi: 10.1103/physrevlett.105.203902. URL http://dx.doi.org/10.1103/PhysRevLett.105.203902.

[185] P. A. Čerenkov. Visible radiation produced by electrons moving in a medium with velocities exceeding that of light. *Physical Review*, 52(4): 378–379, August 1937. ISSN 0031-899X. doi: 10.1103/physrev.52.378. URL http://dx.doi.org/10.1103/PhysRev.52.378.

[186] I. Frank and Ig. Tamm. *Coherent Visible Radiation of Fast Electrons Passing Through Matter*, pages 29–35. Springer, Berlin, Heidelberg, 1991. ISBN 978-3-642-74626-0. doi: 10.1007/978-3-642-74626-0_2. URL https://doi.org/10.1007/978-3-642-74626-0_2.

[187] Vitalii L Ginzburg. Radiation by uniformly moving sources (vavilov–cherenkov effect, transition radiation, and other phenomena). *Physics-Uspekhi*, 39(10):973–982, October 1996. ISSN 1468-4780. doi: 10.1070/pu1996v039n10abeh000171. URL http://dx.doi.org/10.1070/PU1996v039n10ABEH000171.

[188] Esther Ciarrocchi and Nicola Belcari. Cerenkov luminescence imaging: physics principles and potential applications in biomedical sciences. *EJNMMI Physics*, 4(1), March 2017. ISSN 2197-7364. doi: 10.1186/s40658-017-0181-8. URL http://dx.doi.org/10.1186/s40658-017-0181-8.

[189] Boris M Bolotovskii. Vavilov – cherenkov radiation: its discovery and application. *Physics-Uspekhi*, 52(11):1099–1110, November 2009. ISSN 1468-4780. doi: 10.3367/ufne.0179.200911c.1161. URL http://dx.doi.org/10.3367/ufne.0179.200911c.1161.

[190] Octopus Developers. Maxwell input file tutorial. URL https://www.octopus-code.org/documentation/16/tutorial/maxwell/. Accessed: 2025-12-08.

[191] Charles Roques-Carmes, Nicholas Rivera, John D. Joannopoulos, Marin Soljačić, and Ido Kaminer. Nonperturbative Quantum Electrodynamics in the Cherenkov Effect. *Phys. Rev. X*, 8(4):1–16, 2018. ISSN 21603308. doi: 10.1103/PhysRevX.8.041013.

[192] Konstantin Y. Bliokh. Spatiotemporal vortex pulses: Angular momenta and spin-orbit interaction. *Physical Review Letters*, 126(24), June 2021. ISSN 1079-7114. doi: 10.1103/physrevlett.126.243601. URL http://dx.doi.org/10.1103/PhysRevLett.126.243601.

[193] Andy Chong, Chenhao Wan, Jian Chen, and Qiwen Zhan. Generation of spatiotemporal optical vortices with controllable transverse orbital angular momentum. *Nature Photonics*, 14(6):350–354, February 2020. ISSN 1749-4893. doi: 10.1038/s41566-020-0587-z. URL http://dx.doi.org/10.1038/s41566-020-0587-z.

[194] L. M. Rodrigues, L. Marques Fagundes, D. C. Salles, G. H. dos Santos, J. M. Kondo, P. H. Souto Ribeiro, A. Z. Khoury, and R. Medeiros de Araújo. Resonance of vector vortex beams in a triangular optical cavity. *Scientific Reports*, 14(1), May 2024. ISSN 2045-2322. doi: 10.1038/s41598-024-59630-2. URL http://dx.doi.org/10.1038/s41598-024-59630-2.

[195] Giovanni De Ninno, Jonas Wätzel, Primož Rebernik Ribič, Enrico Allaria, Marcello Coreno, Miltcho B. Danailov, Christian David, Alexander Demidovich, Michele Di Fraia, Luca Giannessi, Klavs Hansen, Špela Krušič, Michele Manfredda, Michael Meyer, Andrej Mihelič, Najmeh Mirian, Oksana Plekan, Barbara Ressel, Benedikt Rösner, Alberto Simoncig, Simone Spampinati, Matija Stupar, Matjaž Žitnik, Marco Zangrando, Carlo Callegari, and Jamal Berakdar. Photoelectric effect with a twist. *Nature Photonics*, 14(9):554–558, August 2020. ISSN 1749-4893. doi: 10.1038/s41566-020-0669-y. URL http://dx.doi.org/10.1038/s41566-020-0669-y.

[196] Mohamed Babiker, David L Andrews, and Vassilis E Lembessis. Atoms in complex twisted light. *Journal of Optics*, 21(1):013001, December 2018. ISSN 2040-8986. doi: 10.1088/2040-8986/aaed14. URL http://dx.doi.org/10.1088/2040-8986/aaed14.